Characterizing & Modelling the Bio-Nano Interface

Alexis V. Belessiotis-Richards

Imperial College London
Departments of Materials

Submitted in accordance with the requirements for the degree
of Doctor of Philosophy

April 2021

Declaration of Originality

I, Alexis Belessiotis-Richards, declare that the scientific content contained within this thesis was prepared, acquired, and analysed by myself at Imperial College London and Massachusetts Institute of Technology. Contributors of all collaborative efforts are noted in the text and appropriately referenced.

Copyright Declaration

The copyright of this thesis rests with the author and is made available under a Creative Commons Attribution Non-Commercial No Derivatives license. Researchers are free to copy, distribute or transmit the thesis on the condition that they attribute it, that they do not use it for commercial purposes and that they do not alter, transform or build upon it. For any reuse or redistribution, researchers must make clear to others the license terms of this work.

Acknowledgements

I am very grateful to my supervisor Professor Molly M. Stevens who has continuously supported my research and personal development over the past five years. Thank you Molly for giving me the opportunity to join the group as an undergraduate in 2015 and for allowing me to develop my research interests throughout the PhD. Your mentorship has truly allowed me to grow into an independent and driven researcher.

I am grateful to the professors who have generously shared their time and insights with me throughout my degree. In particular, I would like to thank Professor Alfredo Alexander-Katz for hosting me in his lab and who has been a regular presence throughout the PhD. I would also like to thank Professor Irene Yarovsky for hosting me in her lab and for supporting my work on anti-fouling membranes. I would like to thank Professor Mark S. P. Sansom for his insights and support on my work on protein-membrane interactions. I would also like to thank Professor David J. Payne, Dr Stefano Angioletti-Uberti and Professor Giuseppe Battaglia for their support throughout the degree.

The postdoctoral researchers who I have crossed paths with over the course of the PhD have been extremely patient and supportive of my development. In particular, I would like to thank Dr Stuart G. Higgins for his continued and regular support, including meetings, in-depth proof-reading of my writing and his effort to drive me towards the best possible outcome. Dr Adrian Najer has regularly supported me and taught me of protein interactions with synthetic membranes. Dr Mukarram Tahir taught me soft matter simulations using GROMACS and his input was crucial in the first year of my PhD. Dr Matt Penna mentored me during my time in Melbourne and taught me atomistic MD simulations and protein-fouling methods. I would also like to thank now Professors Nadav Amdursky and Michael Albro for taking me on as an undergraduate researcher and introducing me to the Stevens group way back in 2015.

I would like to thank the EPSRC Centre for Doctoral Training in Advanced Characterisation of Materials (ACM-CDT) for generously funding my PhD and supporting me throughout my degree.

To my partner, Katherine, thank you for never-ending support, your understanding and for helping me be the best version of myself. To my family, Mama, Papa, Clara and Katherine, thank you for being patient, for caring for me and supporting me with home-cooked meals throughout the ups and downs of the past four and a half years. Finally, to my friends in El Vagon, RdM, the Imperial Fleet, Bell Burnell & the Pulsars, Mighty Morags FC, the Stevens Group and the CDT, thank you for the beers, the jams, the talks and the laughs.

Abstract

The rise of nanotechnology has to led numerous developments in the fields of biotechnology and medicine. The promise of nanoparticles delivering drugs *in vivo* and nanomaterials peering into cells are highly sought after and currently investigated in research groups around the world. However, despite the potential of such technologies, much is still unknown about the interface between these materials and the biological world. This thesis aims to further our understanding of this interface in order to aid the design of future generations of materials with new and improved functionality.

Coarse-grained molecular dynamics simulations were employed to study how nanoporous surfaces can affect model cell membranes in close contact. This modelling showed that curvature can be induced in membranes by fine-tuning nanoporous surfaces leading to preferential local changes in membrane properties and preferential localization of proteins. This model was expanded to study in further detail the membrane binding and curvature sensing of a key curvature-active protein domain, the Epsin N-Terminal Homology (ENTH) domain. This protein was shown to be able to sense membrane curvature without its terminal H0 amphipathic helix both with and without the presence of its key lipid binding partner, phosphatidylinositol 4,5-bisphosphate (PIP2). In addition, another PIP2-binding, curvature-active protein, the AP180 N-Terminal Homology (ANTH) domain, was investigated with this modelling system in order to evaluate the curvature-sensitivity of the domain with three different terminal helix compositions. This domain was shown to have innate curvature sensitivity on neutral membranes. In the presence of PIP2 however, only the fully rigid helix structure allowed for curvature sensing of this protein.

In addition to modelling approaches to understand the bio-nano interface, x-ray photoelectron spectroscopy (XPS) was employed to characterize the surfaces of nanostrutured silicon surfaces in order to understand their surface chemistry for biological applications. Gold nanoclusters (AuNCs) were also studied in order to explore the nature of catalytic reactions occurring on their surface.

Publications & Conference Presentations

There is content in this thesis derived from peer-reviewed journal articles.

Chapter 1 contains work that has been published in:

> S. G. Higgins, M. Becce, **A. Belessiotis-Richards**, H. Seong, J. E. Sero & M. M. Stevens. "High-Aspect-Ratio Nanostructured Surfaces as Biological Metamaterial" *Advanced Materials*, 1903862, 2020

Chapter 2 is adapted from the following publication:

> **A. Belessiotis-Richards**, S. G. Higgins, B Butterworth, M. M. Stevens & A. Alexander-Katz. "Single-nanometer changes in nanopore geometry influence curvature, local properties and protein localization in membrane simulations" *Nano Letters* **19** (7), 4770-4778, 2019

Chapters 3 is adapted from the following publication:

> **A. Belessiotis-Richards**, S. G. Higgins, M. S. P. Sansom, A. Alexander-Katz & M. M. Stevens. "Coarse Grained Simulations Suggest the Epsin N-Terminal Homology Domain Can Sense Membrane Curvature Without its Terminal Amphipathic Helix" *ACS Nano*, **14** (12), 16919-16928, 2020

Chapters 4 is in preparation for publication as:

> **A. Belessiotis-Richards**, A. H. Larsen, S. G. Higgins, M. S. P. Sansom, A. Alexander-Katz & M. M. Stevens. "Simulations Suggest Phosphoinositides and Amphipathic Helix Structure Play Opposing Roles in Membrane Curvature Sensing of the AP180 N-Terminal Homology Domain"

The work presented in this thesis was selected for oral presentations at the following conferences:

> Biophysical Society 62nd Annual Meeting (Spring 2018)
>
> Gordon Research Seminar on Self-Assembly & Supramolecular Chemistry (Summer 2019)

Other publications from the PhD that are not included in this thesis research include:

Y. Xianyu, Y. Lin, Q. Chen, **A. Belessiotis-Richards**, M. M. Stevens & M. R. Thomas. "Iodide-Mediated Rapid and Sensitive Surface Etching of Gold Nanostars for Biosensing" *Angewandte Chemie* **60**, 1-7, 2021

M. Penna, K. J. Ley, **A. Belessiotis-Richards**, S. MacLaughlin, D. A. Winkler & I. Yarovsky. "Hydration and Dynamics of Ligands Determine the Antifouling Capacity of Functionalised Surfaces" *The Journal of Physical Chemistry C* **123** (50), 30360-30372, 2019

N. Kim, M. R. Thomas, M. S. Bergholt, I. J. Pence, H. Seong, P. Charchar, N. Todorova, A. Nagelkerke, **A. Belessiotis-Richards**, D. J. Payne, A. Gelmi, I. Yarovsky & M. M. Stevens. "Surface Enhanced Raman Scattering Artificial Nose for High Dimensionality Fingerprinting" *Nature Communications* **11**, 207, 2020

Scope of the Thesis

Chapter 1 introduces key concepts and background literature around the use of nanotechnology for biological applications. In particular, the use of nanostructured materials and their interface with cells is explored as it was a key inspiration for the work undertaken in this thesis. This chapter also introduces background methods and literature on molecular dynamics simulations and x-ray photoelectron spectroscopy.

Chapter 2 examines the use of nanoporous substrates as a means to manipulate cell membranes and drive membrane curvature using coarse-grained molecular dynamics simulations. Design rules for nanoporous wafers are established and nanomaterial-driven changes in membrane characteristics are characterised. In addition, the biological impact of nanopore-induced membrane curvature is explored through protein localization simulations.

Chapter 3 studies how a key curvature-sensing protein, the epsin N-Terminal Homology (ENTH) Domain, interacts with curvature. This chapter explores the effect of the ENTH domain's terminal amphipathic helix on its ability to sense curvature as well as the presence of an elastic network to rigidify the proteins tertiary structure. Furthermore, protein binding is measured on three different membrane compositions.

Chapter 4 investigates how another key curvature-sensing protein, the AP180 N-Terminal Homogology (ANTH) Domain, binds and interacts with membrane curvature. This chapter explores three different terminal amphipathic helix structures of the ANTH domain and evaluates their contribution to curvature sensing of the protein on two membrane compositions.

Chapter 5 presents examples of the application of X-ray photoelectron spectroscopy (XPS) to nanomaterial surface characterization. In particular, the surfaces of silicon nanoneedles are characterized for applications in drug delivery and cellular interfacing. In addition, this chapter presents results on the use of XPS to study the surface chemistry of catalytic gold nanoclusters.

Finally, **Chapter 6** concludes the thesis and summarizes the major findings. This chapter presents an outlook on the where the thesis work lies within the current literature as well as covers some of state-of-the-art research endeavours ongoing in the field of computational modelling of membrane and protein processes.

Contents

1 Introduction **11**

1.1 Nanotechnology Applied to Biology 11

1.2 Characterisation of Interfaces 13

1.2.1 Molecular Dynamics Simulations 13

1.2.2 X-ray Photoelectron Spectroscopy 17

1.3 The Cell Membrane & Curvature 25

1.3.1 Cell Membrane Curvature 26

1.3.2 Endocytosis 28

1.3.3 Modelling Cell Membrane Curvature 32

1.3.4 Nanomaterials That Influence the Cell Membrane 33

2 Membrane Curvature Driven by Nanoporosity **37**

2.1 Introduction 37

2.2 Methods 41

2.2.1 Simulations Details 41

2.2.2 Nanoporous Wafer Construction 42

2.2.3 Curvature Evaluation 42

2.2.4 Membrane Analysis 44

2.3 Results & Discussion 47

2.3.1 Curvature Control of Model Cell Membrane 47
2.3.2 Analysis of Membrane Properties 51
2.3.3 Biological Implications of Curvature 57
2.4 Outlook & Conclusion 60

3 Membrane Curvature Binding and Localization of the ENTH Domain 61
3.1 Introduction 61
3.2 Methods 67
3.2.1 Simulation Details 67
3.2.2 Trajectory Analysis 67
3.2.3 Structural Analysis 68
3.2.4 Wafer Construction 68
3.3 Results & Discussion: 69
3.3.1 Characterization of Membrane Curvature 69
3.3.2 Curvature Sensing of the ENTH Domain 69
3.3.3 Lipid Binding of the ENTH Domain 73
3.3.4 Structural Dynamics of the Flexible ENTH Domains 75
3.4 Conclusion & Outlook 83

4 Membrane Curvature Binding and Localization of the ANTH Domain 84
4.1 Introduction 84
4.2 Methods 88
4.2.1 Simulation Details 88
4.2.2 Trajectory Analysis 88
4.3 Results & Discussion 89
4.3.1 Characterisation of Membrane Curvature 89

4.3.2 Protein Localization 89

4.3.3 Hydrophobic Binding 90

4.3.4 PIP2 Binding 92

4.4 Conclusion & Outlook 99

5 Characterisation of Biologically Relevant Surfaces via XPS 100

5.1 Introduction 100

5.1.1 XPS and Biological Surfaces 101

5.2 Methods 103

5.3 Results & Discussion I:
Surface functionalisation of Silicon Nanoneedles 104

5.4 Results & Discussion II:
Hydrogen Peroxide Disproportionation by Gold Nanoclusters 112

5.5 Conclusion & Outlook 118

6 Conclusion 119

6.1 Conclusions & Future Scope 119

6.1.1 Membrane Composition 121

6.1.2 Protein Localization 122

6.1.3 Surface Chemistry 125

6.2 Summary 126

6.3 Perspective 127

List of Tables

3.1 Summary of All Simulations Performed 65

4.1 Summary of the simulations systems investigated in this work 87

List of Figures

1.1 Schematic of a basic molecular dynamics algorithm. 14

1.2 Schematic showing the timescales of typical biological processes from the atomic to the cellular scale. 15

1.3 Schematic of the Martini coarse-grained representations. 17

1.4 Comparison of atomistic and Martini coarse-grained representations of biological systems. 18

1.5 Schematic of an x-ray photoelectron spectroscopy (XPS) instrument. . . . 19

1.6 Example of a survey spectra of a sample collected using XPS. 20

1.7 Example of C *1s*, N *1s* and Si *2p* core level spectra of a sample collected using XPS. 22

1.8 Schematic of the effects of incident x-range angle on XPS spectra. 23

1.9 Schematic of a cell membrane showing its main components. 25

1.10 Three-dimensional schematic of a cell membrane. 26

1.11 Schematic of a cell highlighting regions of membrane curvature. 27

1.12 Schematic of different mechanisms of membrane curvature generation in cells. 28

1.13 Schematic of clathrin-mediated endocytosis. 29

1.14 Schematic of phosphoinsositide levels during endocytosis. 31

1.15 Simulation snapshots of membrane curvature generation by proteins. . . . 33

1.16 Experimental examples of the biological impact of membrane curvature. . 35

2.1 Schematic of Nanoporous Subrate Driven Membrane Curvature 39

2.2 Schematic of Membrane Curvature Profile and Fit 43

2.3 Curvature Profiles and Fits under Different Nanopore Conditions 47

2.4 Curvature Profiles of All Nanoporous Wafer Conditions 48

2.5 Curvature Values of All Nanoporous Wafer Conditions 48

2.6 Parameter Matrix of Nanopore Design Effect on Membrane Curvature . . 49

2.7 Curvature Evaluation for Cholesterol-Containing Membranes 50

2.8 Membrane Properties in Contact with Nanoporous Substrates 52

2.9 Lipid Orientation Heat Maps under All Nanopore Conditions 53

2.10 Area-Per-Lipid Heat Maps under All Nanopore Conditions 54

2.11 Membrane Thickness Heat Maps under All Nanopore Conditions 55

2.12 Lipid Movement Heat Maps under All Nanopore Conditions 56

2.13 Curvature Comparison of Explicit and Implicit Solvent Models 57

2.14 Protein Localization to Curved Membrane 59

2.15 Protein Structure & Characterization 59

3.1 Schematic and Introduction of Model 63

3.2 Comparison of ENTH Domain Crystal Structures 66

3.3 Additional Snapshots of Simulation System 66

3.4 Membrane Properties & Characterisation 69

3.5 ENTH Domain Localization Results 71

3.6 Raw Histograms of Localization Data 72

3.7 Membrane Binding of all Residues of ENTH Domain 74

3.8 Sequence and Secondary Structure of ENTH Domain 76

3.9 Snapshots of ENTH Domain Interacting with Curvature 77

3.10 Membrane Binding of ENTH Domain to Flat Membranes 78

3.11 Structural Characterization of ENTH Domain 79

3.12 Snapshots and Strucural Dynamics fo ENTH Domains 80

3.13 Snapshots of ENTH Domain Highlighting Flexible Helix 81

3.14 Summary Schematic 82

4.1 Schematic of Simulation Model 86

4.2 Characterisation of Membrane Properties 89

4.3 Membrane Localization of ANTH Domain 90

4.4 Raw Histograms of Membrane Localization Data 91

4.5 Hydrophobic Interactions of ANTH Domain 92

4.6 PIP2 Interactions of ANTH Domain 93

4.7 Lipid Interactions of all residues of ANTH Domain 94

4.8 Snapshots of ANTH Domain on PC Membranes 95

4.9 Snapshots of ANTH Domain on PIP2 Membranes 96

4.10 Angular Rotation of ANTH Domains 97

4.11 Summary Schematic 98

5.1 Oxidation of silicon surfaces 105

5.2 Schematic of silicon surface treatments 105

5.3 Effect of oxidation protocol on APTES functionalisation of silicon surfaces 106

5.4 XPS of silicon surfaces during APTES functionalisation 107

5.6 Silicon surfaces functionalised with chitosan-heparin 109

5.7 Silicon surfaces functionalised with DNA 110

5.8 Silicon surfaces functionalised with DNA 111

5.9 Schematic of the AuNC diagnostic system 113

5.10 Chemical structure of GSH 113

5.11 Schematic of thiolated AuNCs 114

5.12 XPS Spectra of AuNCs under Different Peroxide Concentrations 114

5.13 S2p Spectra Comparison of pure GSH and AuNCs 115

5.14 C1s Spectra Comparison of pure GSH and AuNCs 116

5.15 S2p Spectra of AuNCs with GSH 117

6.1 Snapshots of a large-scale liposome simulation. 120

6.2 Snapshot of a complex composition membrane. 122

6.3 Crystal structure, top-down localization heatmap and relative fold change of other proteins studied. 124

Chapter 1

Introduction

1.1 Nanotechnology Applied to Biology

The advent of nanotechnology has brought many new potential technologies to the forefront of research and industry. Ranging from the miniaturization of silicon microelectronics to the development of nanomedicine platforms, the potential applications are vast. As its name suggests, the advantage and interest in nanotechnology relates to its scale. A key aspect of being able to fabricate at the nanoscale is the ability to directly interact with physical processes that occur naturally in the nanometre range. An interesting example of such an application is in biology and medicine. Indeed, the average size of most biomolecules and proteins is in the 10s of nanometres, [1] and cells respond and react to micro and nanoscale cues within the body. By exploiting nanotechnologies, we now have the ability to directly manipulate individual proteins and cells at the scale of life's tool kit. Such technologies have many outlets in the field of biology and medicine in particular with regards to the development of drug delivery platforms.

In the literature, a key focus of interfacing nanotechnology with cellular life has revolved around affecting the environment that surrounds the cell. Cells interact with the tissue that surrounds them, known as the extra-cellular matrix (ECM), which they secrete, modify and live in. This environment is often micro and nanostructured, and cells take cues from these topographical signals in different ways. For example, cell behaviour can be controlled through physical as well chemical nanopatterning of their culture substrates. [2–6] Another example is the strong dependence of stem cell fate on the stiffness of their culture substrate. [7–13] Nanomaterials have also been extensively employed to measure and stimulate electrical pathways in neuronal, [14–17] as well as cardiac cells. [18–20] Nanoparticles and nanotextured materials have also found a large audience as vectors for

drug delivery to cells both *in vitro* and *in vivo*. [21–24]

The breadth of research into this field is very large and many more examples of cell/environment interactions can be described at length. This thesis however, aims to explore the interface between nanotechnology and biology. The scope of this thesis focusses on exploring this interface through the use of computational methods, in particular, coarse-grained molecular dynamics (MD) simulations and x-ray photoelectron spectroscopy (XPS). In particular, this thesis investigates how cell membranes interface with and are manipulated by nanotextured environments. This involves performing coarse-grained molecular dynamics simulations to study how nanoscale curvature can be generated in cell membranes through interaction with nanoporous substrates in Chapter 2. Subsequently, the biological effects of such membrane curvature is investigated through the study of two curvature-sensitive proteins in Chapters 3 and 4, the ENTH and ANTH domains respectively. Finally, in Chapter 5, x-ray photoelectron spectroscopy (XPS) is employed to study the surfaces of nanomaterials with applications in biomedicine. This chapter will set the scene for this thesis research by summarizing the background to the techniques employed and covering the relevant literature of research in this field.

1.2 Characterisation of Interfaces

At the nanoscale, all interactions between bodies are mediated by surface properties. The success of a medical implant, development of a biosensing platform and culturing of cells can all be explained through surface-mediated phenomena. [25] As such, to understand how a nanoparticle will behave in the body or a nanotextured surface will affect a cell, we must first develop and hone the tools for understanding their surfaces. In the scope of this thesis, two methods were employed to characterize the surfaces of nanotechnological materials for biological applications; x-ray photoelectron spectroscopy & molecular dynamics simulations. Here the fundamentals behind both techniques are briefly introduced.

1.2.1 Molecular Dynamics Simulations

Molecular dynamics (MD) simulation is a powerful tool for studying nanoscale processes with atomic resolution. The technique can be traced back to 1957 with the first simulation of a protein occurring in 1976. [26, 27] As it's name suggests, MD is used for observing the movement and interactions (dynamics) of atoms and molecules in systems containing hundreds to even millions of atoms. While the technique was first limited to simulating a single protein for a few picoseconds, now MD simulations have been stretched to microsecond time scales and even to simulating vesicles and larger biomolecular assemblies. [28–32]

Basics of MD Simulations

MD simulations rely on integrating Newton's equations of motion to predict the position of atoms or particles of interest as a function of time. The main assumption guiding these simulations is that the motion and interaction of atomic nuclei can be described using classical mechanics. At any given time point, we know the spatial position and velocities of all atoms in a simulation. From this information, we can calculate the forces exerted on each atom by the other atoms in a system. Knowing the forces felt by each atom, we can calculate their acceleration and how they might move in the "future", at the next time point, by integrating Newton's equations of motion. This process is then repeated for a given simulation time as seen in Figure 1.1.

The simplicity of MD allows for very diverse set of computational models to be developed in order to study the dynamics of particles at the nano or macroscale. Atomistic MD simulations, where beads are approximated as individual atoms, must be integrated over very small time steps on the order of femtoseconds (10^{-15} s) in order to remain numerically

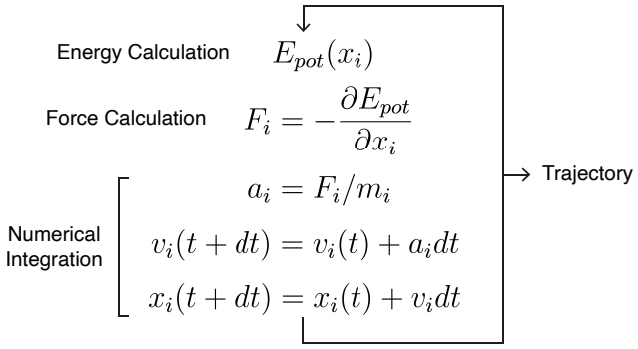

Figure 1.1: Schematic of a basic molecular dynamics algorithm where E_{pot} is the potential energy defined in the forcefield, t is the simulation time, dt is the iteration time. For each i atom in the simulation system, x is the atom coordinates, F is the force, a is the acceleration, m is the atom mass and v is the atom velocity. Redrawn with modifications from Hospital *et al*. [33]

stable. Increasing this time step is limited by the fastest motion within a given system, for example the frequency of oscillation of a bond between two atoms. Reaching long time scales in all-atom simulations, on the order of micro and milliseconds, can be extremely challenging due to the computational cost of running such long simulations. Hence, most biomolecular MD simulations are performed in the nanosecond range. As such, certain phenomena, such as protein folding, will be too lengthy and complex to be captured by a simple MD simulation.

Most condensed matter physics systems can make due with these time constraints to represent physical processes. In biology, however, timescales can be much longer than the femto to micro second range accessible by MD. [34] Figure 1.2 shows the timescales available to MD simulations as compared to atomic, molecular and cellular processes in biological systems. This Figure makes clear that atomistic MD simulations can model a fairly wide range of processes but is not ideal for more macroscopic mechanisms like protein folding and motion for example. In order to account for this, researchers have developed a number of more advanced sampling techniques to improve the base MD algorithm in order to study rare or slow events, this includes free energy techniques such as metadynamics and umbrella sampling for example. [35, 36]

The inter- and intra-molecular forces in a MD simulations are determined by a force-field which determines how atoms in a simulation will interact. Traditionally, this force-field is parametrized in order to either replicate quantum mechanical calculations and/or experimental measurements of given materials but it can be defined depending on the problem of interest. The selection of a suitable force-field for a given system is a crucial element of MD simulations, whereby all observed results will be dependent on the accu-

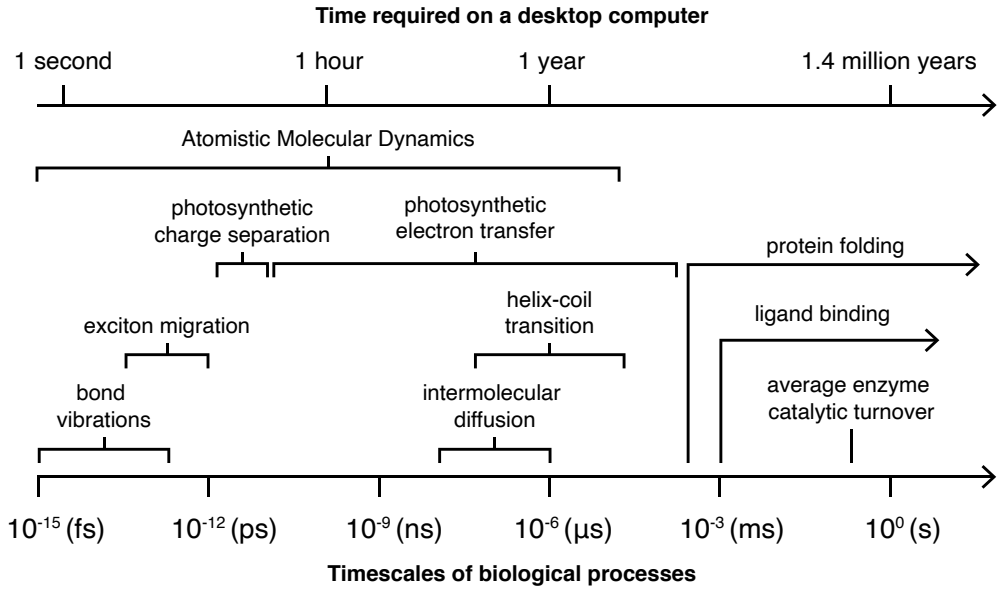

Figure 1.2: Schematic showing the timescales of typical biological processes from the atomic to the cellular scale as compared to Molecular Dynamics. Redrawn with modifications from *Cell Biology by the Numbers* and Zwier *et al.* [1, 37]

racy/appropriateness of the chosen force-field. Such force-fields can never be completely accurate unfortunately as we are inherently looking at the dynamics of hard particles which we approximated to be a physical atom or molecule. Furthermore, basic MD simulations do not allow for the breaking or forming of chemical bonds. The most common force-field for biomolecular simulations is probably the Chemistry at HARvard Macromolecular Mechanics (CHARMM) force-field first published in the early 1980s. [38]

Once a suitable and validated force-field is found, MD simulations allow us to gain valuable insight into the atomic and nanoscopic state of a system. In these simulations, the positions of all atoms are known and can be visualized in three dimensions. In essence, MD simulation can act as a "virtual microscope", allowing us to gain information that would be nearly impossible to ascertain with experimental means. Despite this, one should note that the trajectories in MD simulations are not finite representations of reality. Each simulation will give a different trajectory and these will diverge exponentially with time. Hence, observations from trajectories need to be statistically averaged in order to create an ensemble view of a given problem.

Molecular Dynamics of Membranes

Atomistic simulations have been extensively used to study lipid membranes. The first examples of such simulations can be traced back to the early 1980s. [39, 40] These simulations have allowed for a large field of membrane biology to be explored ranging from the physical properties and phase diagrams of lipidic membranes, [41–43] to studying membrane proteins and ion channels, [44–48] as well as protein binding to membranes. [49–51] Due to their computational intensity, atomistic simulations only allow for the study of relatively small regions of membranes (< 10 nm) at short timescales. In the scope of this thesis, we are interested in investigating membrane interactions with nanomaterials at larger length and timescales.

Coarse Grained Molecular Dynamics

A potential solution to the stringent computational requirements of some membrane systems is the use of an additional simplification technique known as coarse-graining. Coarse-Grained MD (CGMD) is a fairly common adaptation of MD force-fields whereby groups of atoms are collected into discrete groups that behave uniformly (in essence as a single body). For example, the Martini coarse-grained force-field approximates every 4 heavy atoms to a single CG bead. [52] If done correctly coarse-graining conserves the overall properties of a molecule (a lipid or protein for example) while greatly reducing its complexity and computational cost. Although there are no definite rules for how groups of atoms should be coarse-grained, in general coarse-graining is used to approximate different chemical groups within a molecule (residue-based coarse-graining) or to reproduce the overall shape of a molecule (shape-based coarse-graining). [53] Some recent advances in CG force-fields is the application of machine learning technique to parametrize these force-fields without the need for arbitrary selections. [54]

In simulations of biological systems, water molecules take up a huge amount of computational power. Coarse-graining can also reduce the performance load of water by simplifying the representation of water. Four water molecules make up a single CG bead in Martini force-field for example (see Figure 1.3). [52] Analogous to the heavy computational load of water molecules, a number of researchers have developed force-field which use implicit solvent models where water molecules are removed entirely. [55–57] Figure 1.4 shows some examples of coarse-grained representations of lipid and protein systems. Furthermore, recent advances in computational methods have allowed for the development of multiscale simulations techniques which can simultaneously combine atomistic and

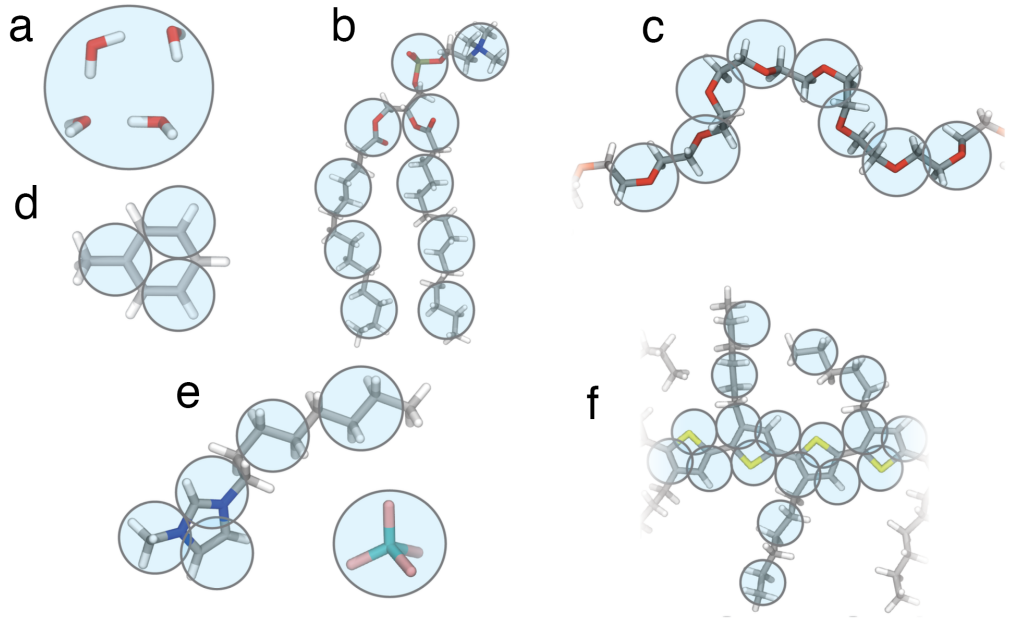

Figure 1.3: Atomistic and Martini coarse-grained representation of (a) a standard water particle representing four water molecules, (b) a DMPC lipid, (c) PEO, (d) toluene, (e) an ionic liquid ($[C8Imim]^+[BF4]^-$), (f) a conductive polymer (P3HT). Adapted with permission under a Creative Commons License from Alessandri *et al.* [60]

coarse-grained detail. [58, 59] Hence, coarse-grained simulations allow for fairly large-scale simulations of lipid bilayers and serve as an excellent tool for the study of dynamic membrane deformation.

1.2.2 X-ray Photoelectron Spectroscopy

Developed in the early 1950s after the discovery of photoemission, X-ray Photoelectron Spectroscopy (XPS) is one the most used characterization technique for high sensitivity surface analysis. Sometimes called electron spectroscopy for chemical analysis (ESCA), this technique provides both qualitative and quantitative information about the surface chemistry of a material. Kai Siegbahn was awarded the 1981 Nobel Prize in Physics for developing the instrumentation and methodology to employ photoemission as an analytical technique.

XPS relies on the the photoelectric effect. A sample is bombarded with a photon beam which interacts with the electron cloud of surface atoms as shown in Figure 1.5. A fraction of the incident photons will interact with electrons in the sample, transferring their energy directly to these electrons. If the incoming beam energy is larger than the binding energy, an electron can be ejected from the sample as a photoelectron. The kinetic energy of these

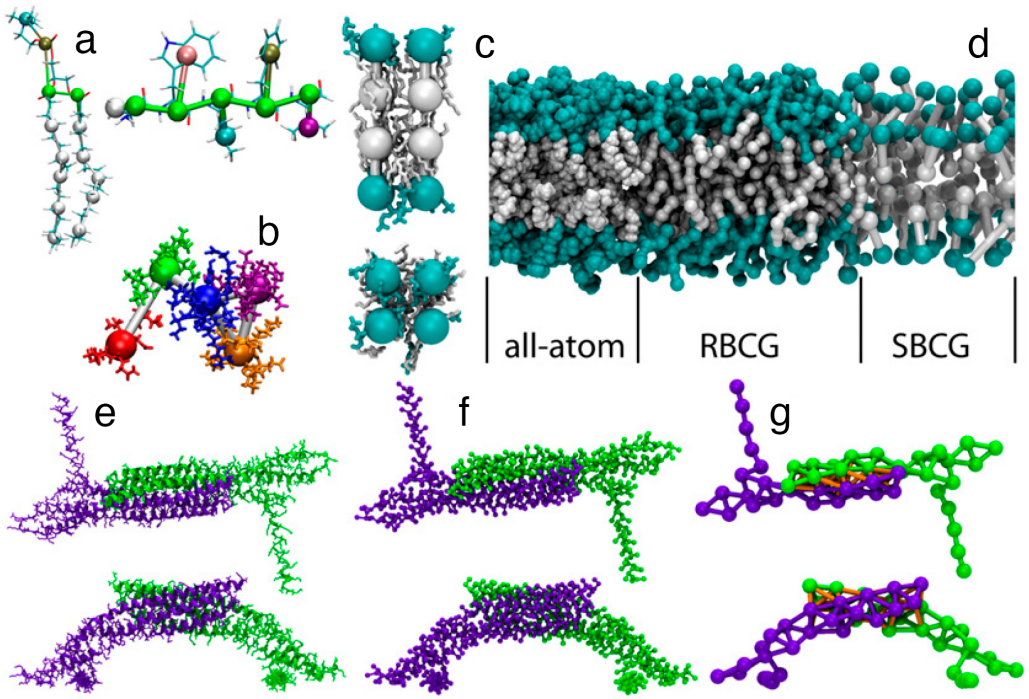

Figure 1.4: (a) Overlayed atomistic and coarse-grained representations of a lipid and peptide with about ten atoms per CG bead. (b) CG representation of a peptide segment using approximately 150 atoms per CG bead. (c) and (d) side and top-down views of a membrane patch modelled atomistically, using residue-based coarse-graining (RBCG) and shape-based coarse-graining (SBCG). Side and top-down view of (e) all-atom, (f) RBCG, and (g) SBCG representation of a BAR domain protein. Adapted with permission from Arkhipov *et al.* [53] Copyright 2008, Elsevier.

ejected electrons can then be measured in a spectrometer (often a hemispherical analyzer such as in Figure 1.5) and a spectra of counts against energy is generated. Note that we use an electron's binding energy (E_B) as its characteristic energy because its kinetic energy (E_K) is dependent on the energy of the incident X-rays ($h\nu$). Photoelectrons are counted and their energy converted following:

$$E_B = h\nu - E_K - W \tag{1.1}$$

Where h corresponds to the Planck constant, ν to the frequency of the incident x-rays and W to the work function of the sample. [61] Hence, in order to produce photoelectrons with enough kinetic energy to be measured, the sample must be subjected to photons of energy larger than the binding energy and work function combined. Monochromated x-rays generated from aluminum (Al) Kα band are the most commonly used photon source in XPS. [62]

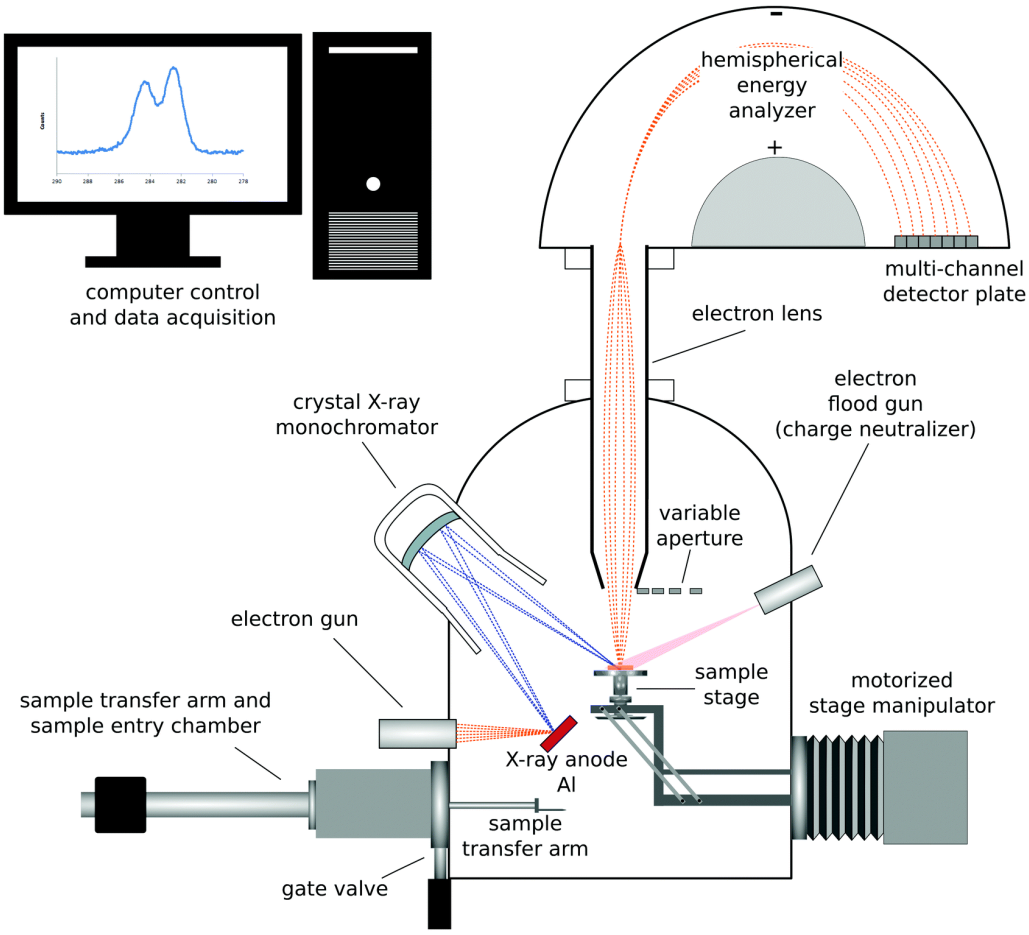

Figure 1.5: Schematic of an x-ray photoelectron spectroscopy (XPS) instrument with hemispherical analyzer. Reproduced with permission. [62] Copyright 2020, Royal Society of Chemistry.

One of the key advantages of XPS is its very high surface sensitivity. Indeed, despite being bombarded with high energy x-rays which can penetrate relatively deep into samples, excited photoelectrons can only escape the sample from a thin surface layer. Photoelectrons excited deeper into the sample interact with surrounding atoms and are scattered before escaping. The depth from which photoelectrons can escape, known as the attenuation length λ, depends on multiple factors – namely E_K and the inelastic mean free path – and is strongly limited to the first 2 to 10 nanometres of a sample's surface. [62] This very low sampling depth might seem like a limitation, however, it enables the technique to be incredibly sensitive to details at the sample's surface. Many biological, physical and chemical processes are limited or constrained to material surfaces, such as catalysis, chemical reactions, oxidation events, adherence/adsorption of species. Hence, XPS gives us the opportunity to investigate these processes with high sensitivity.

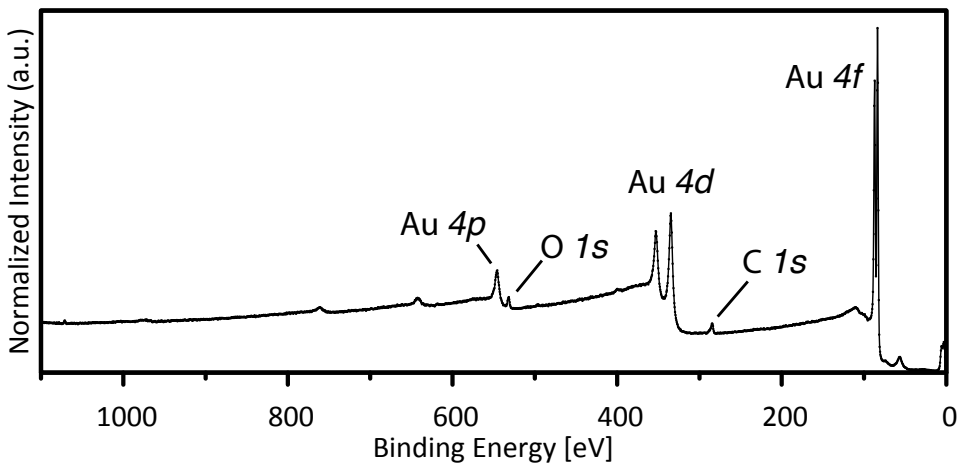

Figure 1.6: Example of a survey spectra of a sample collected using x-ray photoelectron spectroscopy (XPS).

When first analysing a sample in XPS , a survey spectra is generated. This involves bombarding the sample with x-rays and collecting electrons with a binding energy between 0 to 1300 eV. An example survey spectrum is shown in Figure 1.6. In this Figure we can see sharp peaks picked up by the XPS machinery. These usually correspond to core electrons ejected from atoms in the sample. These core electrons have specific energies depending on what element they come from and their appearance in an XPS spectra is known as a core level. As such, we can identify which elements are present in the sample surface simply from looking at the survey spectrum and matching up the binding energies to known elements. XPS can detect all elements from the surface of a sample except Hydrogen and Helium. It should be noted that XPS also collects electrons generated from valence bands, electrons that have lost energy through scattering events as well as Auger electrons. These electrons often appear as broad peaks in the spectrum and contribute to the background signal.

After collecting a survey scan, the elements present on a surface are known. We can now isolate an energy range, usually the core level of an element of interest, and perform a detailed scan at higher energy resolution. These scans can now provide more detailed information on the chemical groups present in the sample surface. Figure 1.7 shows Si *2p*, C *1s* and N *1s* core level scans for a sample. The core levels of a pristine element will change depending on its binding environment, leading to shifts in their energies. Hence,

when looking at a given core level, there may be a series of often overlapping peaks present corresponding to the different chemistries present in the sample. These core level are often analyzed and fitted to a particular set of Gaussian-Lorentzian curves which are convolved to reproduce the measured peaks as accurately as possible. The mathematical description of XPS peaks allow us to deconvolute overlapping or chemically shifted peaks. In Figure 1.7, we can see that the signal has been deconvoluted into individual subpeaks which correspond to given chemical groups. For example, C=O and C-N bonds have been identified in the sample from the C *1s* signal while both metallic silicon and silicon oxide have been detected from the Si *2p* signal. Furthermore, peak fitting allows us to obtain quantitative estimates of sample composition. For example, from the area under fitted peaks in the Si *2p* signal from Figure 1.7, we can estimate, in relative terms, the amount of oxide present on the surface of a wafer compared to that of the pure material.

While identifying chemical groups from XPS spectra is relatively simple in this example, this can be a significant challenge, in particular when dealing with samples of unknown origin. Knowing the chemical structure of the materials in use as well as the processing steps involved is crucial to being able to make sense of XPS spectra. Any number of peaks can be fitted underneath an XPS spectrum, as such one must always make reference to the known chemical knowledge of the sample in order not to incorrectly fit and wrongly interpret the signal.

In addition to being able to identify elemental compositions and deconvolute chemical shifts in a sample, XPS instruments can be expanded to perform depth composition analyses. By tilting a sample during analysis, we can restrict the collection of photoelectrons to an even thinner surface layer. This technique, known as Angle Resolved XPS (ARXPS), is shown schematically in Figure 1.8. ARXPS is a common modification of XPS devices which allows for sample rotation during analysis enabling even more restrictive sampling depth of photoelectrons to the very top atomic layers of the surface. Figure 1.8 shows schematically the evolution of the core level electron peaks for a metal and its surface oxide as we change the incidence angle of incoming x-rays. This technique could also be very relevant in studying the spatial localization of surface proteins or functionalization molecules onto surfaces after interacting with cells.

Limitations of XPS and HiPPES

Due to the sensitivity and specificity of the technique, XPS requires an ultra-high vacuum (UHV) environment in order to avoid sample contamination. Indeed, UHV enables measurements to be performed in a time-frame which limits the formation of contaminants

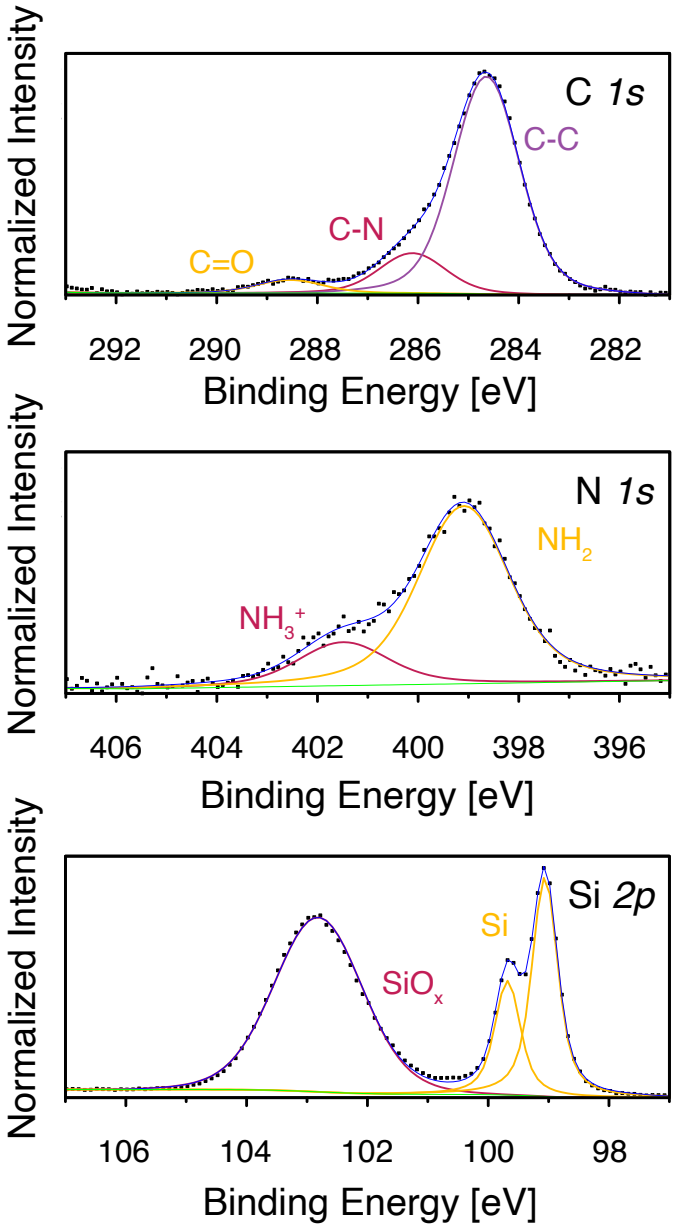

Figure 1.7: Example of C *1s*, N *1s* and Si *2p* core level spectra of a sample collected using x-ray photoelectron spectroscopy (XPS) showing deconvoluted peaks to highlight different chemical groups. The black dots represent the raw XPS signal while coloured lines are functions fitted to the data.

on the sample surface from the surrounding atmosphere. Due to the surface specificity of this technique and its very high sensitivity, samples and measurements are highly prone to contamination. UHV is also required so as to allow the generated photoelectrons to safely

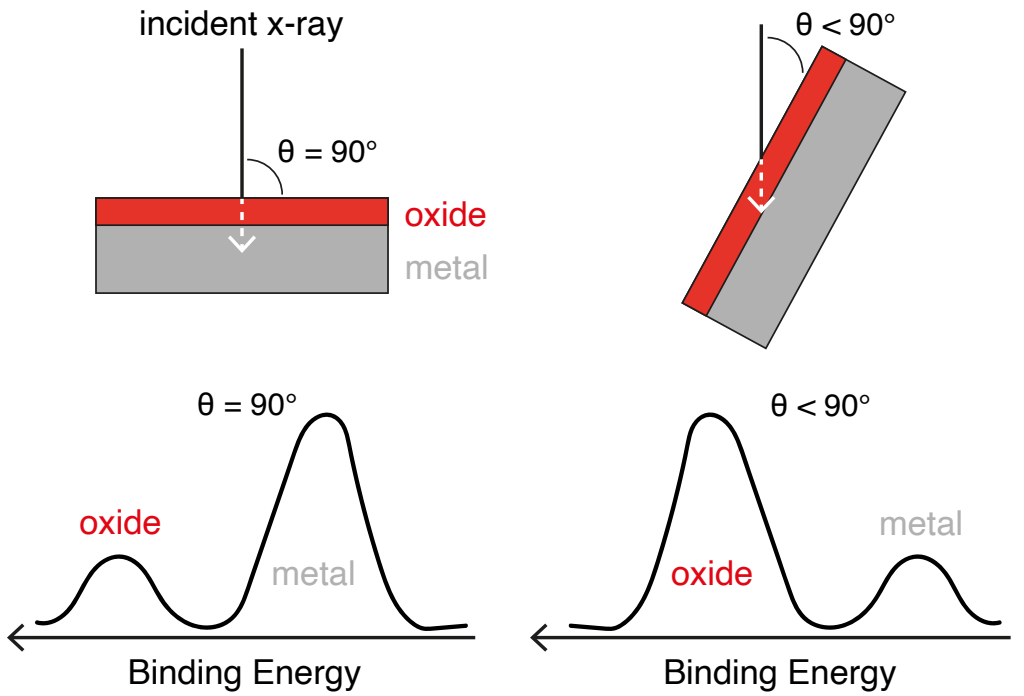

Figure 1.8: Schematic of the effects of incident x-range angle on XPS spectra showing increased sensitivity of the oxide peak of a metal sample as it is tilted nearly parallel to the x-ray source. Redrawn with modifications from Mazzotta *et al*. [63]

reach the spectrometer without being scattered by gas molecules in the chamber. Using such high vacuum analysis, however, limits the validity of measurements when compared to physical phenomena. For example, biological and cellular samples are almost always in an aqueous environment. This is also true of many catalysts. Pumping such materials down to UHV can damage samples (and the XPS machinery via outgassing of contaminating elements, such as fluorine) as well cause loss of information with regards to proteins and biomolecules which are dissolved or unstable in vacuum.

To generate more precise and realistic data, we can apply a variation on XPS known as High Pressure Photoelectron Spectroscopy (HiPPES) or Ambient Pressure XPS (APXPS). A very novel device, this modification allows us to perform photoelectron analyses at much higher pressures. Many HiPPES devices can be used to perform measurements up to 25 mbar of pressure (compared to pressures below 10^{-8} mbar in UHV). [64] The pressure in an APXPS analysis chamber can reach tens of mbar but the pressure in the hemispherical analyzer (where photoelectrons are measured) will still be under UHV. Such devices are designed such that the generated photoelectrons from the sample gradually feel a decrease in pressure as they travel from the analysis chamber to the hemispherical analyzer. This

is done by differential pumping along the length of the tube which gradually reduces the pressure to enable accurate measurement of the generated photoelectrons. Furthermore, the region of high pressure is concentrated tightly onto the sample surface so that photoelectrons are almost instantly in contact with a low-pressure environment once they escape the sample. The advantage of using such devices is to generate stlightly more accurate data for processes which occur under atmospheric pressure, HiPPES is still being conducted at a pressure 40 times lower than atmospheric conditions. These devices also allow the introduction of various gasses into the analysis chamber in order to modify the atmospheric conditions felt by the sample which can be highly relevant for some applications. As the pressure in HiPPES devices is so much higher than UHV, it is thought to be a more appropriate technique for the analysis of samples that are normally hydrated. This is crucial for biological samples which are generally aqueous in nature.

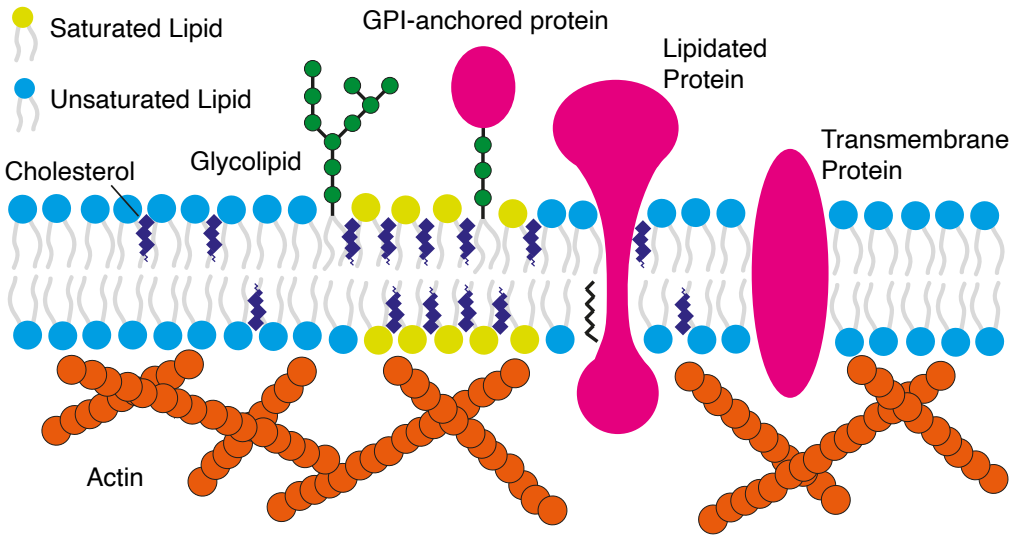

Figure 1.9: Schematic of a cell membrane showing its main components including saturated and unsaturated lipids, cholesterol, glycolipids, GPI-anchored proteins, lipidated proteins and transmembrane proteins. Redrawn with modifications from Sezgin *et al.* [66]

1.3 The Cell Membrane & Curvature

Cells are surrounded by a protective layer known as the plasma membrane. This membrane is a bilayer made-up, for the most part, of amphiphilic molecules known as lipids. These molecules, formed of a polar head and non-polar tail, organize spontaneously into ordered structures in solution. In the body, these molecules naturally form into bilayers in order to expose their hydrophilic headgroups to interstitial fluid and hide their hydrophobic tails. These bilayers are the structural basis for vesicles and plasma membranes and constitute a physical and chemical barrier to molecular diffusion (see Figure 1.9). Indeed, hydrophilic compounds cannot cross the hydrophobic region encapsulated within the bilayers and conversely, hydrophobic molecules can be trapped within this same region. The plasma membrane is made up of three main lipids, phosphoglycerides, sphingolipids. and sterols. [65] These three lipid form the molecular basis for cell membranes but are by no means the only molecules present. Indeed, cell membranes are highly complex structures containing many complementary molecules such as cholesterol and a wide variety of membrane proteins, the latter of which make up around 50% of a membrane's mass (see Figures 1.9 and 1.10). Other similar membranes are found within the cell encapsulating other organelles, most notably the nucleus. These membrane compartments can communicate with another by budding off vesicles from one to fuse with another.

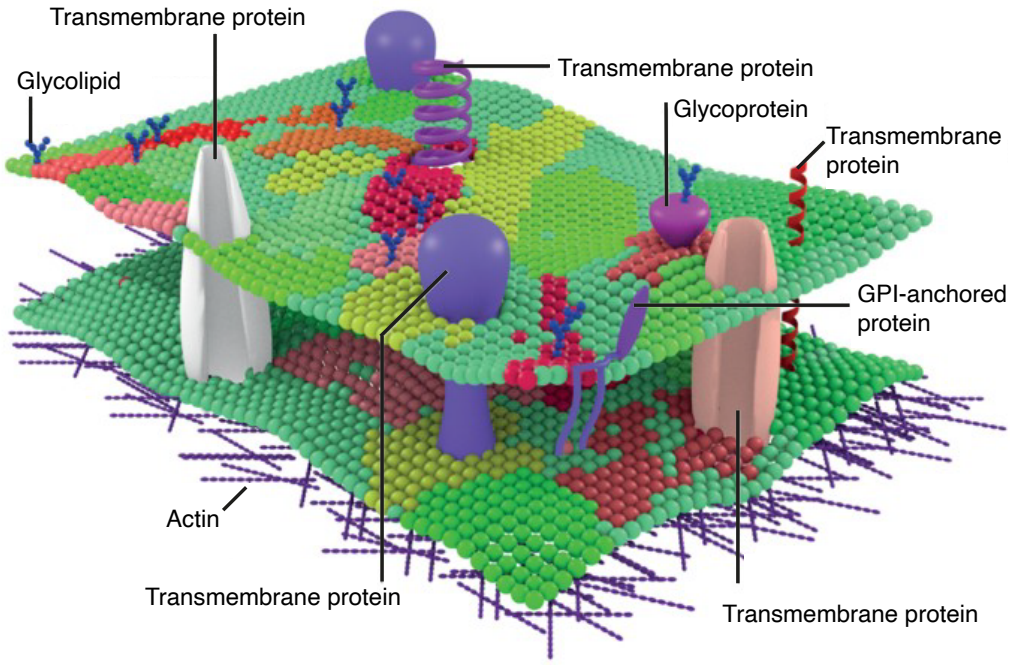

Figure 1.10: Three-dimensional schematic of a cell membrane highlighting the presence of larger non-lipid membrane components. Adapted with permission from Sezgin *et al*. [66] Copyright 2017, Springer Nature.

1.3.1 Cell Membrane Curvature

The cell membrane is a soft material which can be deformed and bent to allow for biological processes to proceed. Cellular movement, attachment and nutrient ingestion all involve significant deformations of the cell membrane. Red blood cells are even thought to change their shape to adapt to the flow rate in blood vessels. [67] Dynamic deformation of the cell membrane occurs during many cellular mechanisms but the cell also contains regions of more static curvature such as in the Golgi apparatus and endoplasmic reticulum. [68] Figure 1.11 shows a schematic of a cell highlighting regions of membrane curvature on the order of tens of nanometers. Such nanoscale membrane curvature plays an important role in membrane-mediated processes such as viral entry into the cell, [69–71] organizing local protein concentrations, [72–75] and controlling protein activity. [76] The functional purpose of such curvature as well as how such curvature is generated and stabilized has been the subject of much research over the years. The recent biomembrane curvature and remodeling roadmap is a testament to the continued interest in this field. [77]

Lipid membranes do have the ability to adapt and change shape dynamically under certain conditions such as osmotic pressure. For example, giant liposomes formed with different

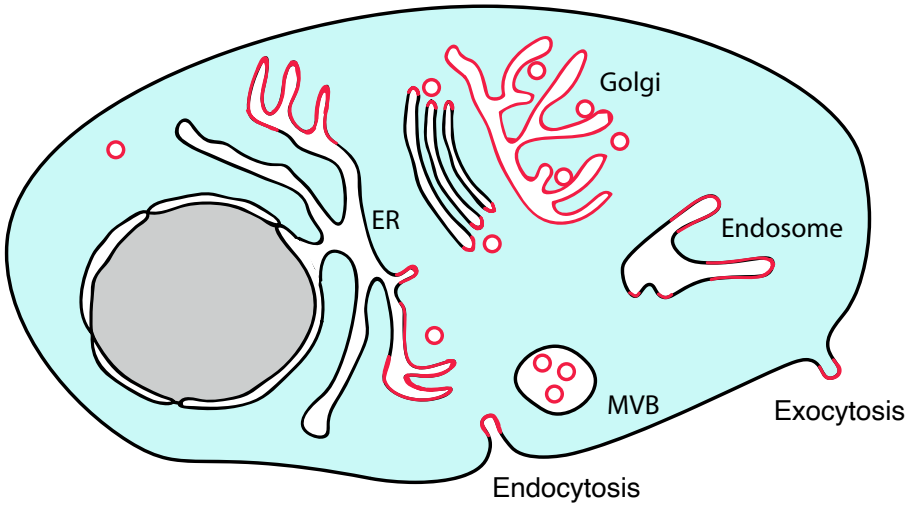

Figure 1.11: Schematic of a cell highlighting regions of membrane curvature in red within the cell membrane. Membrane curvature can be found during endocytosis, exocytosis as well as in organelles such as the endoplasmic reticulum (ER), golgi apparatus, endosomes, multi-vesicular bodies (MVB) and vesicles. Redrawn with modifications from McMahon *et al.* [68]

lipid chemistries can lead to tubule and domain formation which resemble the structures seen in cells. [78, 79] However, this is at a much larger scale (on the order of micrometers) than the nanoscale curvature seen in biology and lipid membranes rarely reproduce such remarkable morphologies *in vitro* as seen within cells. [68] As such, lipid membranes do have some innate ability to form complex shapes but, within the cell, more is at play. Furthermore, as shown in Figure 1.9, the cell membrane is composed not only of lipids but of a wide variety of proteins as well. These proteins, both within the membrane and external to it, are the main drivers of membrane curvature within cells.

Figure 1.12 shows some examples of the mechanisms by which membrane curvature comes about in cells. As described in the giant liposome example above, lipid modifications to membrane systems shown in Figure 1.12a can drive curvature through phase separation. Lipid mismatch has been explored further still both computationally and experimentally, suggesting that certain lipids prefer regions of curvature. [81–86] Curvature can also come about through the clustering of proteins at specific regions of the membrane. For example, membrane proteins might prefer to localize to regions of membrane curvature due to their shape leading to curvature generation as in 1.12b. It has even been shown that curvature can affect transmembrane protein structure and function. [87, 88] Scaffolding proteins such as clathrin or BAR domains, can accumulate on the membrane to stabilize curvature (Figures 1.12d and 1.12e respectively) while proteins with hydrophobic moeities can clus-

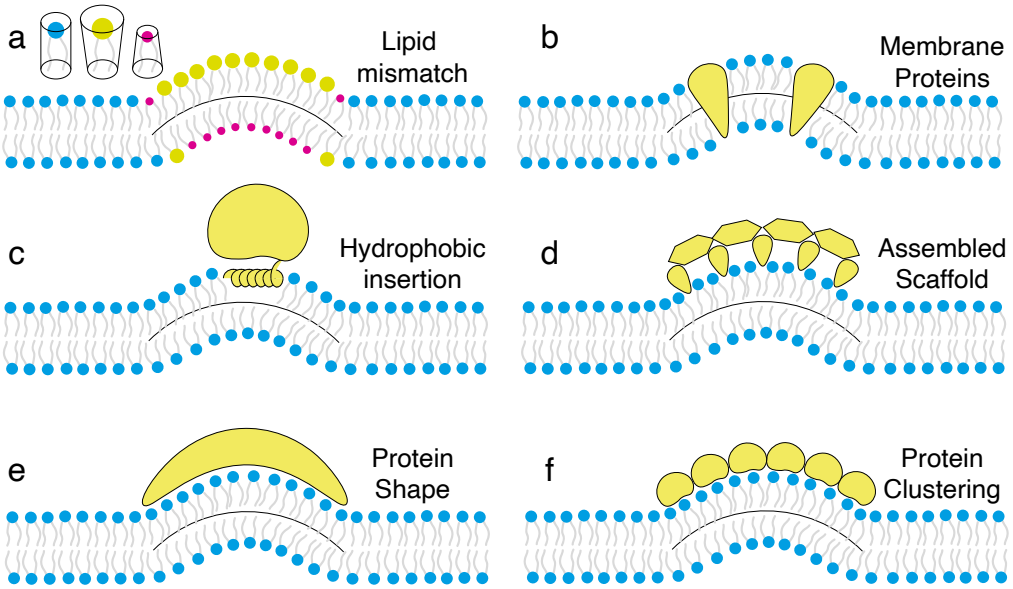

Figure 1.12: Schematic of different mechanisms of membrane curvature generation in cells including (a) lipid mismatch, (b) transmembrane protein shape, (c) insertion of hydrophobic protein motifs, (d) assembly of protein scaffold, (e) protein shape scaffolding and (f) clustering of proteins. Redrawn with modifications from Jarsch *et al.* [80]

ter and drive curvature (Figures 1.12c). These two methods come about in endocytosis. [89] This is by no means a full summary of all the possible curvature-driving mechanisms but it provides a good overview of the main mechanisms present. Other mechanisms include the cell's actin cytoskeleton generating membrane curvature by imposing forces on the cell membrane directly. [90, 91] This happens during cell migration and attachment to the ECM. [92] Disordered proteins can also cluster and create membrane curvature through steric crowding as in Figure 1.12f. [93, 94]

During a given cellular process, each of the mechanisms listed in Figure 1.12 might be active at the same time, giving rise to a dynamic and adaptable system of curvature generation. [80] One such process, endocytosis, is of particular interest to the scope of this thesis.

1.3.2 Endocytosis

In the body, molecules and species traverse the cell's natural barrier via an active process known as endocytosis. Indeed, endocytosis is a cell-driven process which, coupled with exocytosis allows cells to manage their intracellular nutrient balance. [91] Endocytotic pathways describe the methods by which a cell introduces molecules and substances into

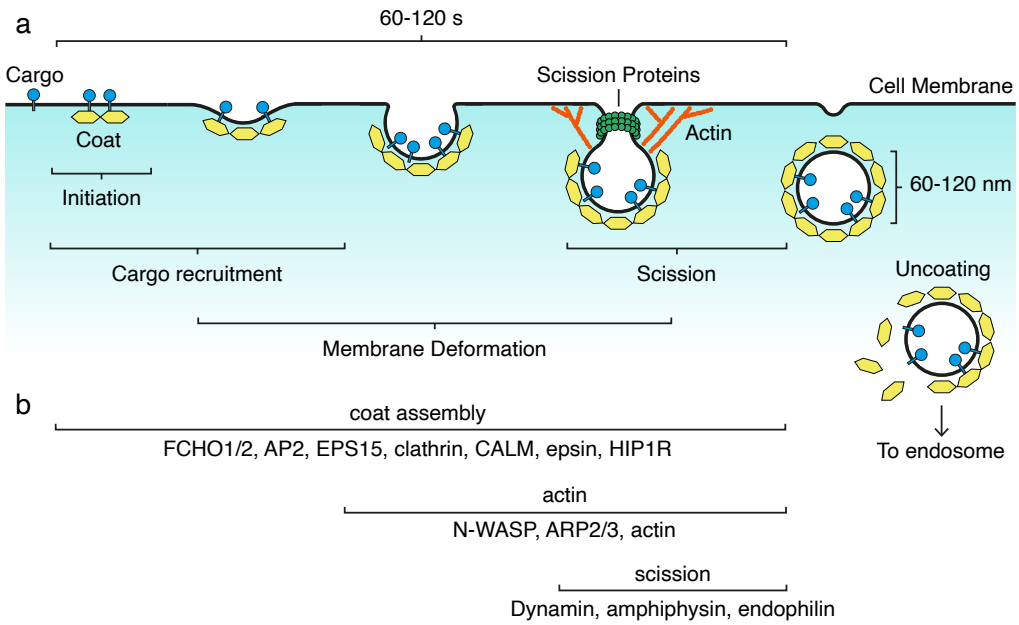

Figure 1.13: Schematic of clathrin-mediated endocytosis showing (a) the formation and stabilization of the endocytic bud as well as (b) key proteins involved in the process. Redrawn with modifications from Kaksonen *et al.* [89]

its cytosol (while exocytosis describes the removal of species from the cytosol). This process can occur under multiple circumstances and modes, the most common of which are phagocytosis, macropinocytosis or caveolae and clathrin-mediated endocytosis. [95] The common feature of these processes, bar phagocytosis and pinocytosis, is the presence and nucleation of an endocytotic vesicle which encapsulates external cargo and transports it into the cell. Each of these processes is slightly different and can be activated by various parameters related to the nature of the cargo as well as how the transport vesicle is formed. This endocytic vesicle buds off from the cell's plasma membrane, which can spontaneously repair itself, and transports the extracellular cargo into the cell by fusing with trafficking vesicles known as endosomes. These endosomes allow the cargo to be sorted before reaching a final vesicular organelle known as the lysosome. The lysosome acts essentially as a garbage collection for endosomal sorting. If the cargo is unnecessary to the cell, it will end up in the lysosome where it is degraded by enzymes in an acidic environment. Being able to escape this vesicle (known as endosomal escape) before degradation in the lysosome is a key challenge in the design of nanotechnological drug delivery devices. This is due to the fact that, when nanoparticles are introduced to a cell, they will predominantly be ingested by the cell via endocytosis. [96]

Clathrin-mediated endocytosis is of particular interest due to impressive clathrin coat pro-

tein which forms over the initial budding vesicle. This hexagonal protein assembles dynamically around the growing bud to stabilize its curvature and then uncoats the vesicle after release into cytosol. Figure 1.13a shows a schematic of entry into a cell via clathrin-mediated endocytosis showing the assembly and then disassembly of the clathrin-coat on the endocytic vesicle. A number of proteins critical to this process have been identified over the years. These include proteins which contain hydrophobic moities to drive curvature (Epsin, clathrin assembly lymphoid myeloid leukaemia protein (CALM)), curvature stabilising proteins (F-BAR domain only protein 1 and 2 complex (FCHO1/2), amphiphysin, endophiliin) and proteins which connect the clathrin coat to the membrane (adaptor protein 2 (AP2), Actin Related Protein 2/3 (ARP2/3)). [89] All these proteins will act in concert to drive membrane curvature, stabilize the formation of the clathrin coat and bridge the clathrin coat to the actin machinery. Dynamin is an outlier as its role is to cleave the budding vesicle from the plasma membrane in order to release into the cytosol. [97, 98] In addition to identifying the main proteins at play, recent developments in super-resolution and transmission electron microscopy techniques have even allowed for the spatial and temporal study of how these proteins localize around the endocytic pit as endocytosis progresses. [99–101]

Many of these proteins contain curvature-active domains which act following the same mechanisms discussed previously and shown in Figure 1.12. FCHO1/2, for example, contains a F-BAR domain, while Epsin and CALM contain a ENTH and ANTH domain respectively. The Bin/Amphiphysin/Rvs (BAR) domain family have been extensively studied for their ability to generate and stabilize curvature due to their unique "banana shape" both experimentally, [102–105] and computationally. [53, 106, 107] These BAR domains follow a curvature mechanism similar to that shown in 1.12e. The Epsin N-Terminal Homology (ENTH) and AP180 N-Terminal Homology (ANTH) domains, on the other hand, drive curvature by insertion of hydrophobic residues into the membrane such as in Figure 1.12c. [108, 109] Figure 1.13b gives an overview of some the key proteins acting during endocytosis. The BAR domain and amphipathic helix-containing domains, each with their own curvature generation mechanism, have become the two most studied structural mechanisms by which protein-driven membrane curvature is generated and sensed. [77]

In addition to the proteins of interest, phosphoinositide (PIP) lipids have been identified as key players during endocytosis. [110] These lipids, named after their inositol ring headgroup (see Figure 1.14), can be phosphorylated at three different sites for a total of seven different states, each enabling a different cellular function. Phosphatidylinositol-4,5-bisphosphate (PI(4,5)P2) is required to nucleate endocytic pits while PI(3)P plays a significant role in the later stages of endocytosis. [89, 111] The transition from the former

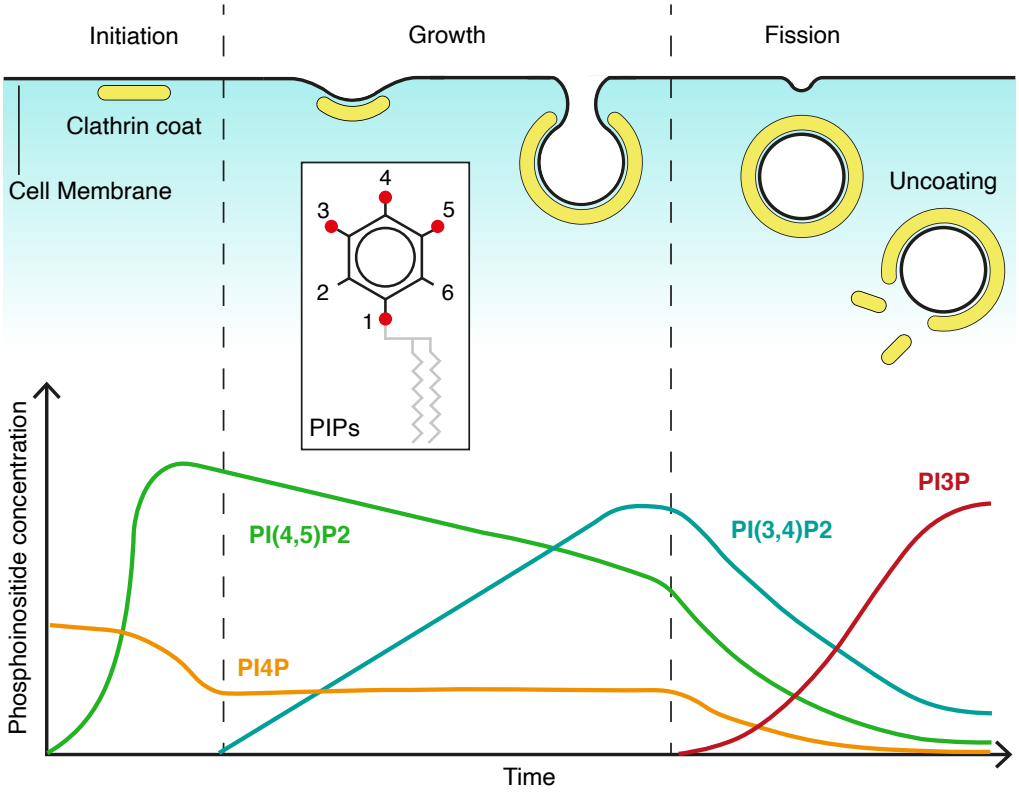

Figure 1.14: Schematic of the relevant phosphoinsositide (PIP) lipids active during endocytosis as well as a schematic a PIP lipid highlighting its inositol ring. Redrawn with modifications from Kaksonen *et al.* [89]

phosphorylation state to the latter is mediated by the formation of PI(3,4)P2, required for endocytic pits to mature. [112] Figure 1.14 shows a schematic of PIP lipids active during endocytosis. Furthermore, many of the proteins and protein domains involved in endocytosis bind PIP lipids. For example, AP2, epsin, CALM and dynamin each have a PI(4,5)P2 binding domain. PI(4,5)P2 is most likely the most important phosphoinositide involved in endocytosis as it is required for binding of many proteins as well as being enriched at the initiation steps of the process. [113] For the rest of this thesis, PI(4,5)P2 will be abbreviated as PIP2 for simplicity.

There is a lack of literature surrounding the exact roles of these lipids within the context of membrane curvature. Computational studies suggest that PIP2 prefers regions of concave curvature [84, 114] while experimentally these lipids are enriched at endocytic sites where curvature is convex. Furthermore, there is a causality dilemma regarding PIP2 and their binding partners during endocytosis. Do PIP2 lipids cluster around budding vesicles when endocytosis starts? Or is PIP2 enriched due to the clustering of curvature proteins? While

answering these questions is beyond the scope of this thesis, the research presented in the following chapters aims to explore the complex interactions between membrane curvature, binding lipids and curvature-active proteins using computational methods.

1.3.3 Modelling Cell Membrane Curvature

The physics for understanding membrane curvature can be traced back to the development of Canham-Helfrich's bending energy model. [115] This theoretical framework led to some of the earliest models of membrane deformation in the early 1990s, [116–118] up to today. [119–122] Similar models have focussed more closely on endocytosis by exploring the energetics of vesicular bud formation, how these are stabilised by curvature proteins, [123–126] as well as how actin self-assembles on endocytic pits. [127] These theoretical methods have also been applied to study the shape and orientation of nanoparticles for improved endocytosis. [128] One of the main drawbacks of these approaches is the lack of molecular information on the membrane. Indeed, membranes are represented as smooth, continuous sheets and remove the complexities of the membrane as an assembly of lipid molecules. These models are excellent for studying the physics and properties of membranes but do not allow for the study of individual lipids or proteins within membranes.

In order to account for this, researchers have explored membrane curvature through the assembly and dynamics of particles. Although atomistic simulations have been extensively used to study lipid membranes since the early 1980s and 1990s, [40, 129, 130] the time and length scale of these simulations have meant that studying membrane curvature is not feasible. As we have seen previously, cellular membrane curvature is on the order of tens of nanometers, a scale that is difficult to reach using fully atomistic molecular simulations. As such researchers studying membrane curvature have relied on coarse-grained (CG) models which approximate lipid molecules as a series of beads. [131] This development has allowed for the study of membrane curvature in mixed composition membranes and vesicles, [132–136] as well as curvature induced by nanoparticles. [137–140] A number of studies have also focussed on how nanoparticles are endocytosed and how their properties affects their ability to cross the membrane. [141–147]

In addition, a large branch of computational research has focussed on directly studying curvature proteins interacting with membranes. Reynwar *et al*'s work is often one of the most famous images of computational modelling applied to biomembranes deformed by pseudo-proteins. [73] Figure 1.15a is reproduced from this work showing striking membrane curvature generation by clustering of surface-bound proteins. Fitting to their importance in the field of membrane curvature, much focus has also gone into to studying the membrane tubulation and curvature generation by BAR domains (see Figures 1.15b

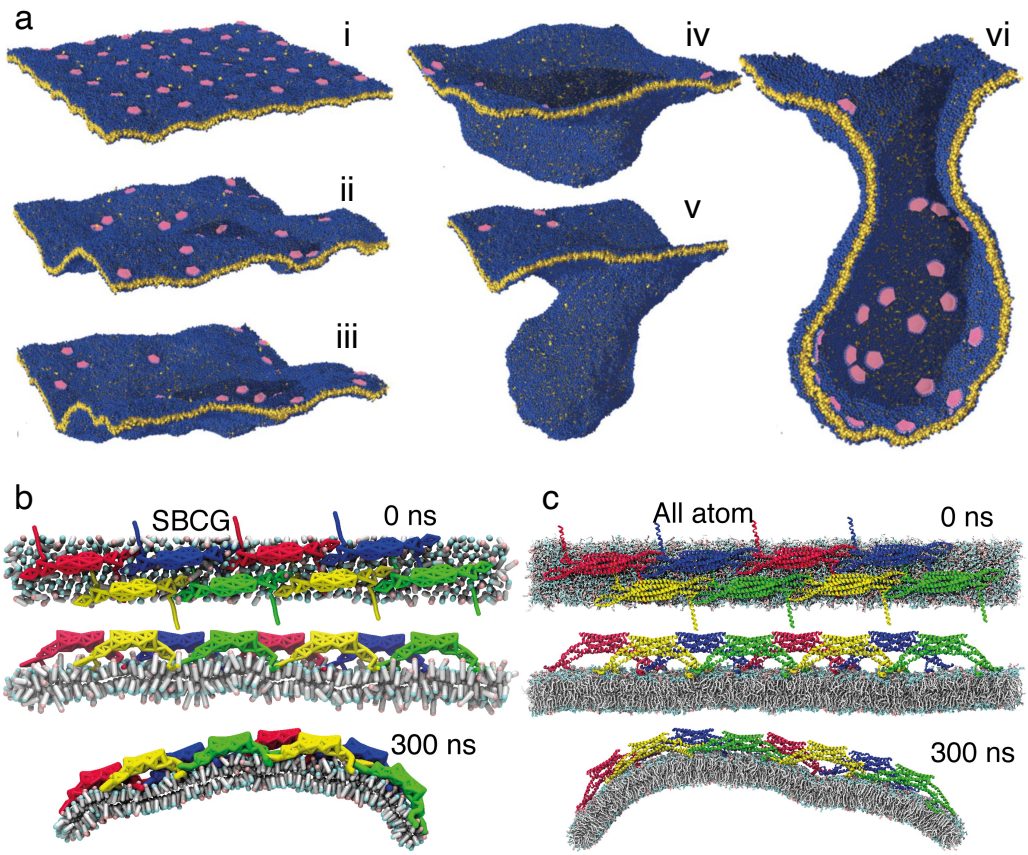

Figure 1.15: (a) Simulation snapshots of a coarse-grained simulation showing significant curvature generation over time (i-vi) by curvature-active pseudo-proteins. Adapted with permission from Reynwar *et al*. [73] Copyright 2007, Springer Nature. Snapshots of membrane curvature driven by BAR domains of Amphiphysin in (b) shape-based coarse-grained (SBCG) and (c) atomistic simulations. Adapted with permission from Yin *et al*. [106] Copyright 2009, Elsevier.

and 1.15c). [106, 148–155] The ENTH domain has also been studied computationally to understand helix insertion and curvature generation, [114, 156–159] while membrane proteins and their curvature inducing properties have also been simulated. [160–162]

1.3.4 Nanomaterials That Influence the Cell Membrane

Having introduced the importance of the cell membrane and its curvature, many researchers have employed the use of nanotechnology to directly manipulate membrane curvature and endocytosis. One of the main applications of nanomaterials in this area has been the development of high-aspect nanostructures to disrupt the cell membrane in order to deliver cargo to cells. [163–167] The idea of using sharp nanostructures to deliver drugs directly to regions of the body is not a new one and has been present in the literature since the mid

to late 1990s [168, 169] up until today [170, 171]. Sharp nanostructures were thought to be able to "pierce" cells allowing for direct delivery of cargo to the cytosol sidestepping endocytosis and lysosomal destruction. Although direct piercing of the cell membrane by nanostructures is unlikely under gravitational forces, [172], nevertheless, there remains an interest in using these structures for drug delivery. Recent research by the Melosh group has shown direct interfluidic access to cells using nanostraw devices, [164, 173–176] while researchers in the Stevens group have shown successful in vitro and in vivo drug delivery using porous silicon nanoneedles. [23, 24]

In addition to drug delivery applications, high-aspect nanostructures have been used to collect intracellular measurements such as enzymatic activity, intracellular pH and electrical current. [177–180] Measuring electrical signal of cells with nanostructures is particularly relevant to the study of neurons [15, 17, 181, 182] as well as cardiomyocytes [20, 183, 184] due to their production of electric signals.

The novelty of these results has led a number of researchers to investigate the interface between sharp nanostructures and cells. This has included using high-resolution TEM techniques, [185] membrane-specific labelling, [186] and the use of transparent nanowire arrays, [187] among others, to accurately examine this interface. [188, 189] Understanding how the cell membrane is affected by interfacing with sharp nanostructures is key to improving such nanomaterials for future applications.

As such, researchers have begun to study how cellular processes are modified at the cell-nanostructure interface. Porous silicon nanoneedles, for example, were recently shown to locally stimulate endocytosis at their surfaces by Gopal *et al* (see Figures 1.16a, 1.16b and 1.16c). [190] These vesicles were concentrated mainly around the tips and sides of the nanoneedles suggesting that the tight interface with a nanoporous material was key to stimulating endocytosis, potentially by driving nanoscale membrane curvature. These same materials were also shown to directly manipulate mechanotransduction pathways within cells by deforming the cell and nuclear envelope. [191] Furthermore, Galic *et al* and Zhao *et al* have observed the clustering of curvature-sensitive proteins around nanostructure-induced cell deformations (see Figure 1.16b), [192, 193] suggesting that membrane curvature and membrane-protein interactions can be directly influenced with nanotextured substrates. Lou *et al* has also shown that actin polymerisation can be induced by nanoscale surface topography, [194] while curvature external to the cell, in the form of smooth topographical features, has been shown to affect cell motility, gene expression and focal adhesion organization. [195]

Finally, as the experimental interest in this biointerface has grown, a number of studies

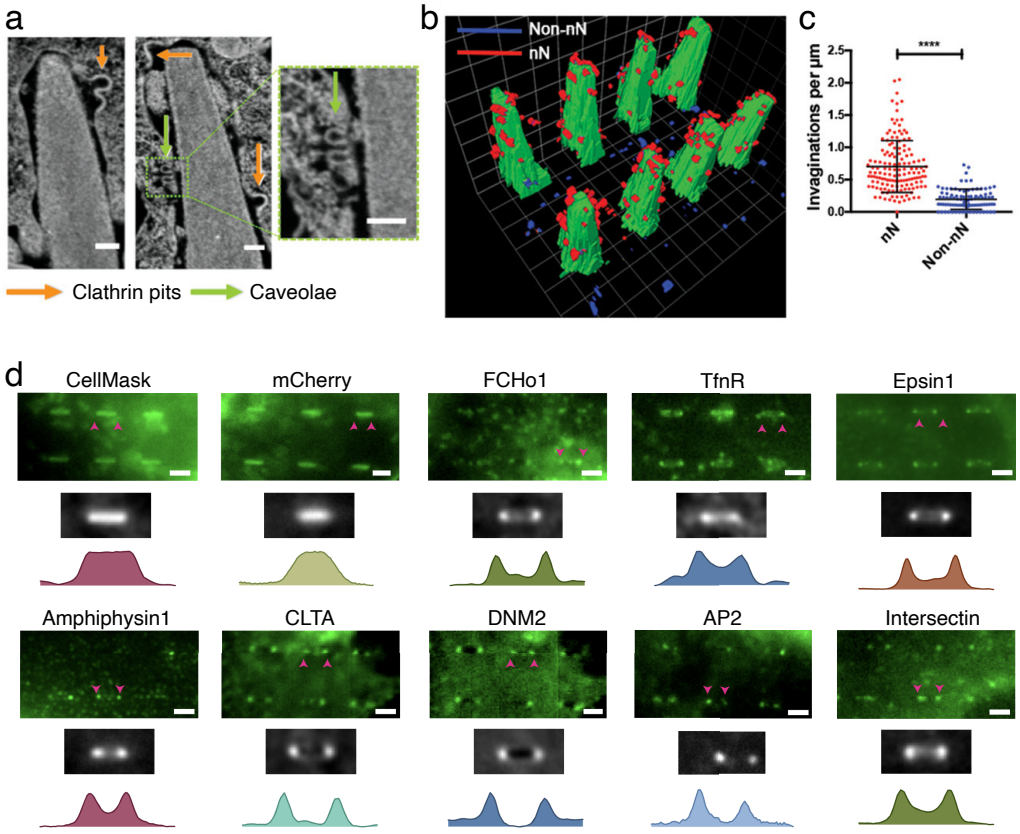

Figure 1.16: (a) Electron micrographs of porous nanoneedles interfaced with cells, (b) confocal reconstructions of endocytic pits surrounding nanoneedles and compared to flat silicon and (c) number of endocytic pits compared on nanoneedles (nN) and flat silion (non-nN). Adapted with permission under a Creative Commons License from Gopal *et al.* [190] Copyright 2019, Wiley. Fluorescence imaging of proteins localized to regions of membrane curvature induced by interfacing with nanopillars. The averaged images of hundreds of nanobars and the intensity along the length of nanobars are shown below the fluorescent images. Adapted with permission from Zhao *et al.* [196] Copyright 2017, Springer Nature.

have attempted to simulate the cell-nanostructure interface. These computational models vary in their approach to the cell membrane, but most consider it as a continuous sheet characterized by parameters such as tension or stiffness. This method considers the balance of forces at the cell-nanomaterial interface in order to provide a free-energy map of likely outcomes. For example, by assuming the gravitational force acting upon the cell, the hydrostatic pressure inside and the net membrane tension, one can estimate the likelyhood of a given nanowire geometry to penetrate a cell. [197, 198] The free energy of the cell–substrate interaction can also be expressed as the sum of the cell–substrate adhesion, the change in surface tension caused by an increase in cell surface area, and the change

in elastic energy caused by bending the membrane in order to understand how a cell will deform on a nanostructured surface. [199–201] These calculations are often computationally inexpensive and highly modular allowing for the exploration of multiple variables with relative ease at the expense of gaining molecular insight into the interface. [202] However, these molecular insights are highly important for understanding the biological effects of nanostructures on cells. Indeed, changes in membrane properties at curvature and clustering of proteins at curvature are lost at this scale.

The work presented in this thesis aims to fill in some of the gaps in our knowledge of the interface between nanomaterials and cell membranes. In particular, this employs coarse-grained molecular dynamics simulations to study how membrane curvature can be induced by nanoporous substrates and what biological effects this curvature may have in Chapter 2. The thesis subsequently explores the binding and localization of two key proteins involved in endocytosis to curvature in Chapters 3 and 4. Chapter 5 examines the application of XPS to the study of nanomaterial surface chemistry for applications in biology.

Chapter 2

Membrane Curvature Driven by Nanoporosity

This chapter describes the use of coarse-grained molecular dynamics simulations to study the interaction between model lipid membranes and nanostructured material surfaces. In particular, the results explore how membrane curvature can be induced through interfacing with nanoporous wafers and how this curvature can act as a hotspot for bioactivity. This chapter is adapted with permission from work published in Belessiotis-Richards *et al*. [159]

2.1 Introduction

The Introduction presented some examples of nanomaterials used for influencing and manipulating cell membranes. One of the main issues in this field is the lack of information on the interface between the cell membrane and these materials. As such, this chapter aims to investigate this interface using a model system; a lipid membrane interacting with a nanoporous substrate.

Nanoporous materials have been studied in detail over the past few years in particular for promoting cell adhesion, proliferation and differentiation on surfaces, [203–211] while membrane curvature has been studied previously in silico using a mixture of coarse-grained and atomistic approaches. [212, 213] However, most computational models focus on protein-sensing or protein-induced deformation, and neglect the influence of nanostructured surfaces. Of the few porosity-induced models, these have considered the impact of 10 to 100 nm structures, rather than sub-10 nm nanopores, while still showing that membrane adhesion to nanopores is favourable. [214] This chapter attempts to extend our

understanding of this bio-nano interface by showing how even below 10 nm, nanoporous surfaces directly induce membrane curvature, and can subsequently influence protein localization.

Employing coarse-grained molecular dynamics simulations, membranes were simulated interacting with nanoporous wafers. These nanotextured surfaces are inspired by the surface topography of porous silicon nanoneedles co-developed in the Stevens Groups. [23, 24, 180, 190] These simulations predict membrane deformation behaviour on nanoscale features much smaller than previously reported in the literature. Pores as small as 8 nm in diameter can deform lipid bilayers. The extent to which the membrane is deformed by nanopores can be strongly controlled and a series of design parameters for fabricating cell-active surfaces can be defined. One of these design parameters describes pore taper; the sharpness of the pore edge. Tapering is a previously unexamined characteristic of nanostructures for cellular interfacing applications, applicable to the design of nanoporous materials as well as high aspect-ratio nanostructures.

The results presented in this chapter show that, when membranes are curved, the properties of the membrane change, resulting in increased area-per-lipid, decreased thickness and increased lipid mobility in the cytosolic-leaflet of curved membrane regions. Experimental studies have suggested that regions of membrane curvature have increased bioactivity, attracting curvature-sensitive proteins. [192, 193] This was confirmed by simulating a deformed membrane with a model curvature-active protein, the Epsin N-Terminal Homology (ENTH) domain. These simulations show spontaneous localization and specificity of the ENTH domain to curvature suggesting a potential role of nanopore-induced curvature in localizing endocytic processes. More work needs to be done on examining different membrane-active proteins and their potential interactions with curvature, but these ENTH-domain simulations substantiate the bioactivity of such regions.

In order to evaluate how membranes interact with nanoporous substrates, a simple model surface of a flat wafer with a single central pore was developed, shown schematically in Figure 2.1a. Model bilayers were then placed above the wafer and allowed to interact with the central nanopore. Spontaneous membrane curvature was observed in almost all cases after interfacing with these nanostructures. Three key nanopore construction parameters were defined to evaluate this effect: pore radius (R, nm), pore taper (T, nm) and surface attraction of the wafer surface (ϵ, kJ/mol) (shown schematically in Figure 2.1b). Each of these parameters was modified and their effect on membrane curvature evaluated. Nanopores were designed with pore radii of 4, 6, 8 and 10 nm, pore tapers of 0.75, 1.25, 2.5 and 5 nm and surface attraction of 0.5, 1.0, 1.5 and 2.0 kJ/mol, totaling 64 individual

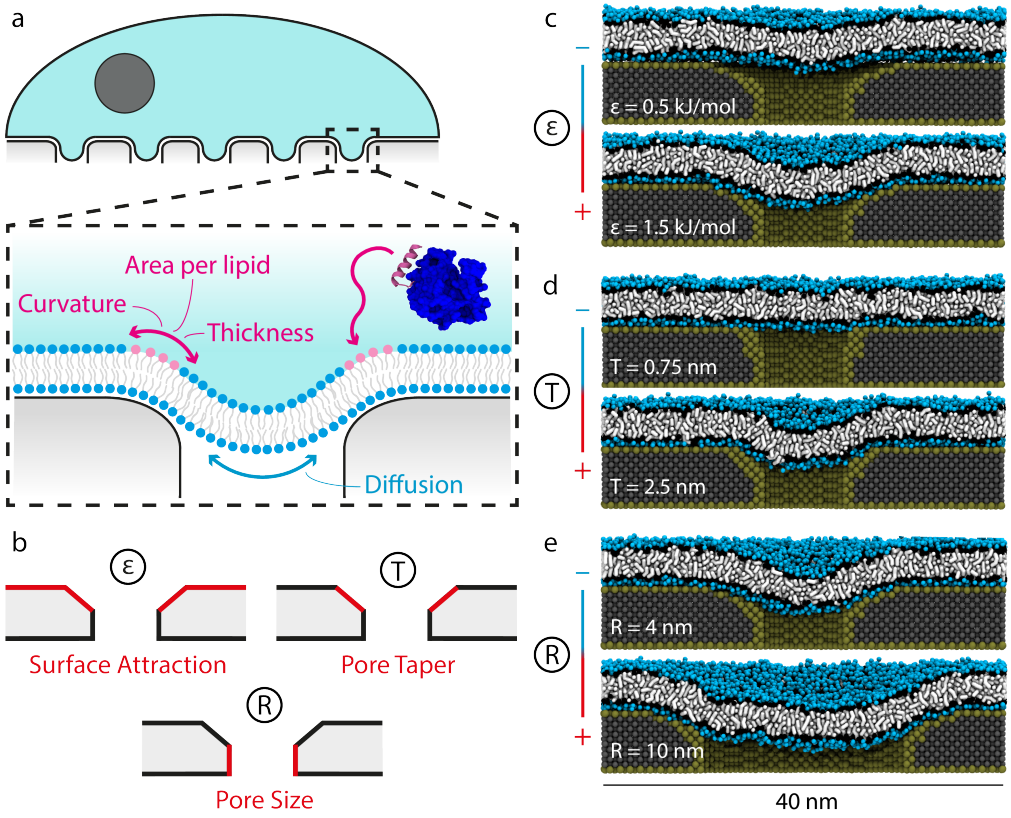

Figure 2.1: (a) Illustration of a cell in contact with a nanoporous substrate showing nanopore-induced membrane curvature and highlighting the approximate locations of curved membrane regions with modified membrane properties (pink lipid heads) exhibiting curvature, above average areas-per-lipid, reduced thickness as well as increased bioactivity. The membrane region not in contact with the wafer, as identified with blue arrow, exhibits increased lipid diffusion in both leaflets. (b) The wafer design parameters explored for influencing membrane deformation: pore radius (R, nm), pore taper (T, nm) and the surface attraction of the wafer surface (ϵ, kJ/mol). (c), (d), (e) Representative cross-sectional snapshots showing membranes after 300 ns of production molecular dynamics under different wafer construction conditions showing the effect of low (-) and high (+) values of each parameter from (b). Reproduced with permission from Belessiotis-Richards *et al*. [159] Copyright 2019, American Chemical Society.

nanopore designs. Details of the wafer construction can be found in section 2.2.

The simulation snapshots in Figure 2.1b show the spontaneous membrane curvature driven by nanoporosity. These snapshots are cross-sections of deformed membranes (after 300 ns of simulation) interacting with various wafer design conditions highlighting the extent to which nanoporous-surfaces curve membranes and the effect of each nanopore design parameter. Decreasing surface attraction reduces the extent of membrane entry into the pore (Figure 2.1c), while increasing pore radius has little impact on the overall curvature of the membrane (Figure 2.1e). Minor increases in the pore taper, on the other hand, have a strong influence, with the membrane changing from relatively flat to highly-curved, see in Figure 2.1d.

2.2 Methods

2.2.1 Simulations Details

All curvature simulations were performed at 310 K with Gromacs 4.6.7[215] using the Dry Martini implicit-solvent coarse-grained force field[57] and visualized using VMD (Visual Molecular Dynamics). [216] The MDAnalysis package was used for all the analysis in this work unless stated otherwise. [217] Membranes were generated from dipalmitoylphosphatidylcholine (DOPC) lipids and contained 4056 molecules using the insane.py script available from cgmartini.nl. [218] Porous wafers were built manually with beads arranged in a Face Centred Cubic structure (FCC) using the Atomic Simulation Environment (ASE) package. [219] Membranes were placed above the nanoporous wafers and were equilibrated for 20 ns using a 0.02 ps time step followed by two rounds of 300 ns of production MD using a 0.03 ps time step, the first round allowing for the membrane to come into contact with the wafer and the second for evaluating membrane properties. All implicit-solvent simulations were carried out without pressure coupling and using a velocity-rescaling thermostat with a 1 ps time constant.

Protein simulations were performed at 323 K using the Martini force-field with explicit water. [52] Explicit and implicit water models showed similar curvature behaviour as seen in Figure 2.13. A case from the curvature-control simulations (R = 6 nm, T = 5 nm and ϵ = 2.0 kJ/mol) was taken and hydrated with coarse-grained water and 10% anti-freeze particles. The higher temperature (323 K instead of a more standard 310 K) and anti-freeze particles are used in order to avoid the freezing of water molecules in the system due to their coarse-grained nature. This is a common issue with the martini model. [52]

The ENTH domain was placed 3 nm above the center of the membrane. The system was equilibrated for 20 ns using a 0.02 ps time step and then simulated for 4 μs using a 0.03 ps time step. During equilibration and production MD, a semi-isotropic Berendsen and Parinello-Rahman barostat was used, using a time constant of 1 and 12 ps respectively. The protein structure of the ENTH domain of Epsin-1 was taken from the RCSB protein data base from the structure resolved by Ford et al. (Protein Data Bank (PDB): 1H0A)[109] and converted into a coarse-grained system using the martinize.py script provided by the Martini developers. The surface of the nanoporous substrate was negatively charged in order to promote adhesion of the membrane, better representing strong attraction seen in reality, [220, 221] and overcoming the diminished adhesive effects in explicit water simulation. Counter ions balancing the charges are also included. Protein minimum distance to membrane and radius of gyration (shown in Figure 2.15b) were calculated using the

$g_mindist$ and g_gyrate tools respectively in Gromacs. [215] The $g_mindist$ tool was also used to compute the number of hydrophobic contacts between protein residues and lipid tails (Figure 2.14b).

2.2.2 Nanoporous Wafer Construction

The nanoporous wafers simulated in this study were designed by first building a rectangle of beads (40 nm x 40 nm x 6 nm) in a Face Centred Cubic structure (FCC) using the Atomic Simulation Environment (ASE) package. [219] A central cylinder of beads with chosen radius (R = 4, 6, 8 or 10 nm) was then removed from the block to form the central pore. We then tapered the edges of the pore in the top 3 nm of the block (leaving the bottom 3 nm cylindrical) using a square root law following:

$$r(z) = \frac{T}{c^2} + z^2 + R \tag{2.1}$$

Where r is the pore radius as a function of vertical distance (z), z is the vertical distance along which the tapering occurs, T is pore taper which describes the distance at which the pore taper ends (becoming the flat surface), R is the minimum radius of the pore and c is the thickness of the tapered region (fixed at 3 nm). The value of T was modified between 0.75, 1.25, 2.5 and 5 nm.

The surface attraction of the wafer was controlled by defining a new coarse-grained bead type for the surface of the wafer. The attraction between lipid heads (Q0 beads) and the crystal surface was then controlled by varying the ϵ parameter within the Lennard-Jones potential of the Dry Martini force-field. [57] The value of ϵ was varied between 0.5, 1.0, 1.5 and 2.0 kJ/mol. In total 64 wafer designs were evaluated.

2.2.3 Curvature Evaluation

Following two rounds of production MD, the lipid heads in the membrane upper-leaflet were averaged and fitted to the sigmoid function shown in equation 2.2 (Figures 2.3a and 2.4 as represented schematically in Figure 2.2. The curvature of the membrane is then evaluated using equation 2.3 (Figures 2.3b and 2.5). The maximum curvature values (Figure 2.6) of the membranes were then computed by solving the roots of the third derivative of equation 2.2 for each simulation case.

To quantify membrane curvature, we fit the curvature profiles to a sigmoid-like equation following (Figure 2.2):

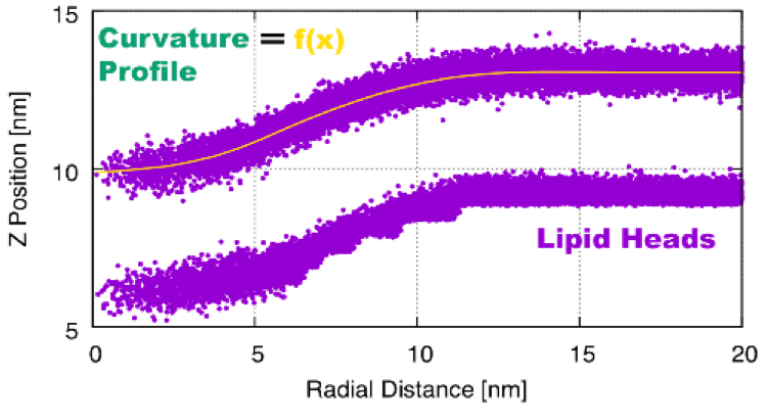

Figure 2.2: Plot of lipid head z-position as a function of radial distance, for both membrane leaflets. The yellow line indicates the fit of a sigmoid-like function to the upper membrane lipid head positions. The Figure is an example of how the curvature was evaluated for nanopore-induced membrane deformation under variable wafer conditions. Reproduced with permission from Belessiotis-Richards *et al.* [159] Copyright 2019, American Chemical Society.

$$f(x) = \frac{a}{d + e^{-c(x-x0)}} + b \tag{2.2}$$

Where a, b, c, d and x0 are fitting parameters. Once fitted, we can input the first and second derivatives of this function in order to calculate the radius of curvature along the curvature profile using:

$$K(x) = \frac{1}{R_c(x)} = \frac{f"(x)}{(1 + (f'(x)^2)^{3/2}} \tag{2.3}$$

Where K is the absolute curvature of the function, Rc is the radius of curvature and f'(x) and f"(x) are the first and second derivatives of the sigmoid function fit of the membrane profile given respectively by:

$$f'(x) = \frac{ace^{-c(x-x0)}}{\left(d + e^{-c(x-x0)}\right)^2} \tag{2.4}$$

$$f''(x) = \frac{ac^2e^{-c(x-x0)}\left(e^{-c(x-x0)} - d\right)}{\left(d + e^{-c(x-x0)}\right)^3} \tag{2.5}$$

The maximum curvature values of the membrane (Figure 2.6 in main text) are determined by taking the third derivative of the sigmoid curve, $f'''(x)$:

$$f'''(x) = \frac{ac^3 e^{-c(x-x0)} \left(e^{-2c(x-x0)} - 4de^{-c(x-x0)} + d^2\right)}{\left(d + e^{-c(x-x0)}\right)^4} \tag{2.6}$$

And solving for its roots following:

$$e^{-2c(x-x0)} - 4de^{-c(x-x0)} + d^2 = 0 \tag{2.7}$$

Assuming:

$$u(x) = e^{-c(x-x0)} \tag{2.8}$$

We can re-write the equation and solve for a quadratic function:

$$u^2 - 4u + d^2 = 0 \tag{2.9}$$

The solutions to this equation being: $e^{-c(x-x0)} = 2d - \frac{\sqrt{12}}{2}d$ and $e^{-c(x-x0)} = 2d + \frac{\sqrt{12}}{2}d$

We can identify the roots and find the max curvature values of the membrane using:

$$x_{1,2} = \frac{-\ln\left(2d - \sqrt{12}d\right)}{c} + x0 \tag{2.10}$$

2.2.4 Membrane Analysis

All membrane property heatmaps (Figure 2.8 and 2.9, 2.10, 2.11 and 2.12) were evaluated over the last 90 ns of simulation time to avoid erroneous results as the membrane contacts the wafer, as well as incorrect property measurements due to lateral membrane motion. Each heatmap was generated by segmenting membrane simulations into 30 by 30 equally spaced bins in the x-y plane.

Area per lipid

Membrane area per lipid in each bin (Figure 2.8b and 2.10) was calculated measuring the average minimum distance (d) between lipid headgroups (PO4 beads in Martini DOPC). This minimum distance is then converted to estimate the area per lipid by assuming that each lipid has a circular area accessible to it of radius, $\frac{d}{2}$, following:

$$\text{area per lipid} = \pi \left(\frac{d}{2}\right)^2 \tag{2.11}$$

Membrane Thickness and Lipid Orientation

Membrane thickness and lipid orientation (Figure 2.8a, 2.8c, 2.9 and 2.11) were estimated by fitting a plane to the top membrane leaflet in each segmented membrane bin. Note that this analysis requires each bin to contain a minimum of 3 lipids. By calculating two vectors (U1 and U2) between three points (a, b, c) on the plane, we can calculate the normal vector (N) of the plane using a cross-product following:

$$U_1 = \begin{pmatrix} a_x - b_x \\ a_y - b_y \\ a_z - b_z \end{pmatrix} \tag{2.12}$$

$$U_2 = \begin{pmatrix} a_x - c_x \\ a_y - c_y \\ a_z - c_z \end{pmatrix} \tag{2.13}$$

$$N = U_1 \times U_2 \tag{2.14}$$

Assuming the bottom leaflet is parallel to the top leaflet, we then calculate the vector (L) between a point in the top leaflet (a) and a point in the bottom leaflet (d) along the normal vector. We then normalize over the length of the normal vector to get an estimate for membrane thickness following:

$$L = \begin{pmatrix} a_x - d_x \\ a_y - d_y \\ a_z - d_z \end{pmatrix} \tag{2.15}$$

$$\text{thickness} = \frac{N \cdot L}{|N|} \tag{2.16}$$

By extracting the z-component of the normalized normal vector (|N|), we can estimate the orientation of membrane regions (i.e. if N_z = 1, the membrane is oriented perfectly parallel to the x-y plane).

Lipid Movement

Lipid movement (Figure 2.8d and 2.12) was measured by calculating the average movement of individual lipids between 300 ps frames of output simulation over given sections

of the membrane. Due to finite size effects, as well as the difficulty of mapping the mean-squared distance travelled by individual lipids to local sections of the membrane, we do not report here the values of diffusion coefficient. However, the overall diffusion coefficient of the membranes, calculated using g_msd, is consistent with reported values between 4 and 5×10^{-7} cm^2s^{-1}. [57]

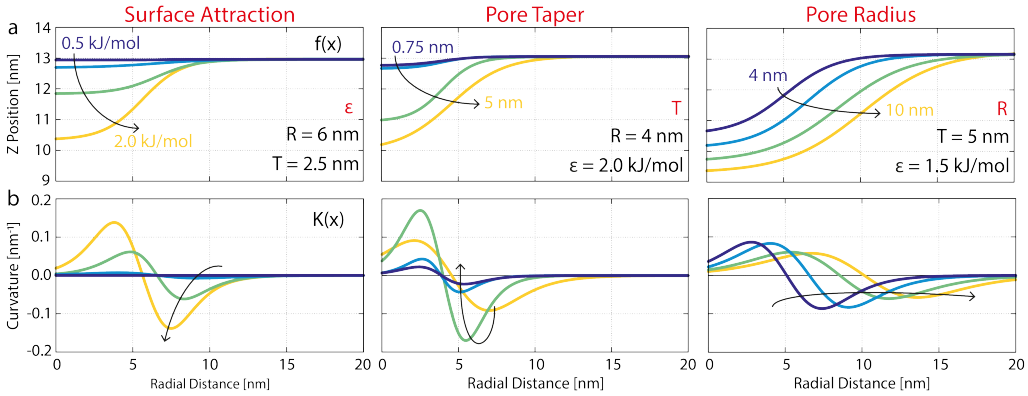

Figure 2.3: (a) Curvature profile and (b) curvature values as a function of radial distance for representative membranes under different nanopore conditions. The effect of pore taper can be clearly seen in the middle column of (b) showing a maximum curvature value at T = 2.5 nm. f(x) and K(x) refer to the functions in equations 1 and 2 respectively. Reproduced with permission from Belessiotis-Richards *et al.* [159] Copyright 2019, American Chemical Society.

2.3 Results & Discussion

2.3.1 Curvature Control of Model Cell Membrane

To quantify the extent of membrane curvature induction, we extracted the positions of lipid heads in the membrane's upper leaflet and averaged their positions radially from the central pore. This creates a 'curvature profile' of the deformed membrane which is then fitted to a sigmoid-like function (as seen in Figure 2.2) following equations 2.2 and 2.3.

Plots of the membrane profile, f(x), and curvature of the membrane, K(x), as a function of radial distance from the central pore are shown under various conditions in Figures 2.3a and 2.3b respectively. Figure 2.3 presents a summary of the fitted curves from different simulation snapshots, as per the example shown in Figure 2.2, and shows how nanoporosity can drive membrane curvature up to radii of approximately 5 nm. Each wafer construction parameter affects the final curvature of the membrane. Increasing the wafer pore size (R) from 4 to 10 nm reduces membrane curvature and shifts the position of maximum curvature away from the central pore. Unsurprisingly, increasing the attraction between lipids and the wafer stimulates membrane deformation. Interestingly, an optimal pore taper (T = 2.5 nm) value maximises curvature. Below or above this taper value, membrane curvature is less significant. Figures 2.4 and 2.5 show the curvature profiles and curvature values for all the parameters investigated in this chapter.

Solving the roots of the third derivative of the sigmoid fit f(x), the maximum curvature

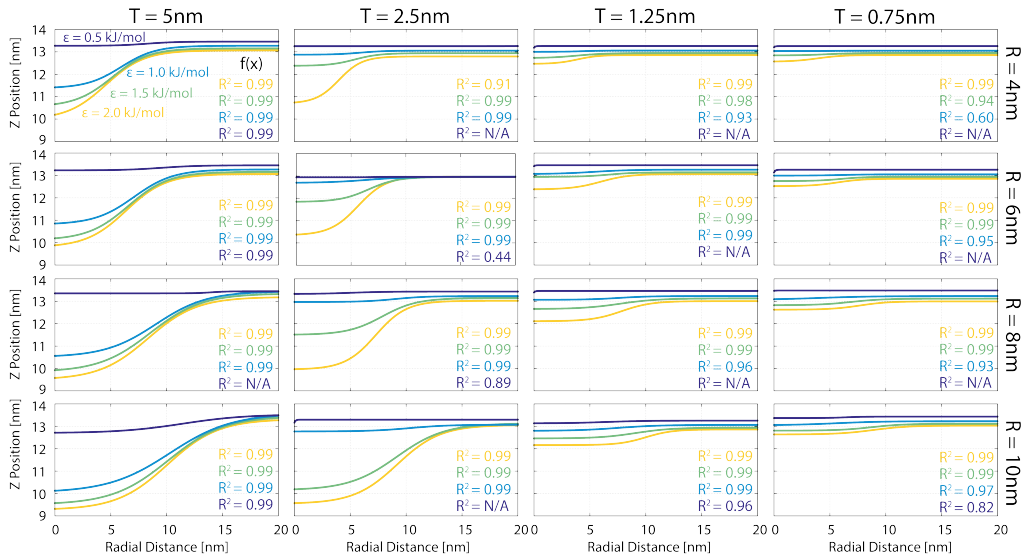

Figure 2.4: Curvature profiles of all wafer parameters (pore taper, T; pore radius, R; and surface attraction, ϵ) simulated in this study showing R squared values for the sigmoid fit of curvature to the simulation results. Reproduced with permission from Belessiotis-Richards *et al.* [159] Copyright 2019, American Chemical Society.

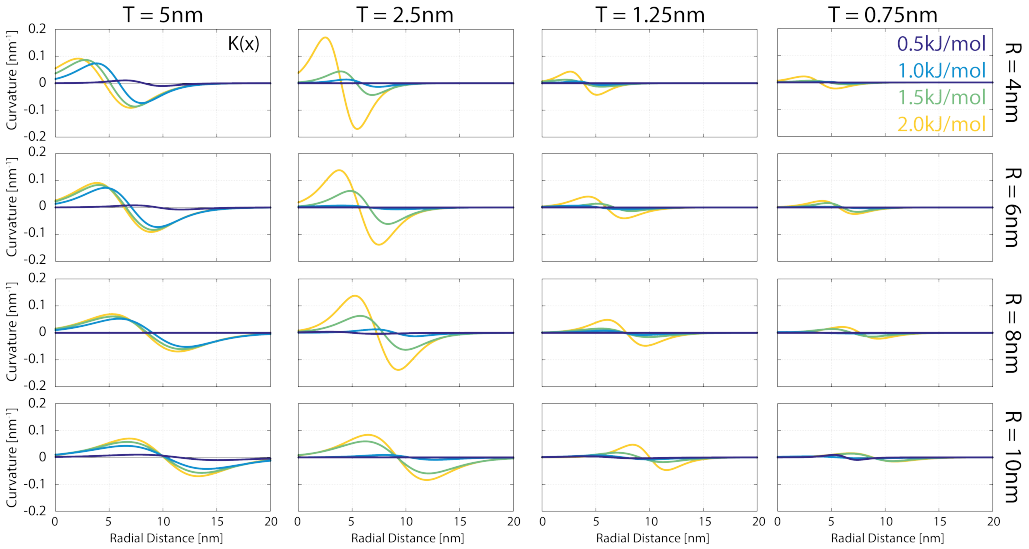

Figure 2.5: Curvature values of all wafer parameters (pore taper, T; pore radius, R; and surface attraction, ϵ) simulated in this study extracted from the sigmoid fits shown in Figure 2.4. Reproduced with permission from Belessiotis-Richards *et al.* [159] Copyright 2019, American Chemical Society.

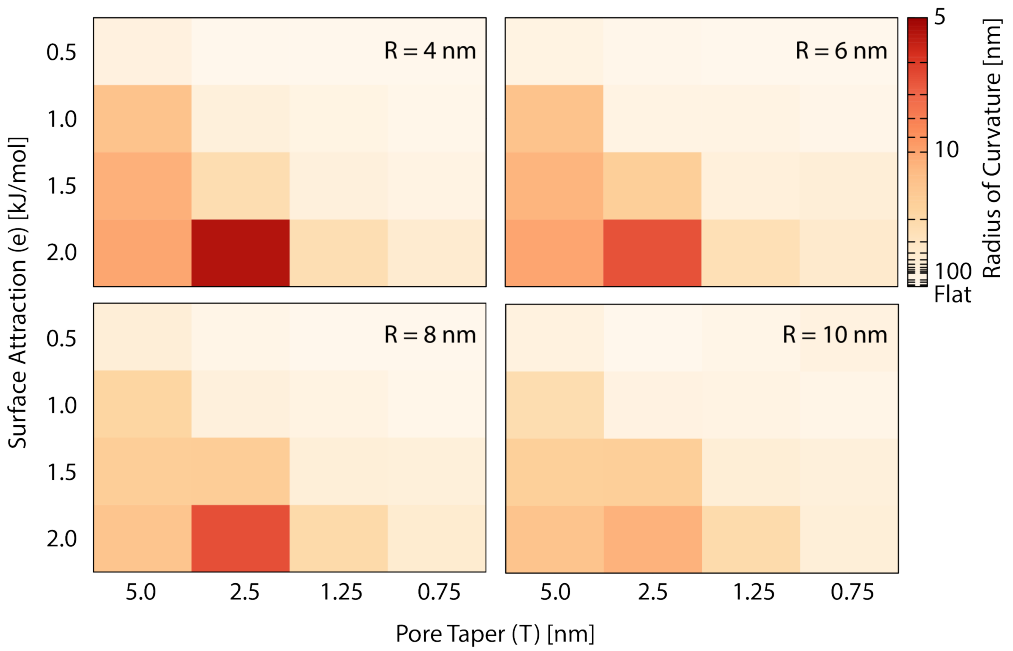

Figure 2.6: Parameter matrix showing the effects of pore size (R), pore taper (T) and surface attraction (ϵ) on final bilayer curvature, summarizing the results of all 64 combinations of the parameters simulated in this study. Each individual 4x4 square represents the varying pore taper and surface attraction values for a given pore size. Reproduced with permission from Belessiotis-Richards *et al*. [159] Copyright 2019, American Chemical Society.

values of the membrane can be evaluated quantitatively as a function of wafer design parameter. These maximum curvature values can then be plotted for each of the 64 wafer parameters investigated in order to determine which wafer designs maximize curvature generation. This is shown in Figure 2.6. From this Figure we observe that maximum curvature for each pore radius is at a taper of 2.5 nm. This suggests that the pore edge sharpness plays a crucial role in inducing membrane curvature. Conversely, membrane curvature decreases with increasing wafer pore size, suggesting a reducing effect of pore size on membrane curvature. This exact value of the optimal pore taper should be taken with a pinch of salt and would need to be validated using different modelling approaches.

These design parameters, in particular surface attraction and pore taper, can be used to guide the fabrication of nanostructures for biointerfacing applications. Increasing surface attraction of topographical surfaces can be achieved via chemical functionalization with peptide-binding motifs or other biomolecules that mimic the extracellular matrix environment. [222] Modifying the taper of nanostructures is an interesting, under-explored parameter that can be controlled using microfabrication techniques. Tapering is a general feature that can be applied not only to the design of planar nanoporous substrates, but also

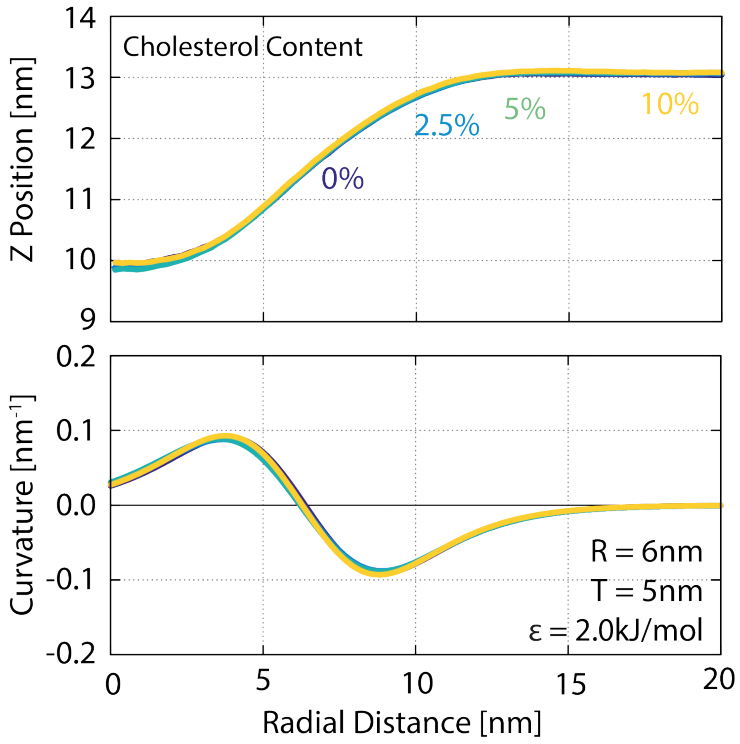

Figure 2.7: Curvature (a) profiles and (b) values of a DOPC membrane containing increasing amounts of cholesterol showing very little difference between final curvature. Reproduced with permission from Belessiotis-Richards *et al.* [159] Copyright 2019, American Chemical Society.

to high aspect-ratio nanostructures such as nanoneedles. [23] We suggest this approach could be employed to enhance the cell membrane curvature generation of nanopillar or nanowire substrates. Tapering could be introduced relatively easily using microfabrication techniques such as metal-assisted chemical etching, [223] or reactive ion-etching. [224]

The model lipid membranes studied in this chapter are made entirely of dipalmitoylphosphatidylcholine (DOPC) lipids and lack many of the components found in real cell membranes such as cholesterol, different lipids and membrane proteins. The differences between the model case and real biological membranes mean that absolute curvature predictions from this modelling should be avoided. However, this analysis suggests that the relative effects of surface attraction, pore radius and pore taper on membrane curvature can inform the design of materials targeting cell-membrane manipulation.

Changing the cholesterol content in these membranes from 0 to 10% showed no membrane curvature difference for similar cases (see Figure 2.7). The surface attraction of the substrates is controlled by modifying the depth of the Lennard-Jones potential well between

surface beads and lipid headgroups. This approach can be compared to modifying the surface charge of a surface to improve adhesion of cells. This can be achieved experimentally using techniques such as oxygen plasma treatments, polyelectrolyte layer coatings, or self-assembled monolayer coatings. [222] In the solvent explicit simulations below, we use surface charge to improve membrane adhesion to the wafer.

2.3.2 Analysis of Membrane Properties

After evaluating the general deformation of these membranes, the membrane properties at regions of curvature were investigated . Figures 2.8a, b, c and d show heat maps of lipid orientation, lipid movement, area-per-lipid and membrane thickness respectively for membranes interfaced with various wafers. These maps show that not only do the nanopores induce curvature, but they also modify key membrane properties around curvature. For a pore radius of 8 nm and a pore taper of 2.5 nm, the area-per-lipid in curved regions increases from between 50 to 60 $\mathring{A}^2$ to almost 80 $\mathring{A}^2$ (Figure 2.8b). [225, 226] This is significant as increased lipid spacing may result in increased localization of membrane-embedding proteins, as well as for localization of larger lipids or transmembrane proteins. [84, 227] This change in area-per-lipid is not an artefact due to periodic boundary conditions as the membranes are simulated as ribbons, periodic in only the y-direction, allowing them to change shape with ease in the x-direction to avoid generating tension as they deform on the pores. This freedom is illustrated in Figures 2.8b to 2.8d, for a pore taper of 2.5 nm, where the unrestricted sides of the membrane have freely moved across their periodic boundaries. Regions of membrane curvature have higher areas-per-lipid and thinner membranes. Figures 2.9, 2.10, 2.11 and 2.12 show the lipid orientation, movement, area-per-lipid and membrane thickness maps for all the parameters investigated in this study.

Increased lipid movement is observed where the membrane is suspended across the pore opening in the center of the simulation cell. The increased movement in this region can be attributed to the lack of wafer-membrane interactions, which might otherwise dampen lipid diffusion in both leaflets where the wafer and membrane are in contact. This is consistent with the observed increase in lipid velocity with decreasing surface attraction (Figure 2.8d). Despite these local changes in lipid dynamics, the overall membrane diffusion parameters, calculated using the g_msd tool in GROMACS, which were found to be between 4 and 5 $\times$ 10^{-7} cm^2 s^{-1}, consistent with prior reports. [57] Such changes in lipid dynamics could be connected to phase separation behaviour observed in pore-spanning lipid bilayers. [228]

Our simulation model indicates that unperturbed membranes have a thickness of about 3.5 nm, consistent with physical measurements of DOPC bilayers. [225, 226] At regions

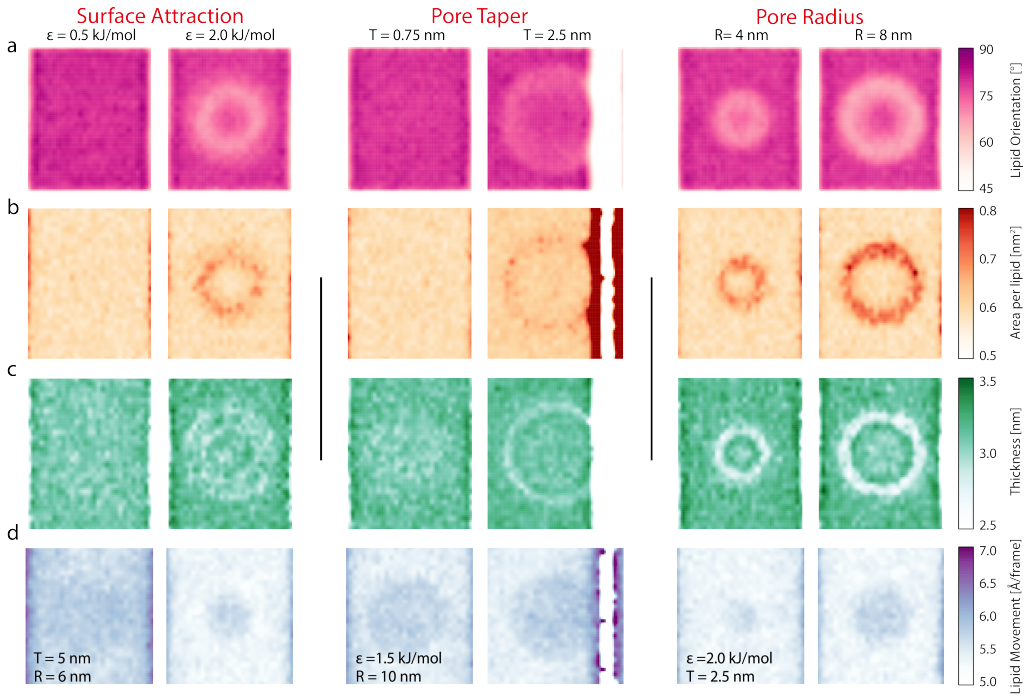

Figure 2.8: Heat maps of local membrane properties of the upper leaflet viewed from above showing (a) lipid orientation along x-y plane, (b) membrane area-per-lipid, (c) membrane thickness and (d) lipid movement for membranes under various conditions showing the effects of surface attraction, pore taper and pore radius on final membrane properties. Reproduced with permission from Belessiotis-Richards *et al.* [159] Copyright 2019, American Chemical Society.

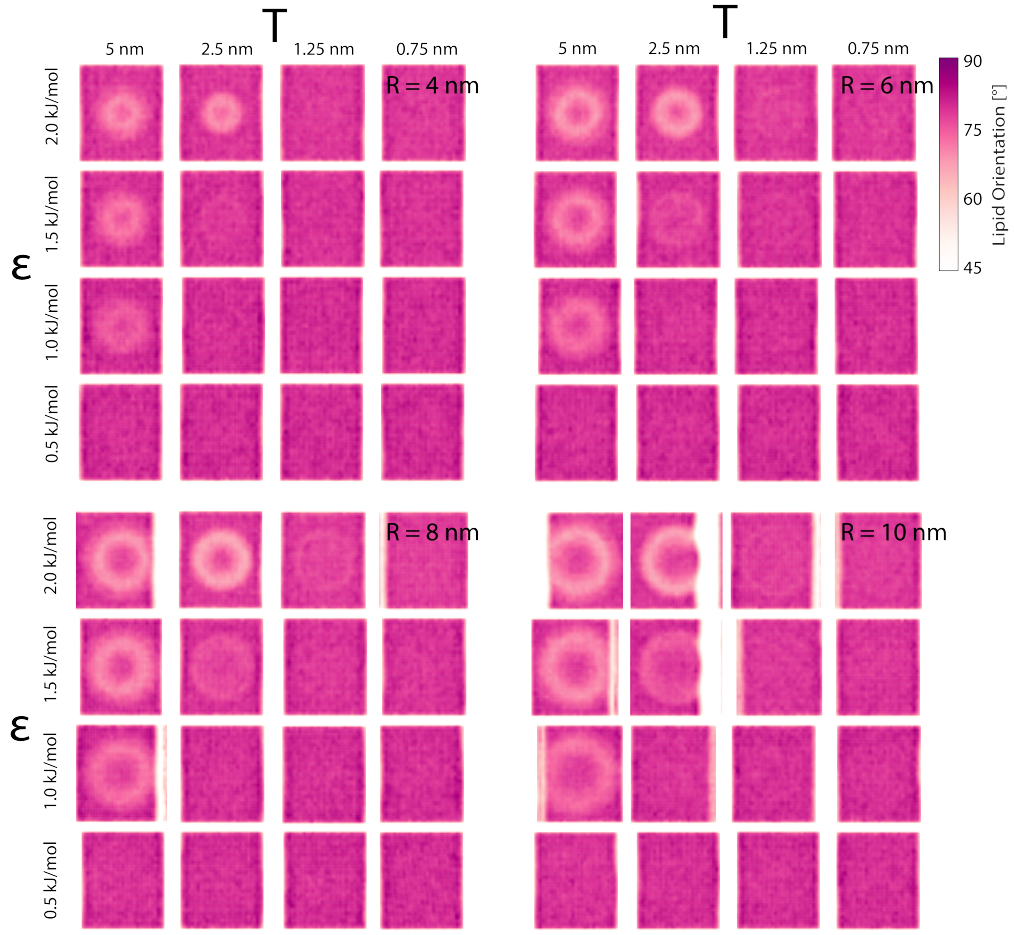

Figure 2.9: Heat maps showing lipid orientation along x-y plane for all wafer parameters (pore taper, T; pore radius, R; and surface attractiveness, ϵ) simulated in this study. Reproduced with permission from Belessiotis-Richards *et al.* [159] Copyright 2019, American Chemical Society.

of membrane curvature , we observe a taper and surface-attraction dependent decrease in membrane thickness from 3.5 to about 2.5 nm. This membrane thinning may have biological implications, for example, resulting in short transmembrane proteins preferentially localizing to such regions. Such proteins typically disrupt membranes to hide their hydrophobic residues and force them into thinner assemblies. [229, 230] We suspect that these nanostructure-induced structural defects may be present in many bio-interfacing applications. Such changes in membrane geometry may play a significant role in the cellular response to such surfaces.

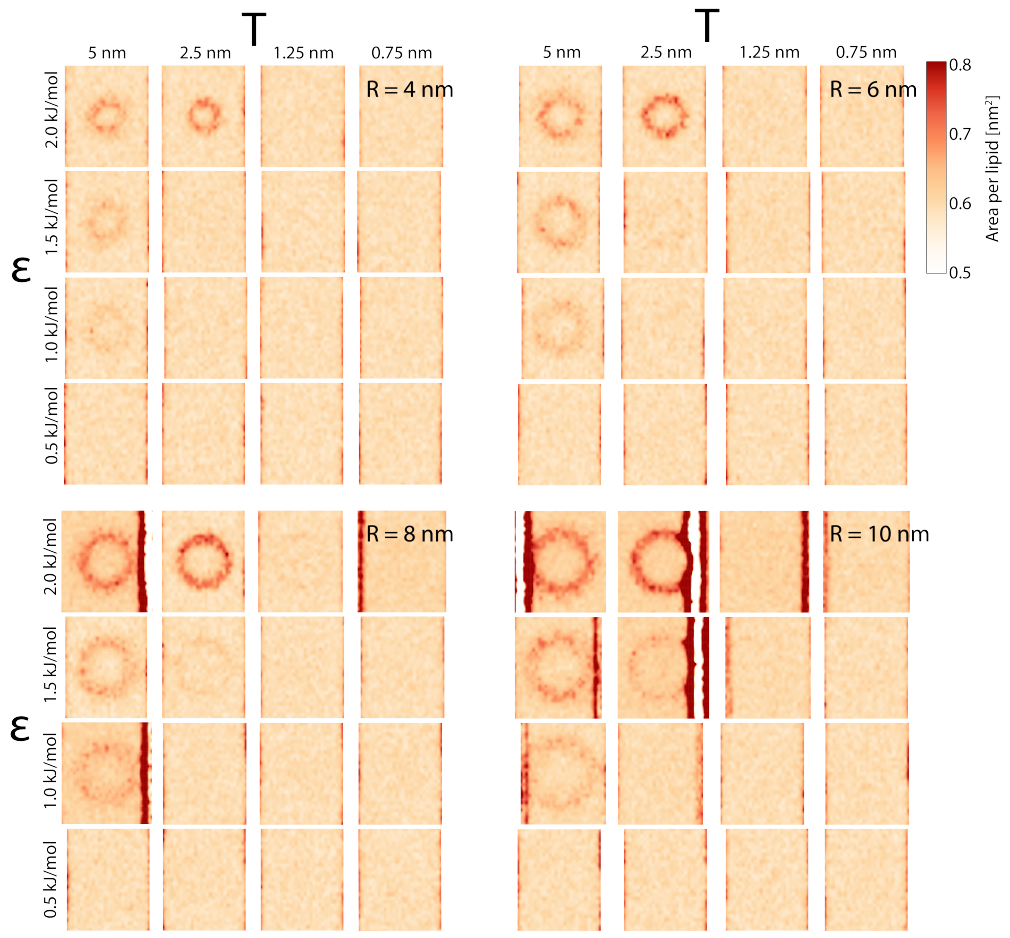

Figure 2.10: Heat maps showing area-per-lipid for all wafer parameters (pore taper, T; pore radius, R; and surface attraction, ϵ) simulated in this study. Reproduced with permission from Belessiotis-Richards *et al.* [159] Copyright 2019, American Chemical Society.

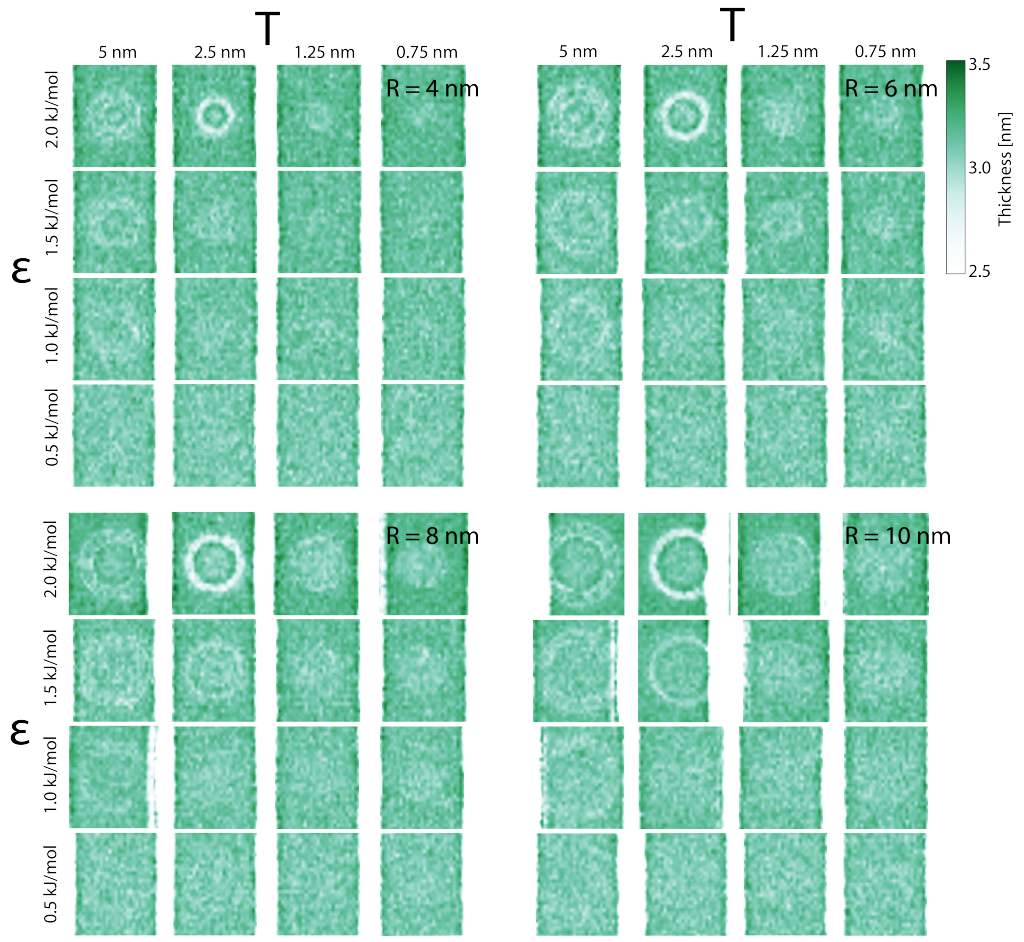

Figure 2.11: Heat maps showing membrane thickness for all wafer parameters (pore taper, T; pore radius, R; and surface attractiveness, ϵ) simulated in this study. Reproduced with permission from Belessiotis-Richards *et al.* [159] Copyright 2019, American Chemical Society.

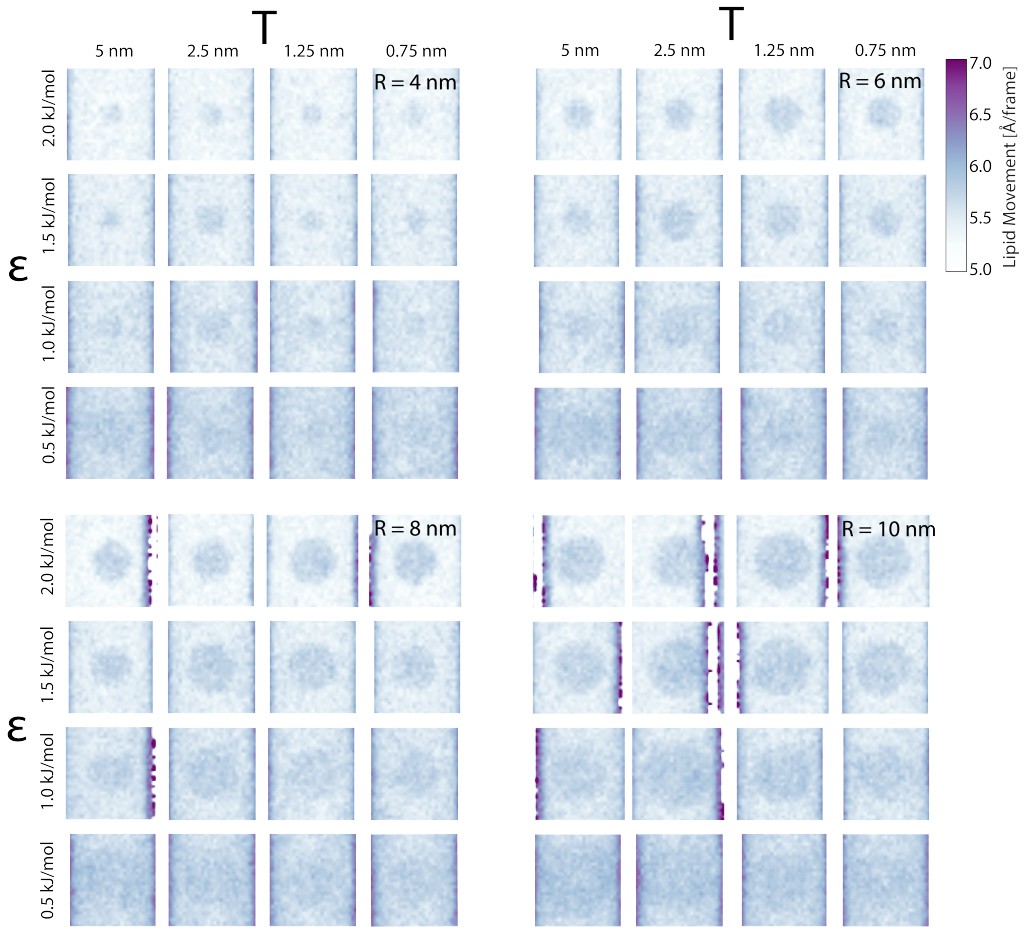

Figure 2.12: Heat maps showing membrane lipid movement for all wafer parameters (pore taper, T; pore radius, R; and surface attractiveness, ϵ) simulated in this study. Reproduced with permission from Belessiotis-Richards *et al.* [159] Copyright 2019, American Chemical Society.

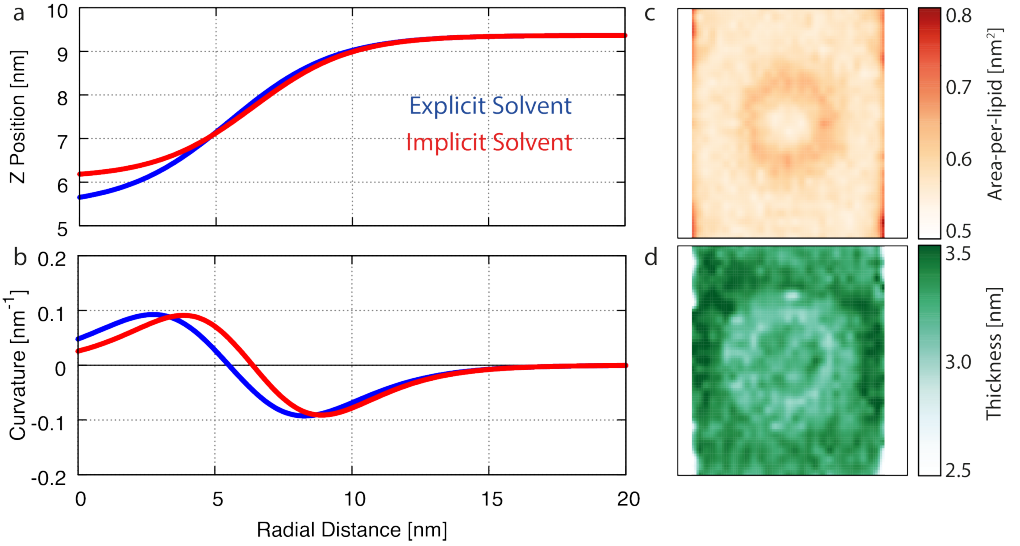

Figure 2.13: Comparison of explicit and implicit solvent model for nanopore-deformed membrane showing (a) membrane profile and (b) curvature values. (c) Area per lipid and (d) thickness heat maps of explicit solvent membrane showing similar patterns to implicit solvent model. Reproduced with permission from Belessiotis-Richards *et al.* [159] Copyright 2019, American Chemical Society.

2.3.3 Biological Implications of Curvature

Regions of membrane curvature can act as hotspots for certain membrane-mediated cellular processes and may modulate cellular function. [190, 193] To test this, we combined a nanopore-deformed membrane (R = 6 nm, T = 5 nm and ϵ = 2.0 kJ/mol) with a membrane-active Epsin N-terminal Homology (ENTH) protein domain. This case nanopore was selected in order to have a balanced area of curved and flat membrane regions so as not to bias the interaction of the ENTH domain with the membrane. This domain binds charged phosphoinositide (PIP) lipids in the cell membrane and plays a crucial role in endocytosis as a structural component of Epsin. [231–233] The ENTH domain is the main membrane binding motif of Epsin and has been shown to recognize and localize to regions of membrane curvature. [234] In these simulations, spontaneous and sustained localization of the domain was observed to membrane curvature regions for up to 4 μs of simulation time. Flat membranes showed no binding of the domain as it gets trapped at the free edges of the membrane where there is significant hydrophobic exposure. Implicit and explicit solvent models showed little difference between membrane properties (Figure 2.13).

Figure 2.14a shows the crystal structure of the ENTH domain and a schematic of its orientation when bound to the membrane with helix H0 interacting with the hydrophobic core of

the membrane. Figure 2.14b shows the hydrophobic contacts between the protein residues and lipid tails evaluated during simulation. This Figure shows insertion of the domain's H0 helix into the hydrophobic region of the membrane (residues 0 to 19) as well as compression of the domain upon insertion to allow for increased access by other hydrophobic residues (approx. residues 40 to 60). These residues are highlighted on the domain crystal structure shown in Figure 2.15a. The protein remained bound to the membrane throughout the simulation (Figure 2.15b) and its radius of gyration was stable throughout (Figure 2.15c). This finding is consistent with spontaneous localization of proteins in prior models of buckled membranes with pre-inserted proteins and peptides. [235] Figure 2.14c plots the histogram of the radial location of the domains center of mass (CoM) during simulation, showing preferential localization at a radius of approximately 10 nm from the central pore. These simulations support the notion that regions of membrane curvature are bioactive. Albeit without PIP lipids, these simulations show that the ENTH domain spontaneously localizes to membrane curvature. The domain remains bound for long simulation times (up to 4 μs modelled here) mainly due to the action of its amphipathic H0 helix (Figure 2.15a). [156] This suggests that other proteins or moieties within the cell containing amphipathic residues could preferentially localize at these regions. One could propose a mechanism by which nanotopographical tools could be used to artificially hijack and confine membrane-mediated intracellular processes through induction of nanoscale membrane curvature. This result may shed led light on the experimental observations by Gopal *et al* of endocytosis localized around nanoporous nanoneedles. [190] Indeed, the tight wrapping of the cell around nanoporous materials could induce nanoscale curvature in the cell membrane which might then stimulate the preferential localization of proteins and maybe even endocytosis at those regions.

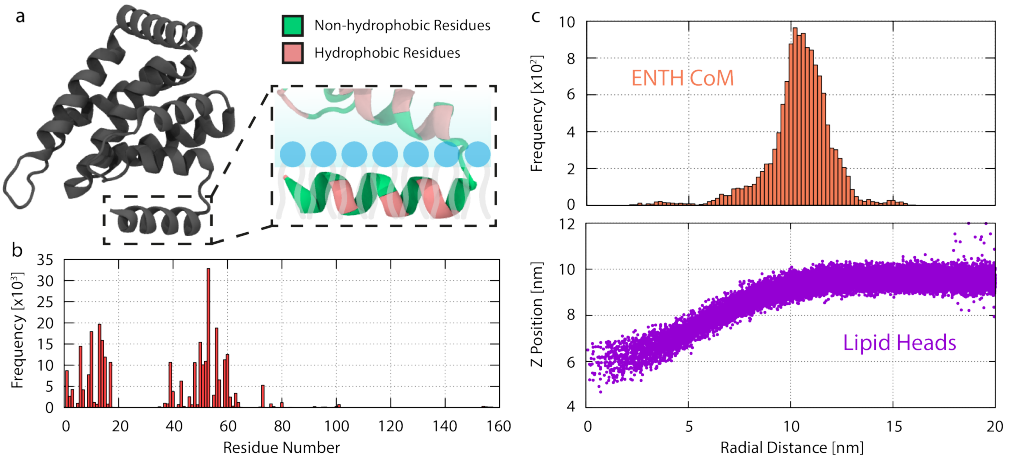

Figure 2.14: (a) Crystal structure of the ENTH domain of Epsin-1 and representation of its conformation when bound to the membrane (light blue) with hydrophobic and non-hydrophobic residues highlighted, (b) histogram showing statistical frequency of contacts between lipid tails and the protein residues during simulation, (c) histogram showing statistical frequency of the domain center of mass (CoM) for 4 μs of production MD and inner-leaflet lipid heads showing localization of the protein to membrane curvature at around 10 nm away from central pore, note that both plots in (c) share the same x-axis. Reproduced with permission from Belessiotis-Richards *et al.* [159] Copyright 2019, American Chemical Society.

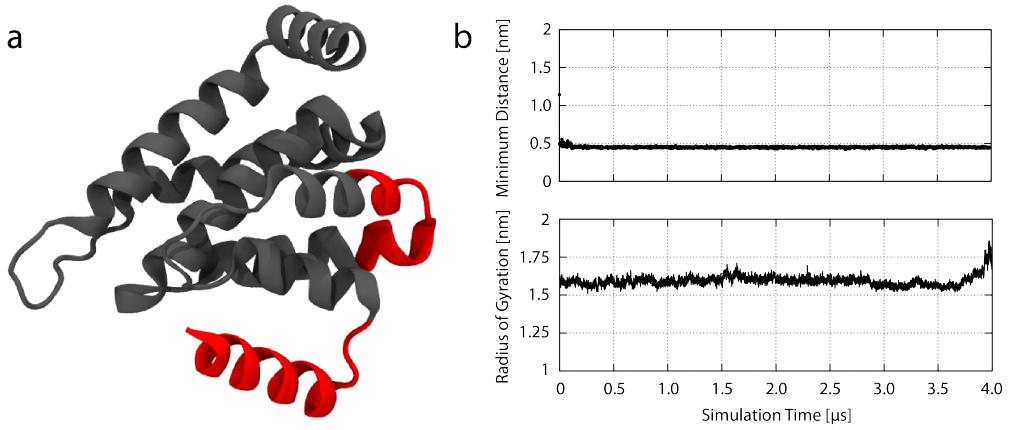

Figure 2.15: Additional protein results showing (a) the ENTH domain with hydrophobic contact residues highlighted in red (PDB: 1H0A.pdb. PIP2 not shown), (b) minimum distance between ENTH domain and DOPC lipids during simulation showing constant contact and ENTH radius of gyration showing no denaturation of the domain during simulation. Reproduced with permission from Belessiotis-Richards *et al.* [159] Copyright 2019, American Chemical Society.

2.4 Outlook & Conclusion

In conclusion, this chapter explored how nanopores can influence and deform cell membranes. A series of nanopore design parameters were defined, including pore radius, surface attraction and pore taper, which influence membrane curvature and can be employed to inform the design of nanostructured biomaterials. Pore taper was discovered to strongly influence membrane curvature, and this parameter could be readily tailored using common microfabrication techniques.

Membrane properties were modified in regions of curvature with greater lipid-per-area spacing and decreased thickness. Membrane curvature was confirmed to stimulate preferential localization of the membrane-active ENTH domain. This chapter furthers our knowledge of the interface between biology and nanoporous surfaces, and supplements our understanding of recently reported observations of increased endocytosis localization around porous silicon nanoneedles. [190]

Further work is needed to improve our understanding of the effects of nanotopography on cell membranes. The model presented in this chapter is limited by the use of a simple membrane composition and its size, two factors which may play a significant role in experimental systems. The nanopore curvature systems developed in this chapter is highly controllable and can facilitate further theoretical studies on the effects of membrane curvature on protein binding, protein function and protein-lipid interactions. Finally, this chapter presents a first foray into understanding the processes behind material-mediated drug delivery and the conclusions could serve to design a new generation of nanomaterials for drug delivery and cellular manipulation.

Chapter 3

Membrane Curvature Binding and Localization of the ENTH Domain

Following on from the nanoporosity model presented in the previous chapter, this chapter explores in more detail the membrane binding and curvature sensing of a curvature-active protein, the ENTH domain. In particular, this chapter investigates the structural basis for how this domain senses membrane curvature and how it interacts with PIP2 lipids. This chapter is adapted with permission from work published in Belessiotis-Richards *et al*. [114]

3.1 Introduction

As as described in the Introduction, membrane curvature is critical for essential cellular functions such as clathrin-mediated endocytosis (CME). CME relies on the complex coordination of phosphoinositide lipids with curvature proteins and the actin machinery to progress. PI(4,5)P2 (referred to herein as PIP2), in particular, is a key lipid in this process. [236] Many of the proteins involved in CME contain PIP2-binding domains such as the pleckstrin-homology (PH) domain of FCHo, the AP180 N-terminal homology (ANTH) domain of AP180/CALM and the epsin N-terminal homology (ENTH) domain of the epsin family. A number of these PIP2-binding domains are also curvature-active. While the individual roles of membrane curvature and phosphoinositides in endocytosis have been independently studied with respect to protein reshaping of membranes and phosphoinositide recycling in CME, [89, 112, 237, 238] there is a gap in our knowledge of the combined roles of PIP2 with membrane curvature. There are almost no computational studies directly studying membrane curvature sensing by proteins in the presence of PIP2 lipids. Chapter 2 explored how nanoscale membrane curvature could be induced through inter-

facing membranes with nanoporous wafer. Expanding on this, this chapter investigates in more detail the binding and membrane curvature sensing of a key curvature-active protein domain, the ENTH domain, in the presence of PIP2.

When the ENTH crystal structure was solved by Ford *et al*,[109] it was shown that Epsin-1 could drive membrane curvature through its ENTH domain due to the insertion of an N-terminal amphipathic α helix, referred to here as H0. Ford *et al*'s work suggests that this helix is formed as a structural consequence after binding PIP2. H0's amphipathic nature then prefers for it wedge into the membrane, creating membrane curvature. Since then, the ENTH domain has become a model for curvature-active protein domains and has been shown to spontaneously sense membrane curvature both experimentally and computationally. [156, 239–241] Hydrophobic insertion of amphipathic helices is a widely accepted mechanism for generating membrane curvature in cells. [92, 242, 243] Many curvature-active proteins contain amphipathic helices such as N-BAR-containing proteins involved in endocytosis, as well as Arf1 and Sarlp. [77, 244] However, recent studies suggest that the exact role of amphipathic helices is not so clear. Membrane composition, in particular the presence of anionic lipids, can play a significant role in modulating the curvature activity of amphipathic helix-containing proteins. [245–247] Chen *et al* have also suggested that hydrophobic residue insertion only plays a minor role in membrane curvature generation by endophilin. [248] Similarly, Zeno *et al* have shown that disordered proteins can sense membrane curvature via purely non-specific interactions, suggesting that, even without the presence of a structural sensing motif, electrostatic and entropic forces can drive curvature sensing. [249] Finally, Mu *et al* have shown that PIP2 localization to regions of membrane curvature can initiate a phagocytic pathway which is suggested to have been at the origin of receptor-mediated phagocytosis. [250]

The results in this chapter explore in greater detail how the ENTH domain senses membrane curvature in the presence of PIP2, what role the H0 terminal helix plays in curvature sensing, and how domain backbone flexibility can affect curvature sensing. Although hydrophobic insertion is well-studied in the context of membrane curvature sensing, it has not been explored at the molecular level in combination with PIP2. We have previously assumed PIP2 to be an important but relatively neutral player in the complex choreography of membrane curvature sensing. But could PIP2 lipids be playing a more active role in this process? In this chapter, a model curvature sensing protein is studied, the ENTH domain, and its interaction not only with curvature but also with its key binding partner, PIP2.

Using coarse-grained molecular dynamics simulations, two crystal structures of the ENTH domain were studied, one with and one without its terminal H0 helix (shown in Figure

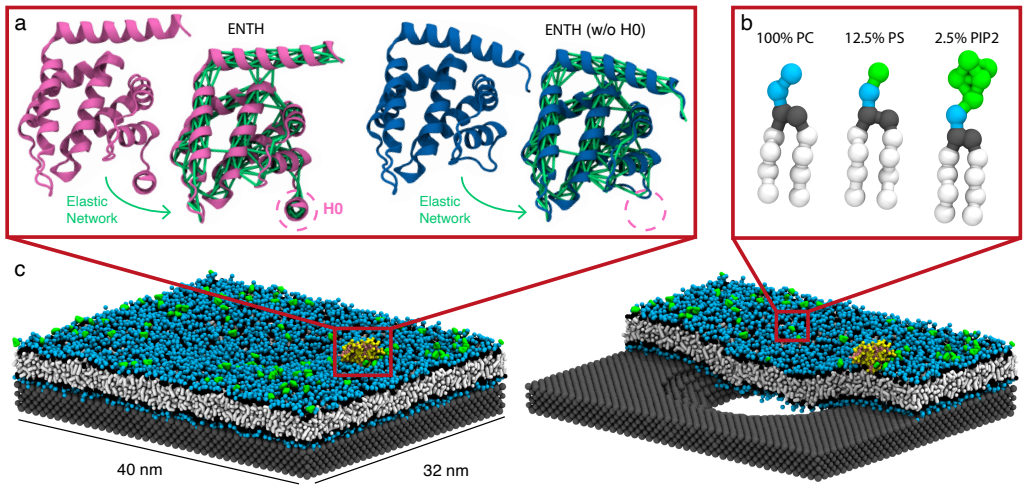

Figure 3.1: (a) Crystal structures of the ENTH with (PDB code: 1H0A.pdb) and without (PDB code: 1EDU.pdb) its terminal domain α-helix (H0) alongside the elastic network applied to fix secondary structure. (b) Membrane compositions used to study ENTH binding and curvature localization (100% PC, 87.5% PC + 12.5% PS, and 97.5% PC + 2.5% PIP2). The white, gray, blue and green beads represent the hydrophobic tails, ester linkers, phosphatidylcholine headgroup and negatively charged groups respectively. (c) Snapshots of the simulation set-up and a slice through the middle of the nanopore-deformed membrane along y-axis (PIP2 lipids are highlighted in green, PC lipids are highlighted in blue). Reproduced with permission. [114] Copyright 2020, American Chemical Society.

3.1a). For each of these structures, the interaction of the domains with curved phosphatidylcholine (PC) membranes containing various proportions of negatively charged lipids was also simulated. The three membrane variants investigated are pure PC, PC with 12.5% phosphatidylserine (PS), and PC with 2.5% PIP2. Both crystal structures were simulated both with and without a rigid elastic network used to fix the tertiary protein structure during simulation.

Following the previous chapter's work on nanopore-induced membrane deformation, it is suggested that interfacing cells with nanostructured materials can induce physical as well as functional changes within the cell, potentially allowing artificially localized cellular function. Understanding these effects will enable new hypothetical answers to both fundamental questions in cell and structural biology. For example, how important is the terminal alpha helix insertion for curvature sensing and what role does PIP2 play? This information will also be useful in the development of nanostructured biomaterials for applications in drug delivery and cellular manipulation. For example, how does nanoscale curvature affect the local distribution of lipids and proteins in the cell membrane? [23, 172, 193, 205, 251]

Three curved membrane compositions were studied containing either: 100% PC lipids, PC and 12.5% PS, or PC and 2.5% PIP2 in the upper leaflet (values shown are number percent). The PS and PIP2 content in these membranes were chosen to present the same net negative charge on the membrane. These membranes were interfaced with a negatively charged nanoporous substrate containing a central pore of 12 nm in diameter with tapered edges of 5 nm, designed to promote membrane curvature. The ENTH domain was also investigated interacting with flat membranes of the same compositions.

Two crystal structures of the ENTH domain were selected for this chapter, differing only in the presence or absence of its N-terminal α helix, H0. Figure 3.1a shows both crystal structures of the ENTH domain investigated. Each of these crystal structures was simulated with and without the presence of an elastic network. An elastic network (shown in green in Figure 3.1a) maintains the overall tertiary and quaternary structure of a protein during simulations allowing for a very limited degree of local flexibility. Figure 3.2 shows the overlapped crystal structures of the two ENTH domains showing that these structures are structurally very similar apart from H0. Within this chapter, the ENTH domain containing its H0 helix will be refered to simply as "ENTH" and the ENTH domain without H0 as "ENTH (w/o H0)". Figure 3.1b shows the coarse-grained representations of the lipid compositions used while Figure 3.1c shows snapshots of the simulation model and a cross-section of the membrane highlighting its curvature. Figure 3.3 presents additional detailed snapshots of the simulation systems studied in this chapter for (a,c) curved and (b) flat membranes . A full list of the simulations performed can be found in Table 3.1

Table 3.1: : Summary of the simulations carried out for this study. *N denotes the number of simulations run, all protein simulations were performed both with and without elastic networks. ** 97.5% PC and 2.5% PIP2. *** 87.5% PC and 12.5% PS. **** Two independent starting positions were used for the flexible ENTH (w/o H0)/PC/PIP2 simulations.

Simulation ID	Protein	Membrane	N*	Duration (μs)
Curved Membrane (36 x 40 x 35 nm cell)				
ENTH/PC	ENTH	PC	2x8	10
ENTH (w/o H0)/PC	ENTH (w/o H0)	PC	2x8	10
ENTH/PC/PIP2	ENTH	PC/PIP2**	2x8	10
ENTH (w/o H0)/PC/PIP2	ENTH (w/o H0)	PC/PIP2	3x8****	10
'Mutant' ENTH (w/o H0)/PC/PIP2	ENTH (w/o H0)	PC/PIP2	8	10
ENTH/PC/PS	ENTH	PC/PS***	2x6	10
ENTH (w/o H0)/PC/PS	ENTH (w/o H0)	PC/PS	2x6	10
Flat Membrane (20 x 20 x 20 nm cell)				
Flat/ENTH/PC	ENTH	PC	2x5	4
Flat/ENTH (w/o H0)/PC	ENTH (w/o H0)	PC	2x5	4
Flat/ENTH/PC/PIP2	ENTH	PC/PIP2	2x5	4
Flat/ENTH (w/o H0)/PC/PIP2	ENTH (w/o H0)	PC/PIP2	2x5	4
Flat/ENTH/PC/PS	ENTH	PC/PS	2x5	4
Flat/ENTH (w/o H0)/PC/PS	ENTH (w/o H0)	PC/PS	2x5	4

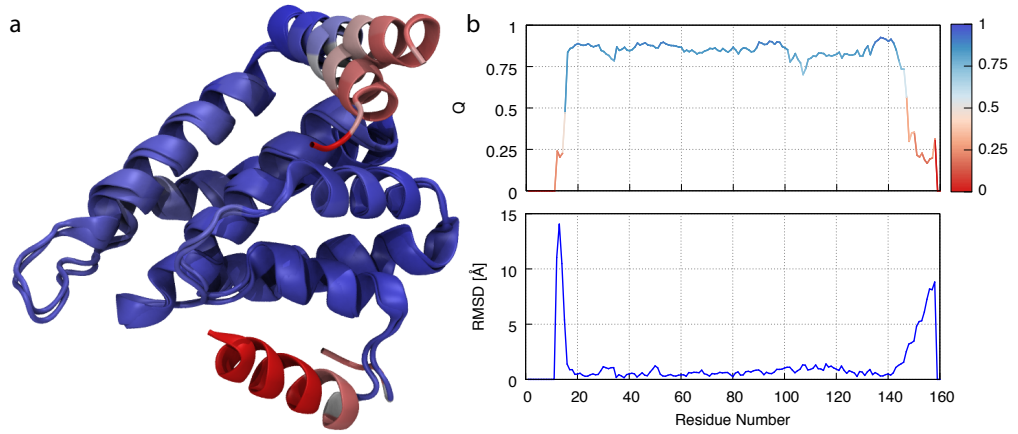

Figure 3.2: (a) Structural comparison of the two ENTH domain structures used in this study (1EDU.pdb and 1H0A.pdb) colored by similarity between the structure. (b) Q values and radial mean squared distance (RMSD) difference between two ENTH domain structures used in this study as a function of residue number. Reproduced with permission. [114] Copyright 2020, American Chemical Society.

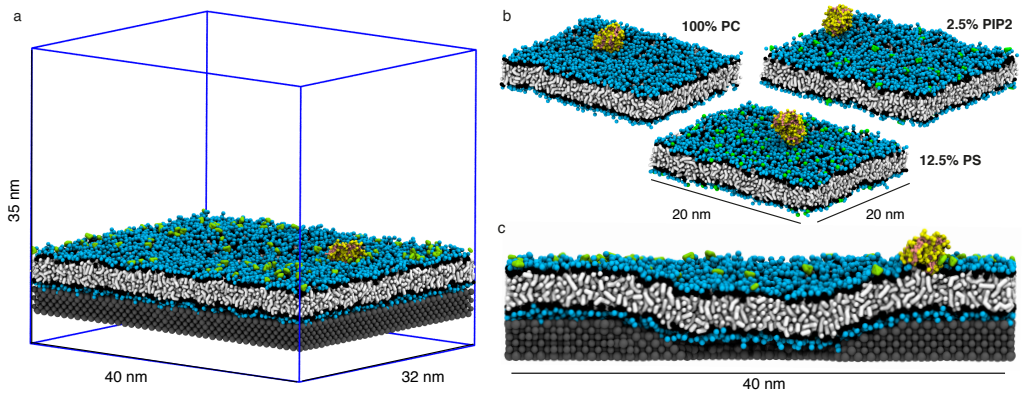

Figure 3.3: Snapshots of the systems studied for this work. (a) Curved membrane showing box size. (b) Flat membranes of different compositions and (c) a slice through the middle of the system shown in (a) highlighting membrane curvature. Reproduced with permission. [114] Copyright 2020, American Chemical Society.

3.2 Methods

3.2.1 Simulation Details

All simulations were performed using Gromacs 4.6.7. [215] Protein simulations were performed at 323 K using the Martini 2 force-field with explicit water. [52] The temperature was coupled to a velocity rescale thermostat using a time constant of 1 ps with the protein, membrane, wafer, solvent and ions each being coupled independently. The protein crystal structures were from the RCSB protein data base: ENTH with helix (Protein Data Bank (PDB) code: 1H0A.pdb) and ENTH without helix (PDB code: 1EDU.pdb). Proteins were coarse-grained using the martinize.py script from cgmartini.nl and an elastic network was added, where noted, using a force constant of 500 kJ/mol and a cut-off distance of 0.9 nm. The systems were equilibrated for 20 ns using a 0.02 ps time step and a semi-isotropic Berendsen barostat using a time constant of 1 ps. For production runs, a 0.03 ps time step was used with the Parinello-Rahman barostat was used and a 12 ps time constant. The protein center-of-mass was computed using the g_traj tool and contacts analysis was performed using the $g_mindist$ tool, both in Gromacs. [215] The velocity rescaling thermostat was used throughout.

3.2.2 Trajectory Analysis

All snapshots were taken using VMD. [216] The heatmaps and radial distribution histograms were computed from the protein center-of-mass (CoM) data extracted from the simulations using the g_traj tool mentioned above. Heatmaps in Figure 3.5 were created by converting the x-y CoM data into absolute distances from the central pore (x=16 and y=20). This data was then mapped onto a 50 by 50 grid of equally spaced bins (x limits = 0-20 nm and y limits = 0-25 nm). The histograms from which the fold change is calculated were determined by converting the x-y CoM data into radial distance from the central pore following:

$$r = \sqrt{(x-16)^2 + (y-20)^2} \tag{3.1}$$

Where r is the radial distance of the protein as a function of time and x and y are the x and y components of the protein CoM at a given frame. This radial data was then converted into a histogram over 100 equally spaced bins between 0 and 25 nm. In addition, kernel density estimates of the raw radial data was computed using $stats.gaussian_kde$ command from the python scipy package. Both the x-y histograms and radial histograms were normalized so that the sum over each bin in the histogram equals to 1.

3.2.3 Structural Analysis

The g_rmsf tool was used to compute protein residue dynamics (RMSF and RMSD) and the g_covar tool was used to compute average structures of the domain. The backbone RMSD values were calculated using VMD.

3.2.4 Wafer Construction

The nanoporous wafer was constructed following the previous chapter and its corresponding publication. [159] 40 by 40 nm PC-only, PC/PS and PC/PIP2 membranes were first built using the $insane.py$ tool and were sectioned into ribbons by removing 4 nm from either edge of the membrane along the x-direction, thereby leaving the membrane continuous only along y. [218] These were equilibrated for 20 ns and simulated for 300 ns under the same conditions mentioned above. Following this, the membranes were placed above the nanoporous wafer and again equilibrated for 20 ns and simulated for 300 ns in order to interface with the wafer. Once curved on the wafer, the unit cell was sliced from 40 by 40 nm to 32 by 40 nm in order to have a fully continuous membrane. This method ensures that no artificial tension is introduced in the membrane during the curving process.

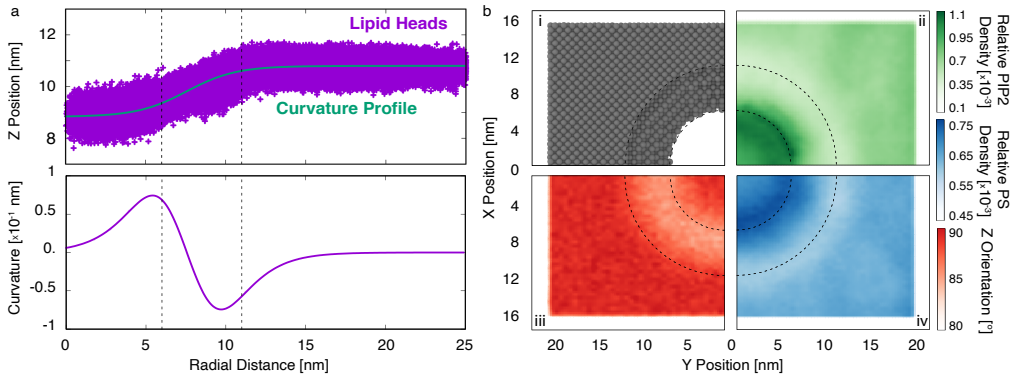

Figure 3.4: Characteristics of the curved membrane showing (a) average position of PC lipid heads, curvature profile and the computed curvature of the membrane as a function of radial distance from the central pore. (b) Heat maps showing (i) a top-down snapshot, (ii) relative PIP2 density, (iii) lipid orientation along the x-y axis defined by a vector connecting the lipid headgroup bead to its first ester bead and (iv) PS density on the curved membrane. Dashed lines represent the start and stop of tapered region of underlying nanoporous wafer approximating the region of membrane curvature. Reproduced with permission. [114] Copyright 2020, American Chemical Society.

3.3 Results & Discussion:

3.3.1 Characterization of Membrane Curvature

Similarly to the previous chapter, the membrane curvature in this system is illustrated in Figure 3.4. This Figure shows the average lipid head positions in the upper leaflet and its corresponding membrane curvature profile evaluated following the same approach as Chapter 2. The maximum radius of membrane curvature corresponds to approximately 12 nm and is located at around 10 nm away from the central pore. Computed spatial properties of the membrane are shown in Figure 3.4b. Local PIP2 and PS density diminishes at regions of curvature while being enriched at concave curvature regions, in the pore center and edges (Figure 3.4b ii and 3.4b iv). The curvature of the membrane around the central pore can be seen from the lipid orientation along the z-axis in Figure 3.4b iii.

3.3.2 Curvature Sensing of the ENTH Domain

Proteins were initially placed approximately 1.5 nm above both curved and flat membranes and left to interact freely. Figure 3.5 shows top-down heat maps of the protein domains centre-of-mass (CoM) on curved membrane with and without an elastic network. This Figure also shows the same data analysed a function of radial distance from the central pore, normalized to the radial charged lipid density profile (the PC density profile is used

for the case where no PIP2 or PS is present). This fold change metric represents the degree to which protein localization is driven by lipid density and is determined according to equation 3.2.

$$Fold\ Change(r) = \frac{\hat{f}(r)}{\hat{g}(r)} \tag{3.2}$$

Where r is the radial distance from the central pore, $\hat{f}$(r) is the kernel density estimator of the protein, and $\hat{g}$(r) is the kernel density estimator of the lipid both as a function of radial distance. The lipid of interest, evaluated in $\hat{g}$(r), is chosen depending on the simulation case; i.e. for PC-only, PS-containing and PIP2-containing cases, the radial distribution of PC, PS and PIP2 lipids is used respectively. A fold change equal to one indicates that, at a given radial distance, the density of protein and lipid are equal. This suggests that the protein and lipids are perfectly tracking one-another. Fold changes above one indicate an increase in protein localization with respect to the underlying lipid. Values below one indicate reduced localization. If the fold change is either above or below one, this indicates that the protein is localizing independently of lipid positions. The raw histograms and kernel density estimates of protein and lipid localization used to calculate these fold changes are shown in Figure 3.6.

Flexible ENTH domains consistently localize to convex membrane curvature, at around 11 nm. The peaks in the respective fold change indicate that this localization is independent of changes in the underlying lipid density. This behaviour includes the expected localization of the ENTH domains on neutral PC membranes, due to the action H0, see Figures 3.5a and 3.5b. Unexpectedly, however, neither removing H0 (Figures 3.5c and 3.5d), nor adding PIP2 or PS to the membrane (Figures 3.5e-l respectively), changes this behaviour. This is contrary to the presumption that strong curvature sensitivity is dependent on the action of H0. Looking at the data presented in Figure 3.5 as a whole, we see that with and without H0, flexible ENTH domains behave similarly. This suggests that the ENTH domain may contain another curvature-active region other than H0. These simulations also suggest that the ENTH domain have improved curvature sensing when its tertiary and quaternary structure are flexible. Simulating with an elastic network reduces this curvature sensing ability, as indicated by smaller fold change in Figures 3.5b, d and h, and even removes curvature sensing entirely in the ENTH/PC/PIP2 case (Figure 3.5f). An elastic network increases the rigidity of the protein and hence reduces its ability to adapt to curvature in order to expose hydrophobic residues.

In figures 3.5f and h, an additional localization peak is present between 0 and 5 nm. These

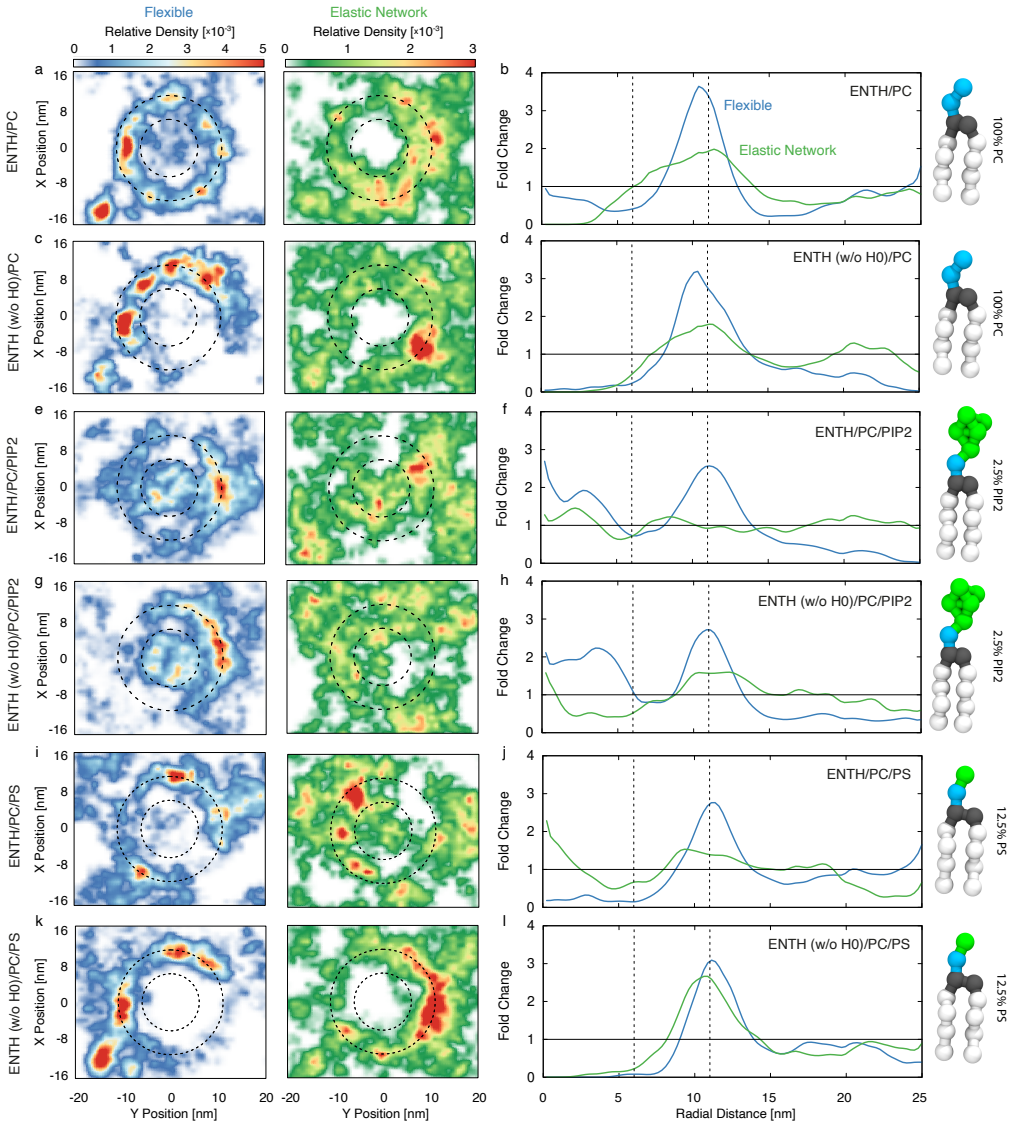

Figure 3.5: Statistical frequency heat maps showing center-of-mass positions of ENTH domains and density profiles normalized to lipid density for (a,b) ENTH domain and (c,d) ENTH (w/o H0) domain interacting with a curved PC-only membrane, (e,f) ENTH domain and (g,h) ENTH (w/o H0) domain interacting with a curved PIP2-containing membrane., (i,j) ENTH domain and (k,l) ENTH (w/o H0) domain interacting with a curved PS-containing membrane. Dashed lines represent the start and stop of tapered region of underlying nanoporous wafer approximating the region of membrane curvature. Adapted with permission. [114] Copyright 2020, American Chemical Society.

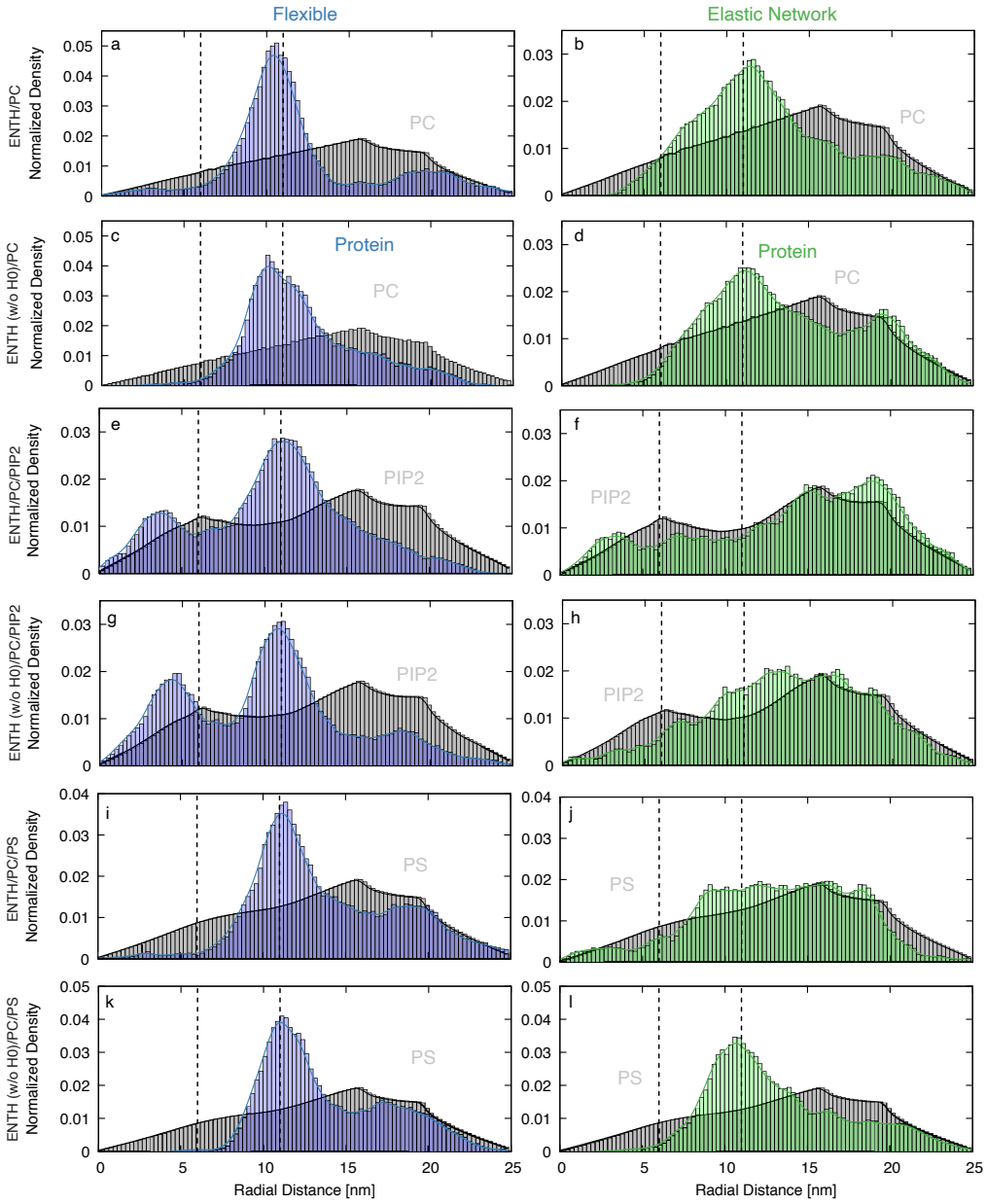

Figure 3.6: Protein and lipid density profiles normalized over 100 bins used to calculate fold change in ENTH domain localization behaviour in Figure 3.5. Each histogram was normalized to the total number of counts recorded for each simulation case. Note that the scalloped features at 16 nm and 20 nm are artefacts due to the rectangular simulation cell. Reproduced with permission. [114] Copyright 2020, American Chemical Society.

peaks are not present in the PC-only simulations (Figures 3.5b and d). The appearance of this new peak can be explained by the local enrichment of PIP2 in the central pore region as shown in Figure 3.4b ii and in Figures 3.6e and g. Hence, local enrichment of PIP2 can drive localization away from membrane curvature. This is interesting as, during endocytosis, PIP2 is significantly enriched at endocytic sites. [89] Ford *et al* showed that mutated ENTH domains (with disrupted H0 formation) still localized at endocytic sites. [109] These experimental results were explained as stemming from the local high concentration of PIP2 at these regions. These simulations support this theory and also suggest that this behaviour could be due to the action of another curvature-active region within the ENTH domain.

3.3.3 Lipid Binding of the ENTH Domain

The protein localization results examined in the previous section pointed to H0-independent membrane curvature sensing by the ENTH domains. To further this, the interactions of each residues in the domains with PC-, PC/PIP2- and PC/PS-containing membranes was analysed. The contacts of all residues in the domain with PC and PC/PIP2 membranes can be seen in Figure 3.7. The first column in this Figure (figures 3.7a) presents the hydrophobic contacts between the ENTH domain and the different membranes. A hydrophobic contact is defined as any contact between a protein residue and a lipid tail (white colored beads in Figure 3.1b).

When the ENTH domain has its H0 helix, consistent hydrophobic interactions between residues 3 to 15 are observed. These are absent in the ENTH (w/o H0) cases as this region corresponds to the location of H0 on the protein domain. However, hydrophobic contacts are also seen between residues 49 to 65. This second region is hydrophobically active in all ENTH (w/o H0) simulations (Figures 3.7a ii and 3.7a iv) but only in flexible ENTH cases with H0 (Figures 3.7a i and 3.7a iii). With an elastic network and H0, this region loses its hydrophobic activity. For clarity, this region is denoted as H3 as it corresponds approximately to helix 3 in the protein domain.

Looking closer at the sequence and structure of the ENTH domain in Figure 3.8, it can be seen that H3 has a strong hydrophobic surface, even more so than H0. In the elastic network ENTH (w/o H0) cases, the highest hydrophobic counts are seen at residues 48, 50 and 51 (Figure 3.7a ii and iv). These residues correspond to the "elbow" region of the protein which wants to be hydrophobically exposed. Even when the protein is rigid, this elbow region still inserts into the membrane. This suggest that, when the protein is flexible, H3 is free to expose more hydrophobic residues to the membrane and makes for stronger curvature sensing. This can be seen qualitatively in simulations snapshots presented Figure 3.9.

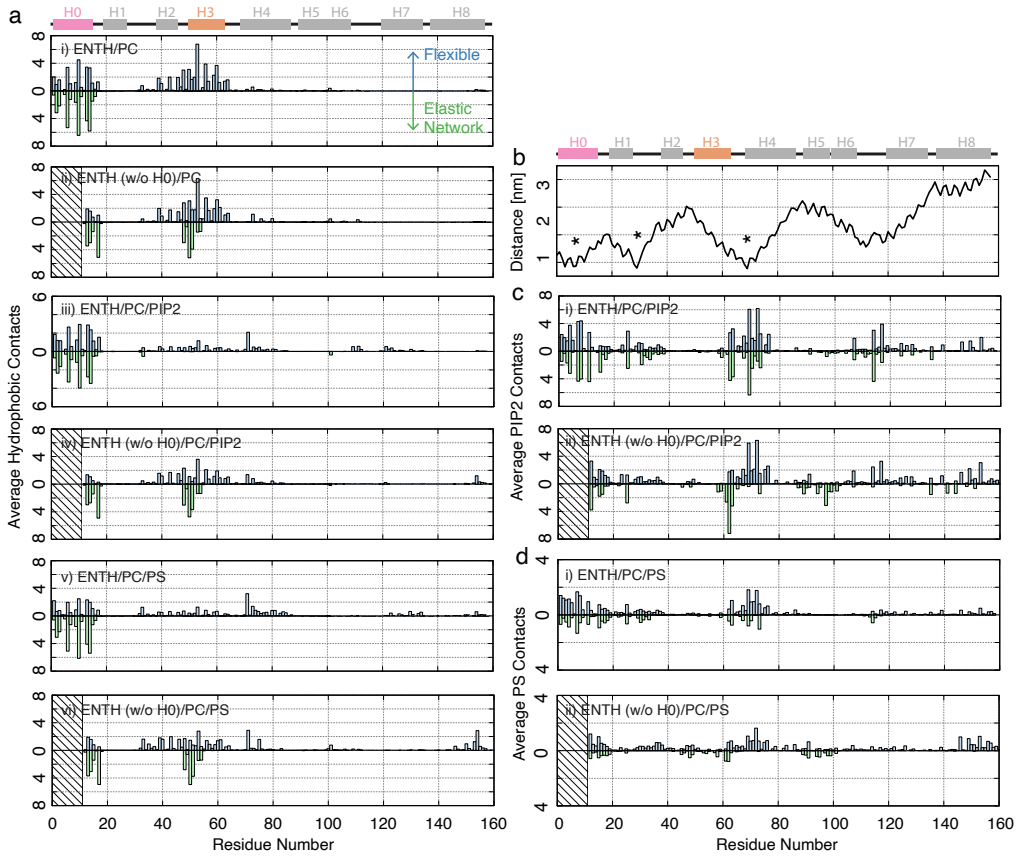

Figure 3.7: Contact analysis of all residues of the ENTH domain. (a) Average number of hydrophobic contacts of the ENTH domains in contact with PC-, PC/PIP2 and PC/PS-containing membranes. A schematic of the ENTH domains secondary structure as a function of residue number is represented above the figures, each block represents an alpha helix. (b) distance between PIP2 headgroup center-of-mass and each residue of ENTH computed from the crystal structure (PDB code: 1H0A.pdb). Black asterisks represent binding pockets of PIP2. (c) Average number of contacts with PIP2 headgroup of the ENTH domains in contact with PIP2 containing membranes. (d) Average PS headgroup contacts of the ENTH domains in contact with PS containing membranes. Adapted with permission. [114] Copyright 2020, American Chemical Society.

Here, a collapse in conformation of the flexible proteins is observed, which suggests the protein is maximizing hydrophobic exposure. Conversely, the proteins with elastic network are oriented away from the membrane as can only hydophobically insert one region (H0) or the other (H3). On flat membranes, the activity of H0 and H3 is reduced in the presence of PIP2 suggesting that their hydrophobic activity is curvature-driven (Figure 3.10 a). Flat PS-containing membranes still show strong hydrophobic activity however, which we can rationalize due to the strong charge attraction and small headgroup size of

the lipids driving the protein into close contact with the membrane.

This binding behaviour reinforces the observations of curvature sensing of ENTH (w/o H0) proteins in the previous section. These results suggest that the ENTH domain contains a complementary curvature-active structural region, H3, in addition to its amphipathic helix H0. When the ENTH domain is flexible it can adapt to membrane curvature and expose both H0 and H3 simultaneously. Elastic network simulations, on the other hand, force the domain to only expose one of these regions at a time.

In order to determine the binding pockets of PIP2 to the ENTH domain, the distance between the PIP2 headgroup CoM and each residue of the protein was calculated from Ford *et al*'s crystallographic work. [109] This is shown in Figure 3.7b where asterisks point to where PIP2 is expected to bind. Looking at the contacts between PIP2 and the protein residues in Figure 3.7c, consistent contacts are observed around residues 0 to 10, around residue 30 and between residues 65 and 75. These contacts match-up with the computed binding pockets in Figure 3.7b suggesting that PIP2 is binding correctly to both flexible and rigid ENTH domains. This binding functionality is also observed on PC/PS membranes, see Figure 3.7d, and on flat membranes, see Figures 3.10 c and d.

3.3.4 Structural Dynamics of the Flexible ENTH Domains

As a number of simulations of the ENTH domain were flexible, the structural dynamics of the protein were studied. This was done by averaging the protein structures over simulation ensembles for each case and comparing the Root Mean Squared Deviation (RMSD) between flexible and elastic network simulations. The RSMD as a function of residue number is shown in Figure 3.11a. Here fairly large RMSD values are observed across the residues due to the flexible nature of the proteins structure during simulation. However, two regions in Figure 3.11a stand out as dynamic in all cases, between residues 0 to 35 (pink asterisk) and residues 100 to 120 (black asterisk). These two regions are also represented in overlaid simulation snapshots in Figure 3.11b. These snapshots are purely representative and were taken at random times during simulation. An averaged view of the flexible proteins can be seen in Figure 3.12a. The internal Root Mean Squared Fluctuations (RMSF) and RMSD changes within each protein (not flexible compared to elastic) can be see as a function of residue number in figures 3.12b and c respectively.

In ENTH domains which contain H0, this first dynamic region (residues 0 to 35) can be associated with rotation/re-orientation of the H0 helix in the membrane along with associated motion of H1 and the disordered chain connecting H2. This re-orientation of H0 and H1 can be observed in figures 3.11b and 3.13. For ENTH (w/o H0) cases,

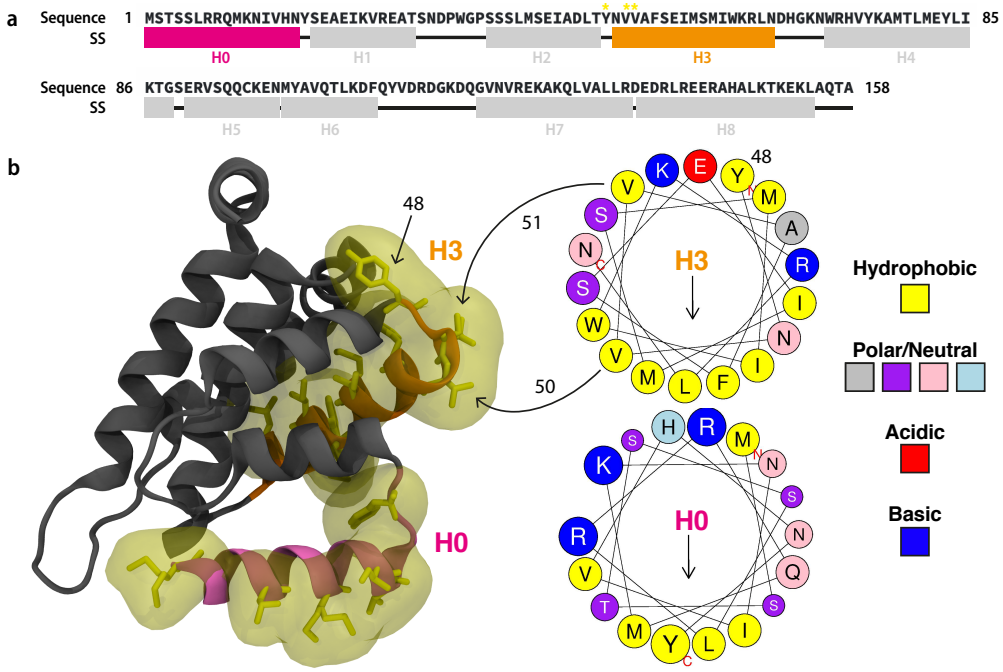

Figure 3.8: (a) Sequence and secondary structure of the ENTH domain highlighting helices H0 and H3 in pink and orange respectively. Residues 48, 50 and 51 are identified with yellow asterisks. (b) Crystal structure of the ENTH domain with hydrophobic residues of helices H0 and H3 highlighted in yellow and hydrophobic surfaces in transparent yellow along with helical wheels for helices H3 and H0 showing hydrophobic moment of each helix produced by HELIQUEST.1 Residues 48, 50 and 51 are marked on the wheel and structure as these residues are hydrophobically active in the elastic network ENTH (w/o H0) case (see Figure 4a ii and iv). Reproduced with permission. [114] Copyright 2020, American Chemical Society.

this region corresponds to flip-flopping of H1 and the chain connecting H2. Normally oriented towards the membrane, this region can rotate to face up when flexible, most likely to enhace the exposure of H3 to the membrane (see Figure 3.11b ENTH (w/o H0)/PC/PIP2 and Figure 3.13). We posit that these changes come about in order to maximize exposure of hydrophobic residues to the membrane.

The second dynamic region identified in the protein (residues 100 to 120) aligns with a loop bridging helices H6 and H7. As this regions points towards the membrane, when left flexible, it retreats in order for the protein to flatten more effectively upon binding. Indeed, both the dynamic regions identified are oriented towards the membrane and hence are most likely to undergo a certain amount of deformation when the protein adapts to curvature. There is also a slight increase in RMSD around H3 which can be explained by its hydrophobic interactions with the membrane .

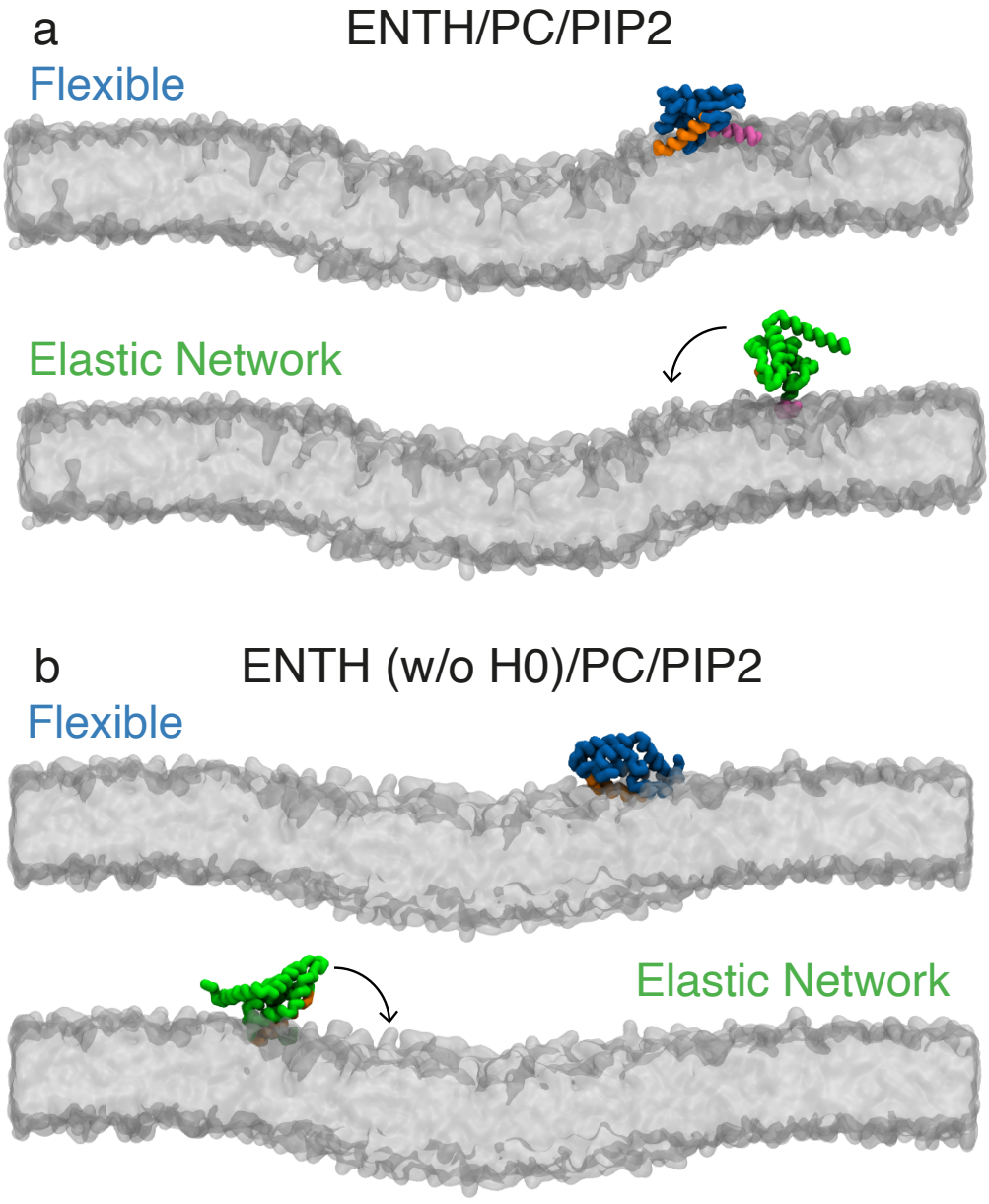

Figure 3.9: Representative snapshots of flexible and elastic network proteins interacting with curvature for (a) ENTH/PC/PIP2 and (b) ENTH (w/o H0)/PC/PIP2 case. Black arrows have been added to show the elastic network proteins strong orientation away from curvature. Reproduced with permission. [114] Copyright 2020, American Chemical Society.

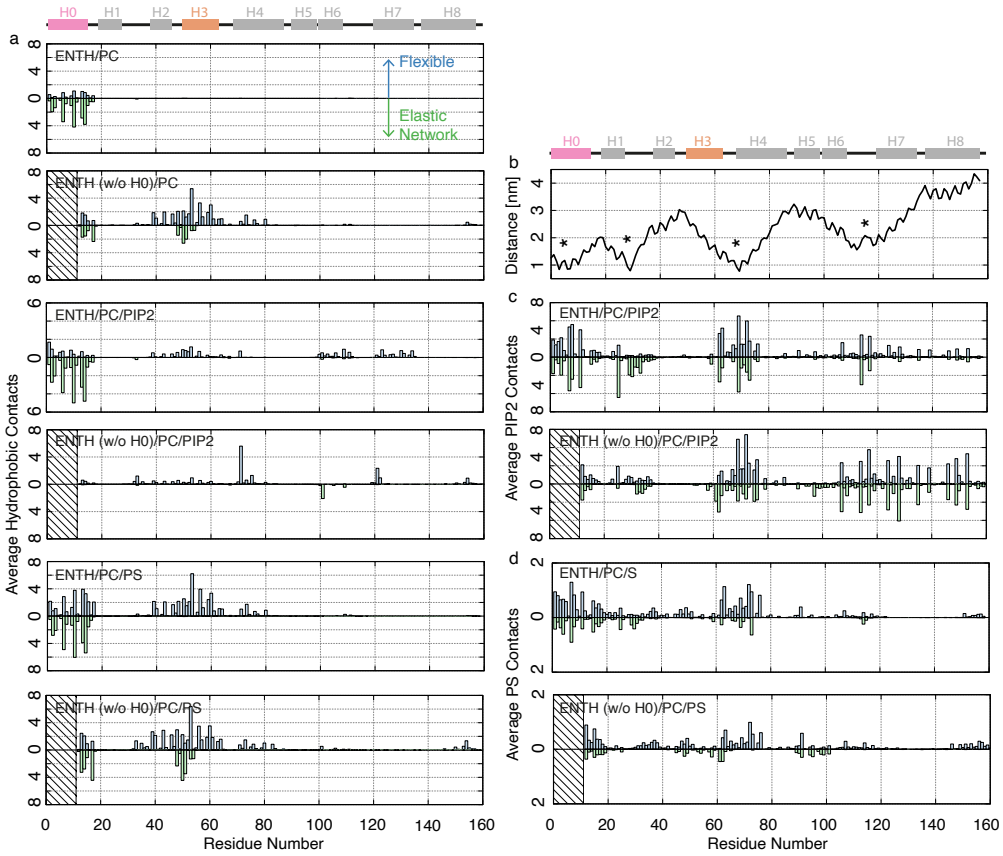

Figure 3.10: Contact analysis of all residues (0 to 160) of the ENTH domain on each simulated case on flat membranes of different composition. (a) Average hydrophobic contacts per residue, (b) distance from PIP2 headgroup to each residue in ENTH domain, (c) average PIP2 headgroup contacts and (d) average PS headgroup contacts per residue. Reproduced with permission. [114] Copyright 2020, American Chemical Society.

Despite the fluctuations in structure when left flexible, a relatively close overlap can be seen between the elastic and flexible structures in the Figure 3.11b snapshots. The backbone RMSD differences (calculated from residue 35 to 160) are approximately 0.5 nm which is relatively small for such dynamic systems. Overall, the flexible simulations are not denaturing as a whole and retain stable structural regions (residues 35 to 100 and residues 120 to 160). Furthermore, the curvature sensing data in Figure 3.5 and the PIP2-binding data in Figure 3.7 suggest that the observed function of the flexible domains is consistent with elastic-network structures. The flexible cases can even replicate observed experimental curvature sensing behaviour which elastic network simulations cannot (see Figure 3.5e and f).

Finally, the location of H0, H3 and the PIP2 binding site of the ENTH domain are shown

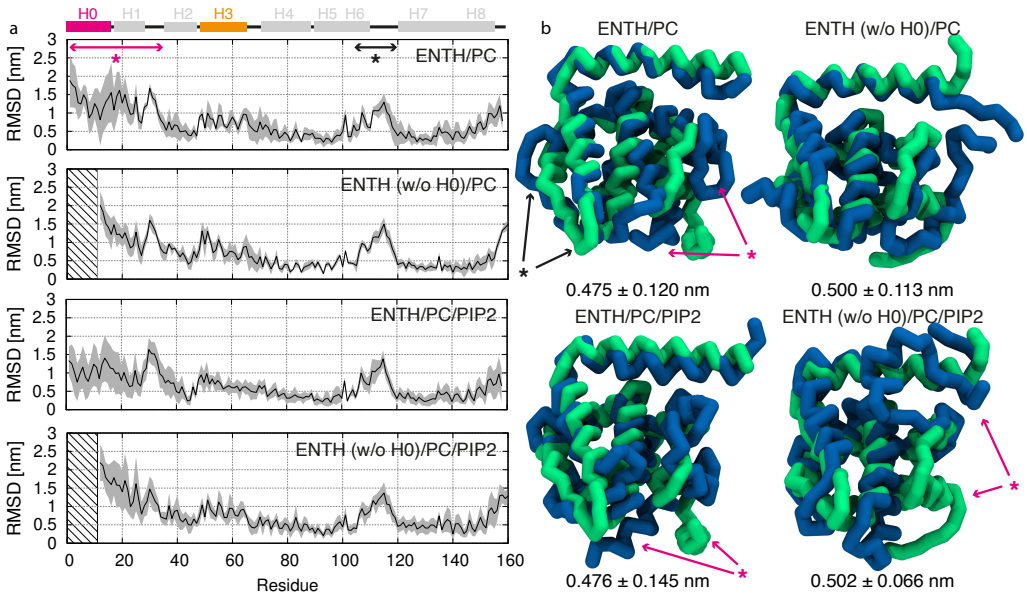

Figure 3.11: (a) Root Mean Squared Deviations (RMSD) between flexible and elastic network ENTH domains as a function of protein residues. (b) Representative snapshots of the structures of the flexible (blue) and elastic network (green) ENTH domains with asterisks highlighting flexible regions of the protein along with the backbone RMSD difference between each structure (calculated from residues 35 to 160). Reproduced with permission. [114] Copyright 2020, American Chemical Society.

in Figure 4.11a. These structures reinforce the idea that H3 may play a role in curvature sensing of the ENTH domain. Indeed, without H0, H3 is both near and pointing towards the membrane. When flexible, H3 can expose more hydrophobic residues to sense membrane curvature. When rigid, only the elbow region of H3 can interact hydrophobically with membrane curvature (see Figure 3.8). Without H0, the ENTH domain has ample space to adapt to curvature, flattening and allowing for further hydrophobic interactions.

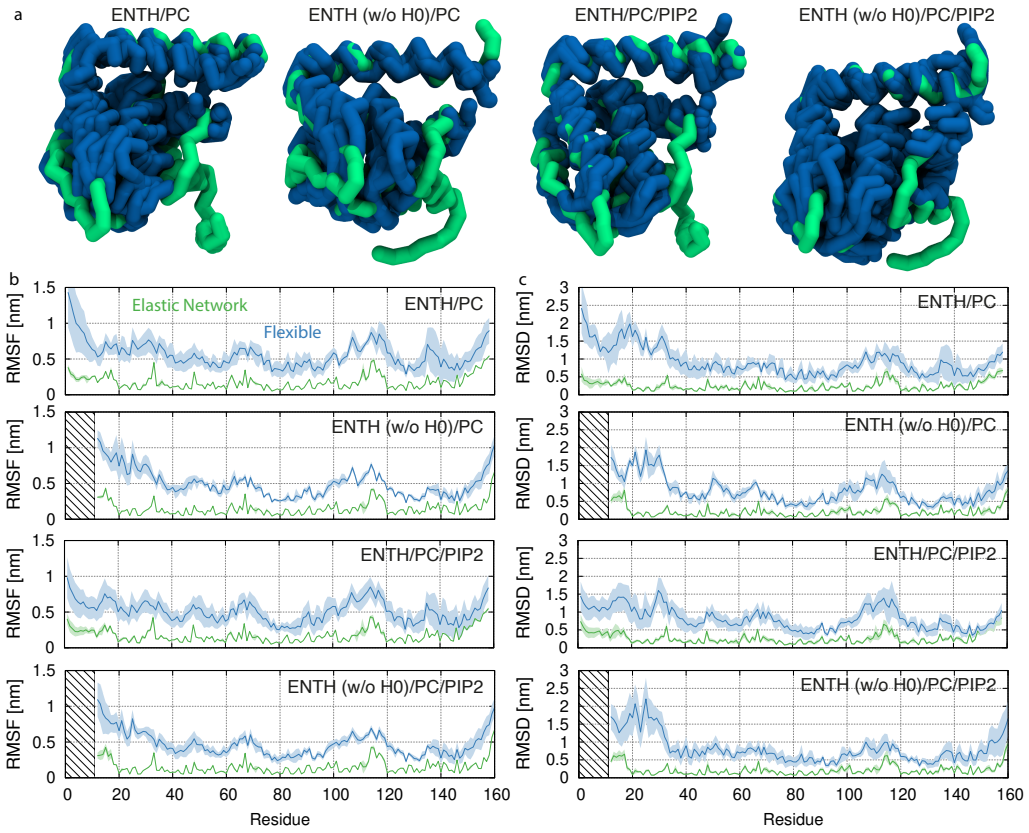

Figure 3.12: (a) Backbone snapshots of the average structures of 8 simulations of the flexible ENTH domain (blue) and a single averaged elastic network ENTH domain (green). Note that the first 35 residues of the flexible domains are not represented in the snapshots for clarity. (b) Root Mean Squared Fluctuations (RMSF) and (c) Root Mean Squared Deviations (RMSD) of protein residues of the ENTH domains. Reproduced with permission. [114] Copyright 2020, American Chemical Society.

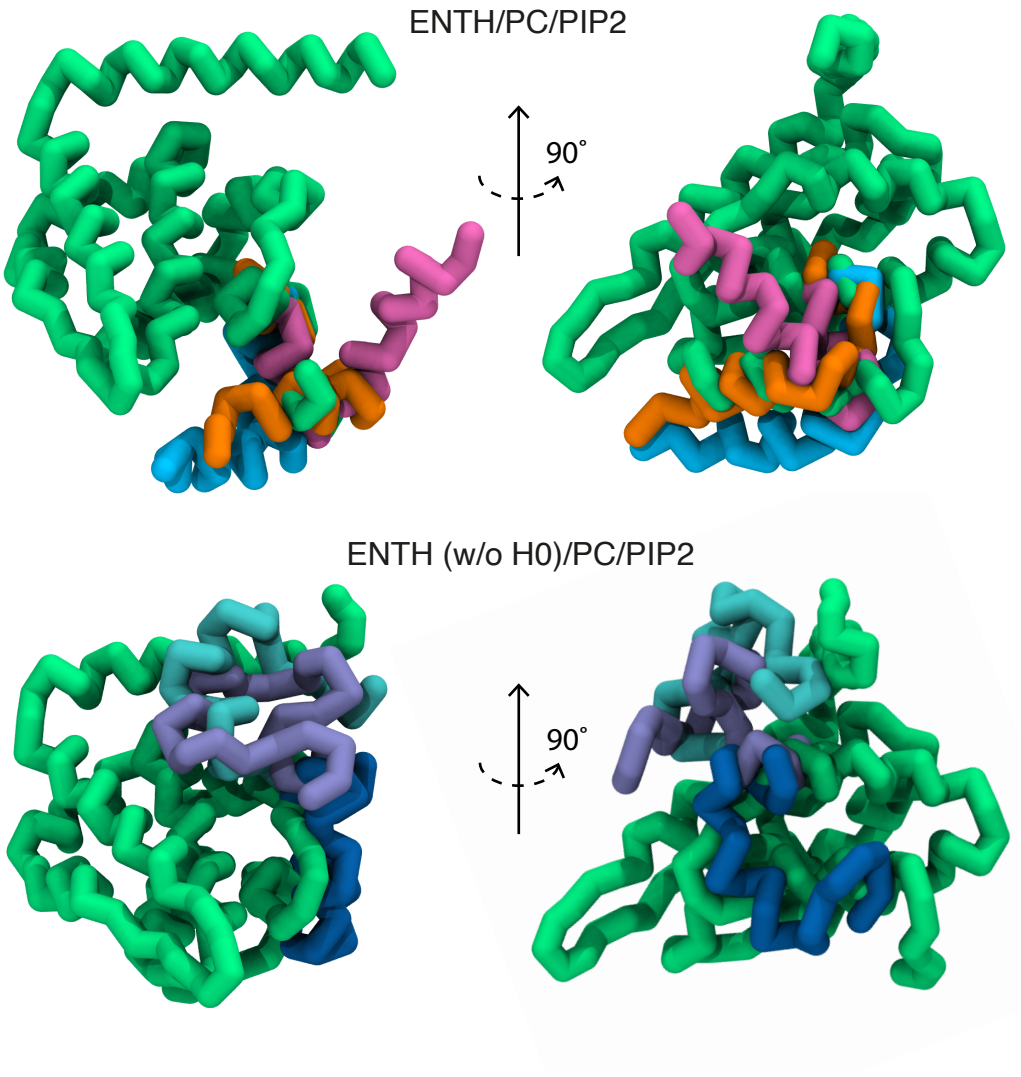

Figure 3.13: Snapshots of the ENTH domain showing flexibility of its N-terminal region (residues 0 to 35). Shown in green is the average elastic network structure and overlaid are three random snapshots (colored randomly) of the flexible ENTH domains. Reproduced with permission. [114] Copyright 2020, American Chemical Society.

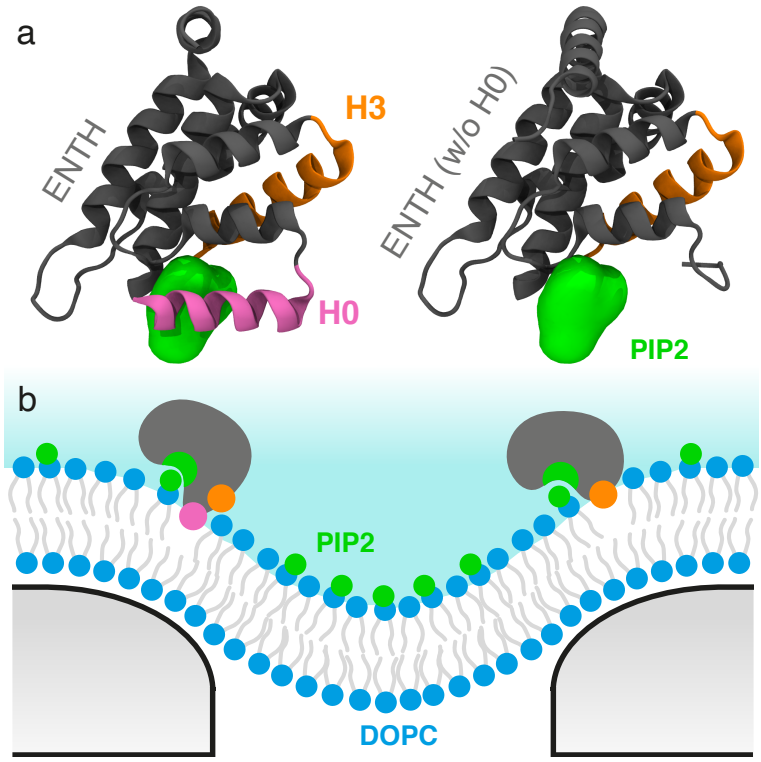

Figure 3.14: (a) Structure of the ENTH domain highlighting helices H0 and H3 in pink and orange respectively and bound PIP2 in green. (b) Schematic overview of the work showing a cartoon ENTH domain sensing curvature both with and without H0. Reproduced with permission. [114] Copyright 2020, American Chemical Society.

3.4 Conclusion & Outlook

This chapter presented a simulation model allowing us to query both structural and functional aspects of the curvature sensing of the ENTH domain. The curvature localization and membrane binding of the proteins was evaluated as well as the effect of backbone flexibility on curvature sensing. Surprisingly, this model suggests that the ENTH domain does not require its H0 helix to localize to membrane curvature. This results reinforces experimental observations of the ENTH domain localizing to curvature without its H0 helix. Instead, the ENTH domain has another helix, H3, which can supplement the domains innate curvature sensing ability. Simulating both with and without an elastic network, these results suggest that flexibility allows for increased hydrophobic exposure and hence better curvature sensing. This modelling approach is unorthodox yet it could be expanded to the study of various other curvature sensing protein systems.

Our model however, is limited in that it focusses on substrate-induced membrane curvature. Further work is needed to understand how proteins assemble and localize spontaneously on free-standing membranes as these could deform dynamically via protein interactions. Furthermore, future work is needed to study membrane curvature at different radii of curvature, with more complex compositions and when exposed to multiple proteins simultaneously. It will also be important in future to further calibrate the MARTINI forcefield against atomistic simulations. In this case, there is strong experimental evidence of membrane curvature activity of the ENTH domain to back-up the simulated protein behaviour. [109, 239, 252]

Overall, the results in this chapter allow us to think more broadly about the role of amphipathic helices in curvature sensing by proteins. The ENTH domain is arguably the first protein to be discovered to have curvature generating function due to the action of its amphipathic helix H0 and has since served as a "gold-standard" membrane curvature protein. If the ENTH domain can sense curvature without H0, what other amphipathic helix-containing proteins might also sense curvature without it? This is not to say that amphipathic helices are unimportant as they are critical in the generation of curvature. However, these results point to the overall hydrophobic interactions between such proteins and membrane curvature to be more complex than previously thought. These ideas could be further explored both in experiments and with simulations.

Chapter 4

Membrane Curvature Binding and Localization of the ANTH Domain

Expanding on the work presented in the previous two chapters, this chapter investigates another curvature-active protein, the ANTH domain, and its mechanisms of membrane curvature sensing and PIP2-binding on nanopore-deformed membranes. This chapter is in preparation for publication.

4.1 Introduction

The previous two chapters explored the implementation of a nanoporosity-based membrane curvature model and its application to studying the membrane binding and curvature sensing of a key curvature protein, the ENTH domain. Following on from this work, this modelling framework was applied to study another PIP2-binding, curvature-active protein domain, the AP180 N-terminal homology (ANTH) domain.

Clathrin-assembly lymphoid myeloid leukaemia (CALM) protein and its neuronal homolog AP180 contain clathrin and adaptor protein 2 (AP2) binding sites towards its C-terminus as well as an AP180 N-terminal homology (ANTH) domain which binds phosphatidylinositol 4,5-bisphosphate (PIP2) at its N-terminus. [108] As part of CALM, the ANTH domain binds PIP2 lipids in the cell membrane and mediates the assembly and disassembly of the clathrin coat during clathrin-mediated endocytosis (CME). [238, 253–256] The ANTH domain is also found in Sla2, a protein which is thought to mediate membrane-actin coupling. [90, 257] In addition, CALM is one of many proteins recruited early on during CME and plays a role in stabilizing membrane curvature during its progression. [89, 258] Knockdown of CALM or AP180 has been shown to disrupt endocytosis,

[259] and synaptic vesicles respectively. [260]

Recently, Miller *et al* have shown that the CALM ANTH domain contains a terminal amphipathic helix (AH) that can induce membrane curvature and modulate the rate of endocytosis in cells. [261] Such terminal amphipathic helices are thought to act as "wedges" which insert into the membrane and drive membrane curvature. [77, 262, 263] A key example of such a helix is found in the epsin N-terminal homology (ENTH) domain, another critical protein recruited early on during CME, which was explored in the previous chapter. [109] Epsin is required to reconstitute clathrin-coated vesicles in vitro due to the curvature action of its AH and is critical for membrane fission. [264–266] Recently, new research has begun to show the ability of these ENTH and ANTH domains to interact together and form complexes. [257, 267–269] As such, these protein domains and their terminal amphipathic helices play an important role in the initiation and progression of CME in cells. However, protein crowding and coupling with intrinsically disordered domains has also been noted as a mechanism for driving membrane curvature. [94, 270–272] It has even been shown that disruption of the key amphipathic helix (H0) in ENTH domains still allows for curvature generation due to crowding. [273] In addition, the research in the previous chapter has suggested that the ENTH domain can sense membrane curvature even without its terminal AH in the presence of PIP2. [114] This contrasting evidence elicits questions regarding the role of AHs in membrane curvature sensing. Furthermore, both the ENTH and ANTH domains bind PIP2 lipids in the membrane but the role of these lipids surrounding curvature is still far from understood. Indeed, what role does PIP2 play with respect to curvature and localization of AH-containing proteins to membrane curvature? Also, how important are AHs in the curvature sensing process?

Following this thesis' previous work on protein-curvature interactions,[114, 159] this chapter explores the behaviour of the ANTH domain and its interaction with membrane curvature. The role of the ANTH's terminal helix was investigated by evaluating the curvature-sensing ability of three crystal structures of the domain as proposed by Miller *et al*. [261] Figure 4.1a shows the crystal structure of the ANTH domain with three differing terminal helices, a short helix truncated at a1 (shown in blue), a split helix with an unstructured region separating a1 from a0 (shown in light pink), and a full helix with both a1 and a0 intact (shown in purple). In addition, the effect of PIP2 on the ANTH domain's curvature sensing behaviour was investigated by studying two membrane compositions, a neutral 100% phosphatidylcholine (PC) membrane and a negatively charged membrane containing 97.5% PC and 2.5% PIP2 (see Figure 4.1b). Figure 4.1c shows snapshots of the simulation system showing a membrane interfaced with a nanoporous wafer as well as a slice through the membrane highlighting its curvature. Table 4.1 presents a summary of

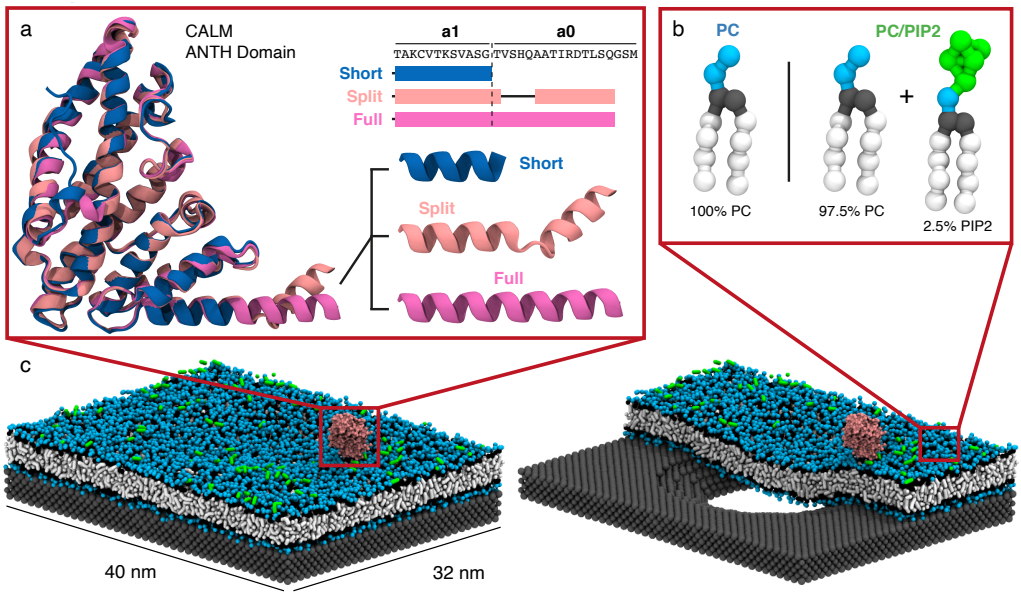

Figure 4.1: Schematic of the systems studied in this work showing (a) overlapped crystal structures of the CALM ANTH domain with the three terminal helices, denoted as: short (PDB code: 1HFA.pdb), split (PDB code: 3ZYM.pdb) and full (PDB code: 3ZYL.pdb), studied in this work along with the amino acid sequence for this region. Note that each structure is missing the first three residues of a0. (b) Snapshots of the lipids used in the two membrane compositions studied for this work, 100% PC (PC) and 97.5% PC + 2.5% PIP2 (PC/PIP2). White beads represent hydrophobic groups, gray beads represent carboxy groups, blue beads represent the headgroups of PC lipids and green beads represent the headgroups of PIP2 lipids. (c) Snapshots of the simulation system showing the membrane as well as a slice-through highlighting curvature as well as a protein to-scale in red.

the simulations performed in this study.

Table 4.1: Summary of the simulations systems investigated in this work (*N denotes the number of independent simulations run. ** 97.5% PC and 2.5% PIP2)

Simulation ID	Protein	Membrane	N*	Duration (μs)
Short/PC	ANTH	PC	8	10
Split/PC	ANTH	PC	8	10
Full/PC	ANTH	PC	8	10
Short/PC/PIP2	ANTH	PC/PIP2**	8	10
Split/PC/PIP2	ANTH	PC/PIP2	8	10
Full/PC/PIP2	ANTH	PC/PIP2	8	10

4.2 Methods

4.2.1 Simulation Details

All simulations were performed using Gromacs 2018.3. [215] Protein simulations were performed at 323 K using the Martini 2 force-field with explicit water. [52] The temperature was coupled to a velocity rescale thermostat using a time constant of 1 ps with the protein, membrane, wafer, solvent and ions each being coupled independently. The protein crystal structures were from the RCSB protein data base: ANTH short helix, (Protein Data Bank (PDB) code: 1HFA.pdb), ANTH with split helix (PDB code: 3ZYM.pdb) and ANTH with full helix (PDB code: 3ZYL.pdb). Proteins were coarse-grained using the martinize.py script from cgmartini.nl and an elastic network was added, where noted, using a force constant of 500 kJ/mol and a cut-off distance of 0.9 nm. The systems were equilibrated for 20 ns using a 0.02 ps time step and a semi-isotropic Berendsen barostat using a time constant of 1 ps. For production runs, a 0.03 ps time step was used with the Parrinello-Rahman barostat was used and a 12 ps time constant. The protein center-of-mass was computed using the gmx traj tool and contacts analysis was performed using the gmx mindist tool, both in Gromacs. [215]The velocity rescaling thermostat was used throughout.

4.2.2 Trajectory Analysis

All snapshots were taken using VMD. [216] The heatmaps and radial distribution histograms were computed from the protein center-of-mass (CoM) data extracted from the simulations using the $gmxtraj$ tool mentioned above. Heatmaps in Figure 4.3 were created by converting the x-y CoM data into absolute distances from the central pore (x=16 and y=20). This data was then mapped onto a 50 by 50 grid of equally spaced bins (x limits = 0-20 nm and y limits = 0-25 nm). The histograms from which the fold change is calculated were determined by converting the x-y CoM data into radial distance from the central pore. This radial data was then converted into a histogram over 100 equally spaced bins between 0 and 25 nm. In addition, kernel density estimates of the raw radial data was computed using $stats.gaussian_kde$command from the python scipy package. Both the x-y histograms and radial histograms were normalized so that the sum over each bin in the histogram equals to 1.

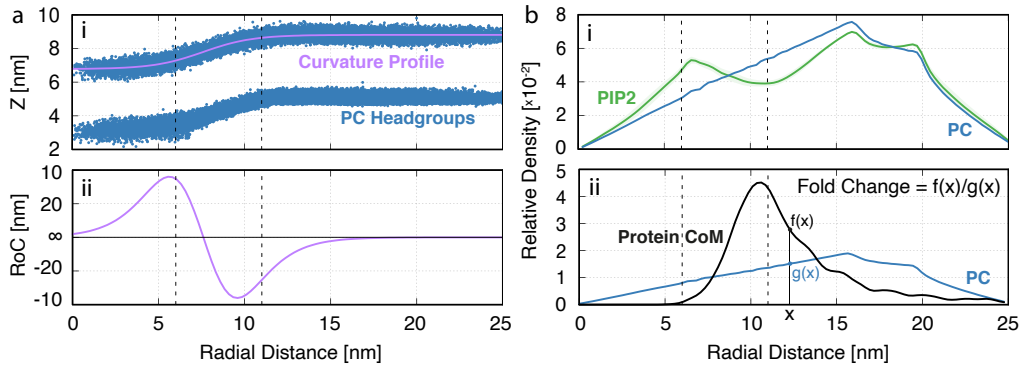

Figure 4.2: (a) (i) Average vertical position of PC lipid headgroups and membrane curvature profile as a function of radial distance from central pore and (ii) curvature values of curvature profile as a function of radial distance. (b) (i) Average kernel densities of PC and PIP2 lipids as a function of radial distance and (ii) an example for how the fold change of protein localization is computed in this study. Note the dashed lines represent the start and end of the tapered region of the underlying wafer which approximates to the membrane curvature region.

4.3 Results & Discussion

4.3.1 Characterisation of Membrane Curvature

The curvature profile of the membrane system can be seen clearly in Figure 6.2ai. The PC lipid headgroups are fitted to a sigmoidal function to get an estimate of the radius-of-curvature (inverse of curvature) for the membrane (Figure 6.2aii). In addition, due to the fixed curvature in the system, PIP2 enrichment and depletion is observed at concave (at approx. 6 nm) and convex (at approx. 11 nm) regions of the membrane respectively (Figure 6.2bi). PIP2's preference for concave curvature regions has previously been observed computationally by Koldsø et al. [84] In order to evaluate protein curvature sensing, the fold change in radial position with respect to the underlying lipid density is tracked, shown schematically in Figure 6.2bii.

4.3.2 Protein Localization

Examining the protein localization results in Figure 4.3, consistent curvature sensitivity for all ANTH domains is observed when interacting with 100% PC membranes (corresponding to peaks at approximately 11 nm in Figure 4.3b). This is surprising as, without a fully-fledged AH, we would expect both the Short (Figures 4.3ai and 4.3bi) and Split (Figures 4.3aiii and 4.3biii) ANTH domains to not be curvature active. These results suggest that the ANTH domain has some innate curvature sensitivity irrespective of the presence or structure of its AH. When PIP2 is added to the membrane, however, only the Full ANTH

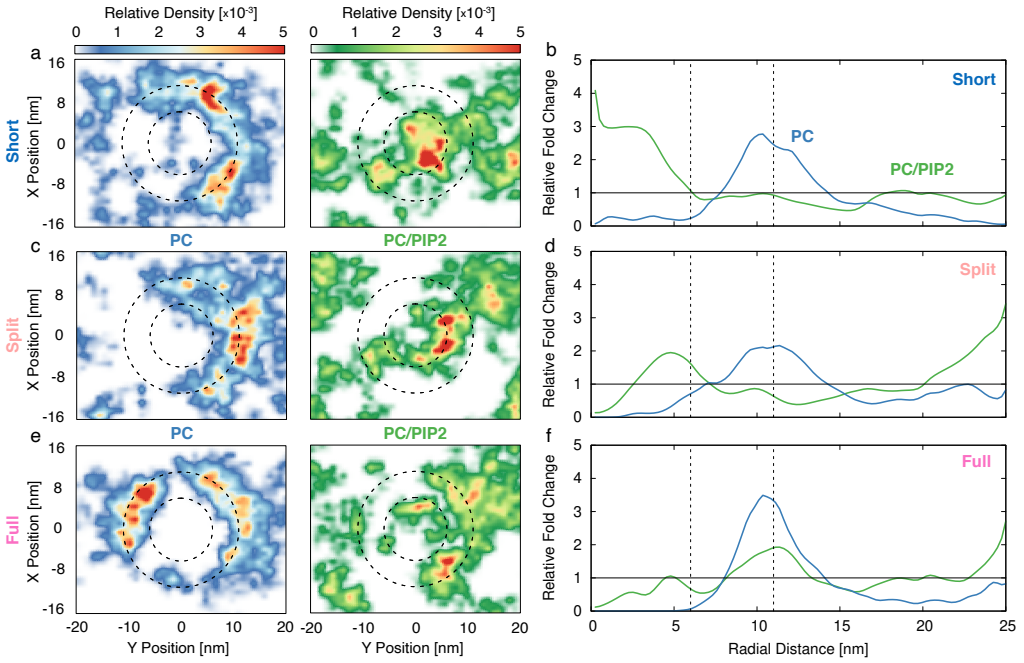

Figure 4.3: (a) Statistical frequency heatmaps showing center of mass positions of the (i) Short, (ii) Split and (iii) Full ANTH domains respectively on 100% PC and 2.5% PIP2 membrane. (b) relative fold change of (i) Short, (ii) Split and (iii) Full ANTH domains respectively as a function of radial distance from central pore normalized with respect to lipid density. Note the dashed lines represent the start and end of the tapered region of the underlying wafer which approximates to the membrane curvature region.

domain retains its curvature sensing ability (Figures 4.3aiii and 4.3biii). This coincides closely with the experimental work performed by Miller et al. which suggests that only the full helix ANTH domain is curvature active. [261] The raw protein localization results are shown in Figure 4.4 from which the relative fold-change in Figures 4.3b are calculated.

4.3.3 Hydrophobic Binding

To understand the origin of the curvature sensing of the ANTH domain, the binding behaviour of the proteins to both PC and PC/PIP2 membranes was examined. In particular, the hydrophobic interactions between the protein and the hydrophobic tails of the lipid molecules in the membrane were analysed. Figure 4.5a shows the average hydrophobic contacts between each ANTH domain interacting with 100% PC and 2.5% PIP2 membranes. For the short and full ANTH domains (Figures 4.5ai and 4.5aiii), we see strong hydrophobic activity of two residues (Y44 and M52) on the third helix of the protein, denoted as a3. These residues can be seen on the structure of the ANTH domain in Figure 4.5b. The full ANTH domain (Figure 4.5aiii) also shows consistent hydrophobic activity

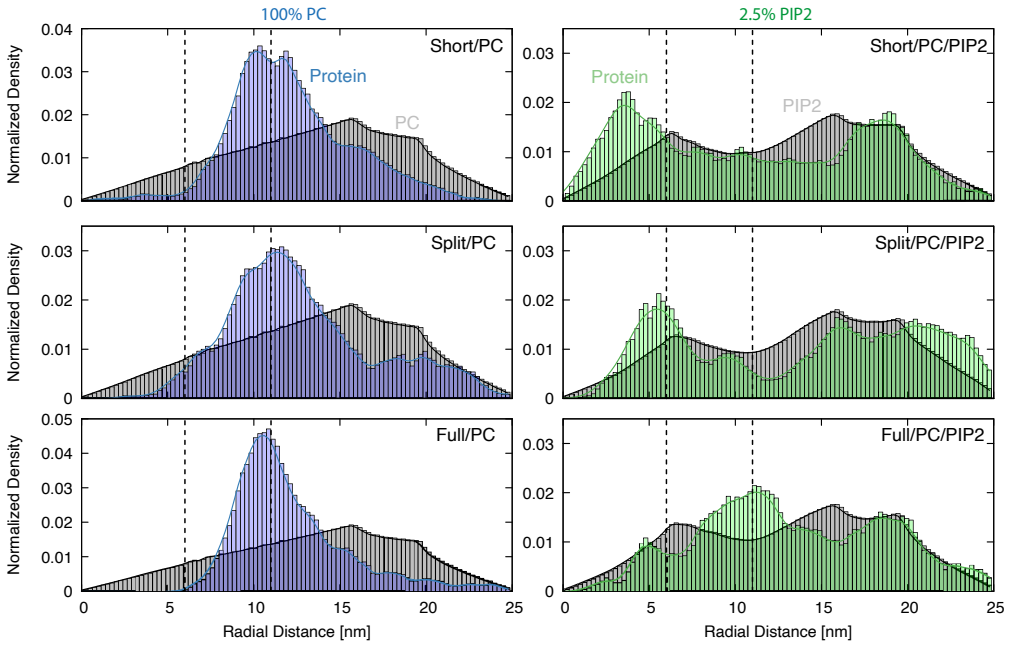

Figure 4.4: Protein and lipid density profiles normalized over 100 bins used to calculate fold change in ANTH domain localization behavior in Figure 3 of the main manuscript. Each histogram was normalized to the total number of counts recorded for each simulation case. Note that the scalloped features at 16 nm and 20 nm are artefacts due to the rectangular simulation cell.

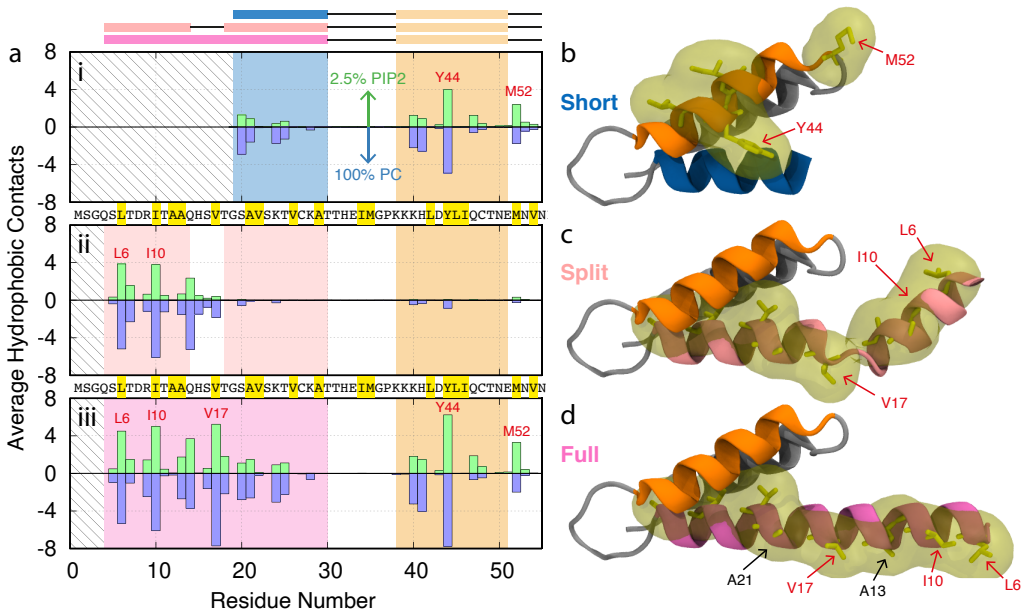

Figure 4.5: (a) Membrane binding analysis showing sequence and average hydrophobic contacts for (i) short, (ii) split and (iii) full ANTH domain on 100% PC and 2.5% PIP2 membranes for first 55 residues. Residue codes in yellow highlight correspond to hydrophobic residues (L, I, A, V, M, Y). The rectangles above represent alpha helices in the structure. Residues L6, I10, V17, Y44 and M52 are marked in red text as they are the key hydrophobic residues in this region. (b), (c) and (d) structures of first 55 residues of the short, split and full ANTH domains respectively with hydrophobic residues and corresponding hydrophobic surface highlighted in yellow.

along a0 and a1, with strong contacts at L6, I10 and V17, again corresponding very well with experimental work by Miller *et al* who identified these as the key curvature-active residues of the ANTH domain. [261] These three residues are highlighted and labelled in red on the structures in Figures 4.5c and d. The split domain, however, only shows strong activity at L6 and I10 (Figure 4.5aii). This binding information confirms that the ANTH domain's curvature activity can be assigned to its AH. However, it also presents findings on how this protein interacts with curvature, with the hydrophobic activity of a3 being of interest. The hydrophobic binding information for all residues of the protein can be seen in Figure 4.7a.

4.3.4 PIP2 Binding

After considering hydrophobic interactions, the contacts between negatively charged PIP2 headgroups and the proteins were examined. Figure 4.6a shows very consistent PIP2 binding across each case. Indeed, the key positive residues K24, K28 and K38 are actively interacting with PIP2 for each protein. These are highlighted in the structures in Figures

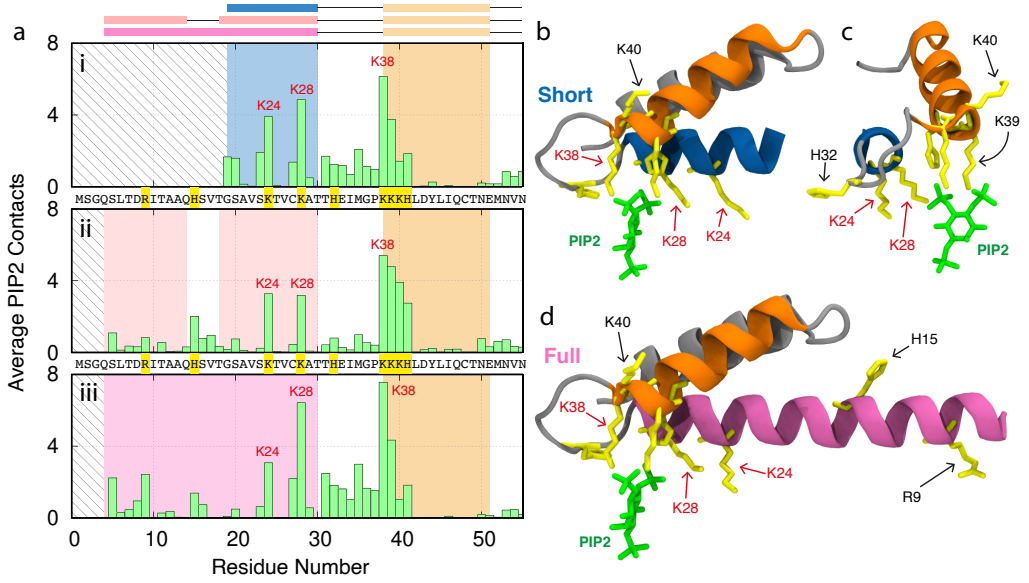

Figure 4.6: (a) Membrane binding analysis showing sequence and average PIP2 headgroup contacts for (i) short, (ii) split and (iii) full ANTH domain on 100% PC and 2.5% PIP2 membranes for first 55 residues. Residue codes in yellow highlight correspond to positively charged residues (K, H, R). The rectangles above represent alpha helices in the structure. Residues K24, K28 and K38 are marked in red text as they are key PIP2-binding residues in this region. (b), (c) Structure of first 55 residues of the short ANTH domain from the side and looking down a1, with PIP2 highlighted in green and positively charged residues highlighted in yellow. (d) Structure of first 55 residues of the short ANTH domain from the side.

4.6b, c and d. This shows us that modifying the terminal helix of the ANTH domain does not affect PIP2 binding.

Figure 4.7b shows the PIP2 binding for all residues of the ANTH domain. Interestingly, significant binding around residue 150 is observed. This can be explained by the ANTH domain tilting to maximize PIP2 contacts with other positively charged residues. Indeed, looking at the orientation of the ANTH domains on PC and PC/PIP2 membranes in Figures 4.8 and 4.9 respectively, a clear orientation of the protein towards the membrane in the presence of PIP2 can be seen, especially for the Short and Split cases. This was observed in a more quantitative fashion using rotation matrix calculations (using the $rotmat$ tool in GROMACS). We see a clear shift towards the membrane is noted when PIP2 is added (Figure 4.10). Note that a value of 1 or -1 in the Z rotation calculations suggests that the protein is more oriented or inversely oriented along the vector of the simulations cell z-axis respectively.

Despite each protein having an identical PIP2-binding site and interacting the same way

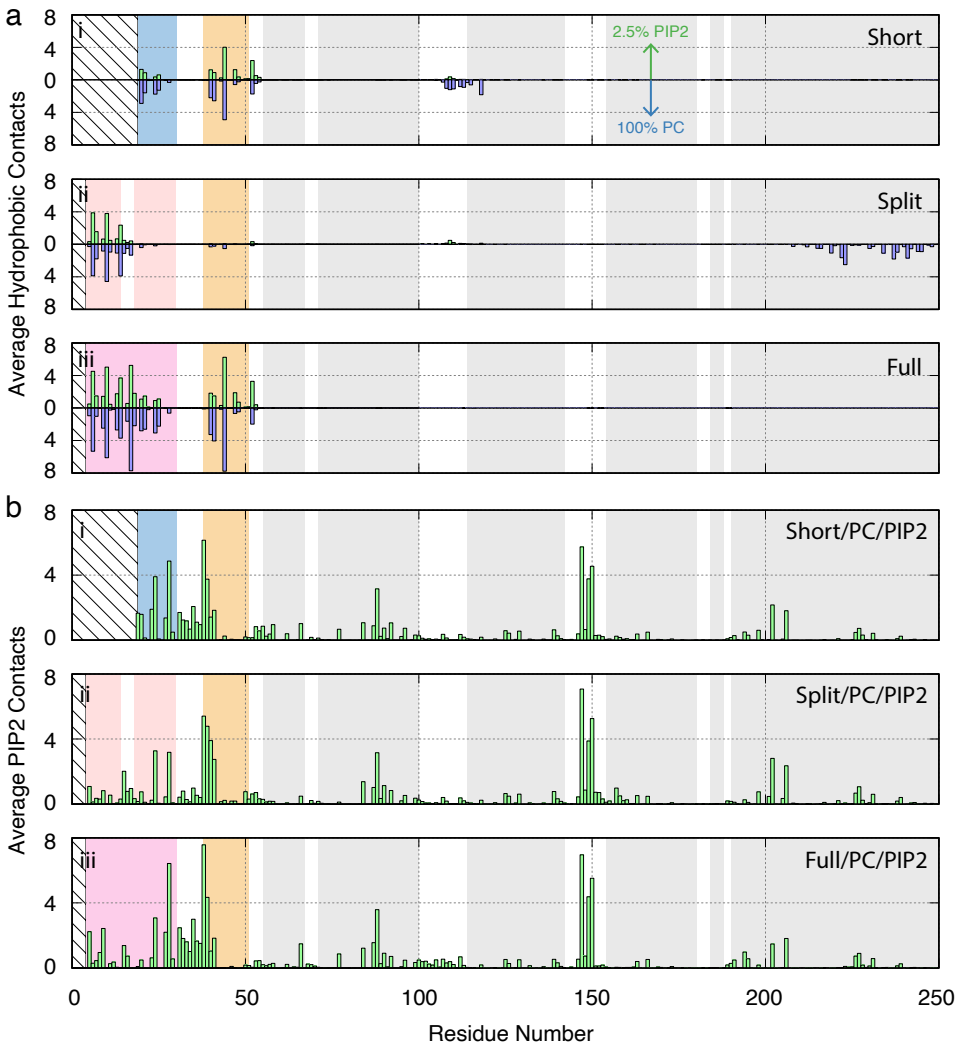

Figure 4.7: (a) Hydrophobic binding showing contacts for (i) Short, (ii) Split and (iii) Full cases on both PC and PC/PIP2 membranes. (b) PIP2 binding of all cases in this work showing contacts for (i) Short/PC/PIP2, (ii) Split/PC/PIP2 and (iii) Full/PC/PIP2 cases.

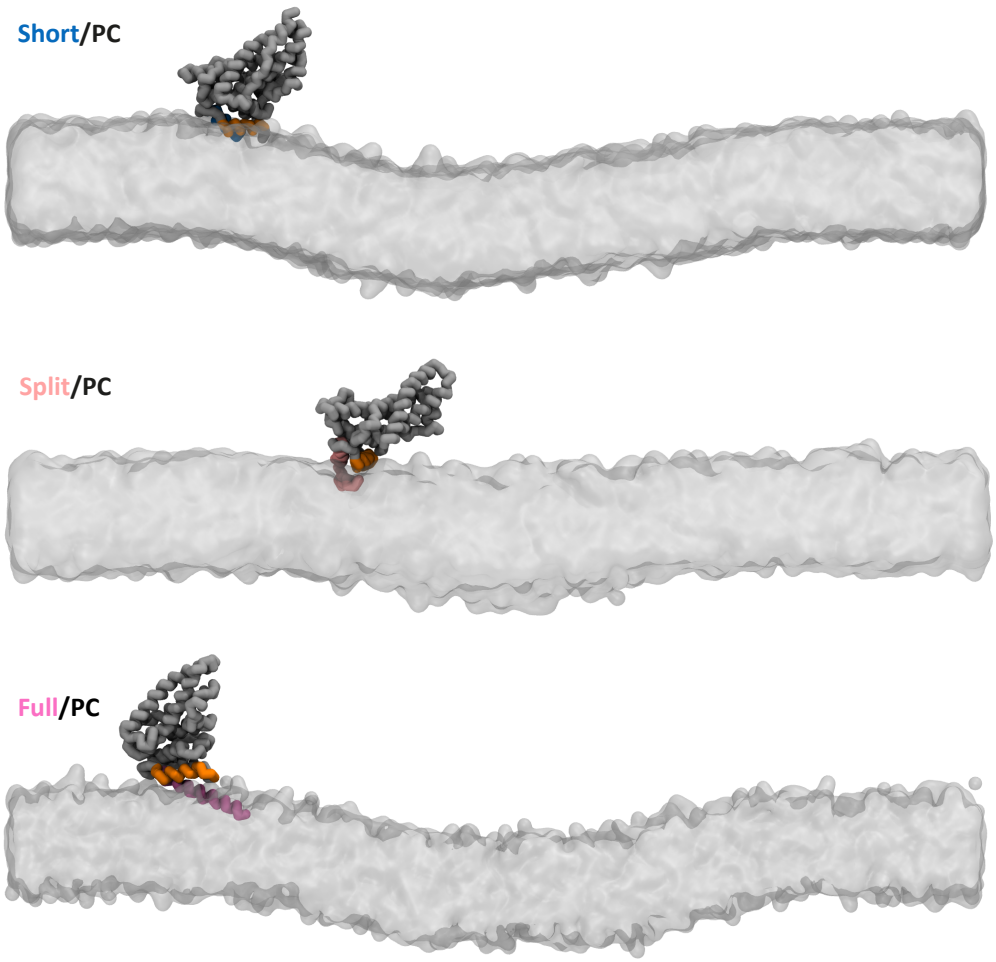

Figure 4.8: Snapshots of the ANTH domain interacting with PC-only membranes.

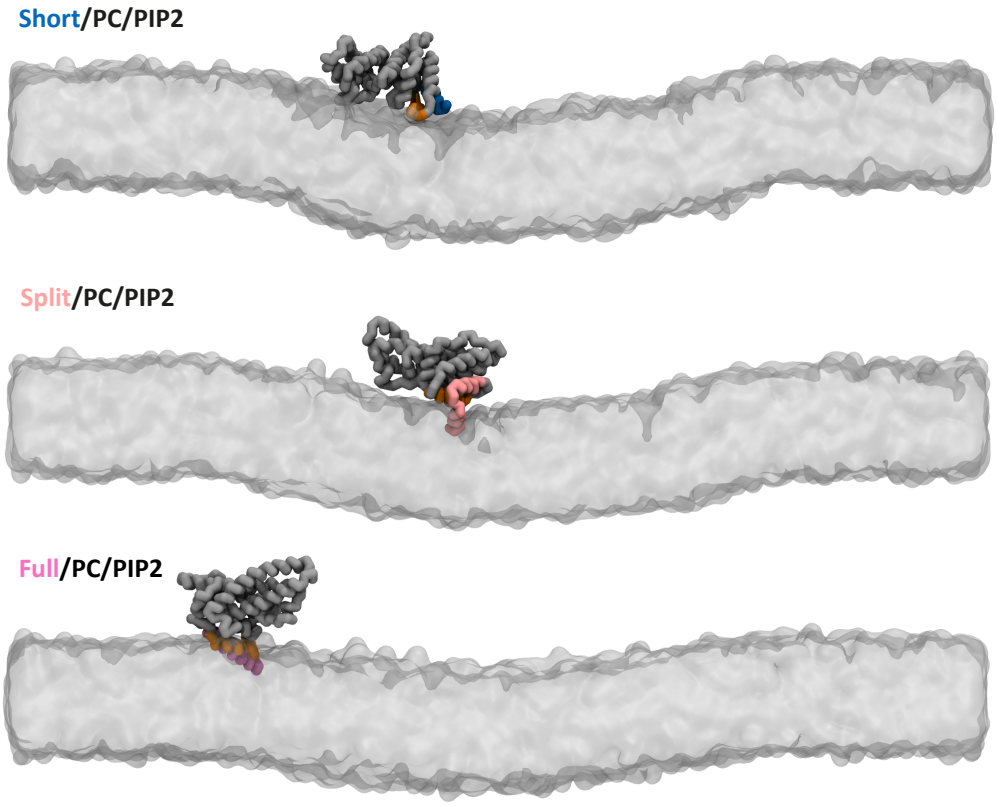

Figure 4.9: Snapshots of the ANTH domain interacting with PIP2-only membranes.

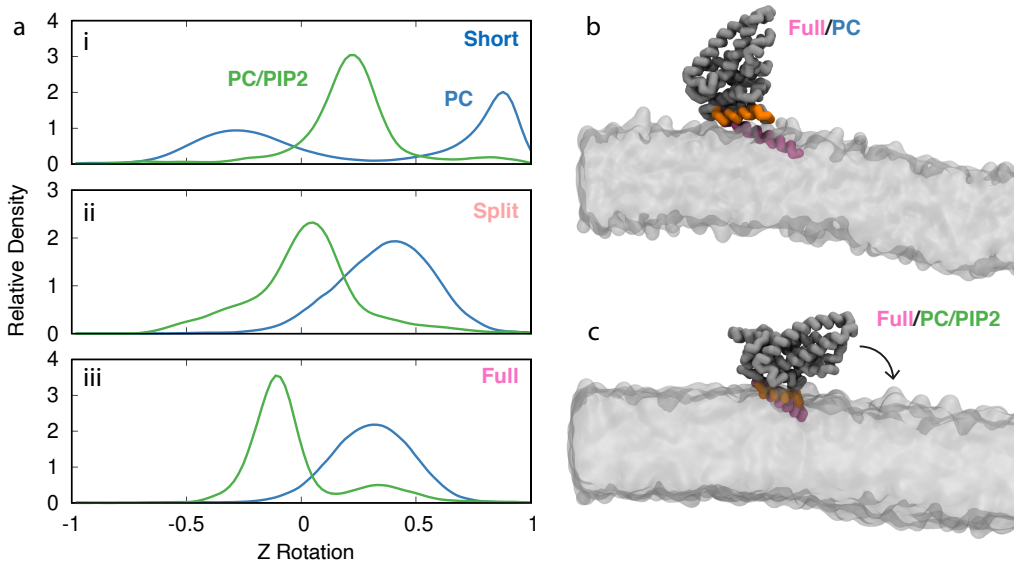

Figure 4.10: (a) Relative density of z component rotation matrix compared to initial state for (i) Short, (ii) Split and (iii) Full helix cases on both PC and PC/PIP2 membranes. (b) and (c) show snapshots of the Full CALM ANTH domain interacting with a PC and PC/PIP2 membrane respectively showing a noted tilt of the protein orientation once bound in the PIP2-containing case.

with PIP2, the presence of PIP2 strongly affects the proteins ability to sense curvature. This behaviour can be explained by thinking about the opposing forces, PIP2 and hydrophobic, acting upon the protein of interest and how these affect its localization. The contributions from PIP2 are equal for each crystal structure of the ANTH domain studied here as it was shown that binding is identical (Figure 4.6). On the other hand, the hydrophobic contributions for each helix structure are different with the Full helix showing 5 active hydrophobic residues and the Split and Short helices showing only 2 each (Figure 4.5). As such, we suggest that the hydrophobic contributions for the Short and Split helices are lower than PIP2 attraction leading to a removal of curvature sensing in Short/PC/PIP2 (Figure 4.3ai and bi) and Split/PC/PIP2 cases (Figure 4.3aii and bii). The Full helix however, has a strong enough hydrophobic contribution that it can overcome the opposing PIP2 attraction allowing it to still sense curvature (Figure 4.3aiii and biii). This logic is represented schematically in Figure 4.11. Figure 4.11a shows a schematic of the idealized free energy surfaces from PIP2 and hydrophobicity along the curvature model while Figure 4.11b shows the relative contributions of each opposing forces for each the Full, Split and Short helix.

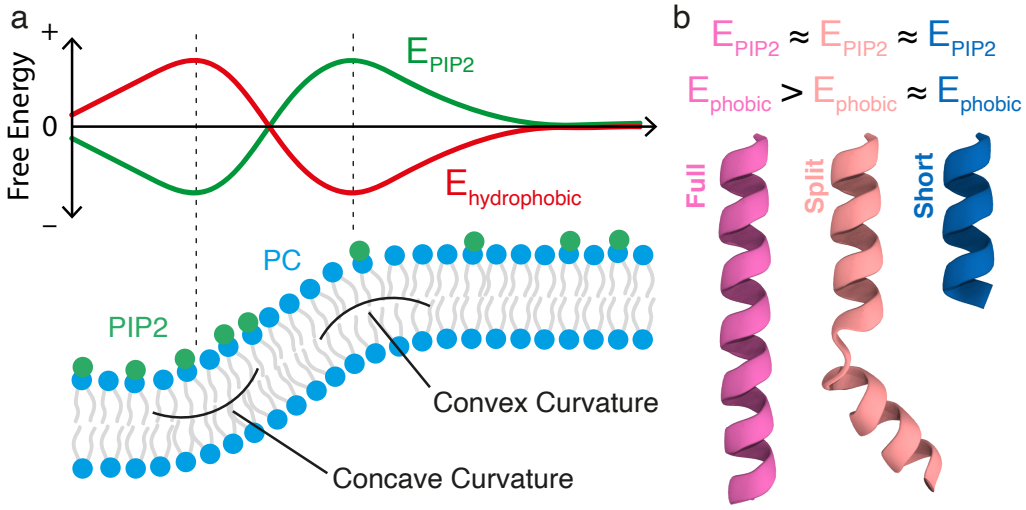

Figure 4.11: (a) Schematic of free energy profiles of PIP2 and hydrophobicity as a function of the membrane profile highlighting concave (∪) and convex (∩) regions of curvature. (b) Comparison of PIP2 and hydrophobic free energy contributions for Full, Split and Short helices of the ANTH domain along with their crystal structures highlighting that the pip2 attraction of the protein to the membrane is the same for all cases but the hydrophobic contribution of the full helix preferring convex curvature is larger than the split and short helices.

4.4 Conclusion & Outlook

In conclusion, the membrane curvature activity of the ANTH domain with three different helix structures was studied under PC-only and PIP2-containing membrane conditions. It was shown that on PC-only membranes, the ANTH domain exhibits curvature sensing behaviour irrespective of the structure of its terminal helix. This is surprising as we expect this helix to be the main driver behind curvature sensing of the ANTH domain. This can be explained by the activity of two hydrophobic residues on helix a3, Y44 and M52, at the membrane-exposed surface of the protein. On PIP2-containing membranes, only the ANTH domain with Full helix can sense curvature, while the others localize to PIP2 dense regions. This can be explained by the combined activity of hydrophobic residues on both helices a0 and a3. The hydrophobic binding analysis for a0 ratified experimental results suggesting that residues L6, I10 and V17 are the key curvature active residues on this helix. The short and full cases, on the other hand, have less overall hydrophobic residues exposed and as such do not sense membrane curvature. Finally, it was shown that all three protein structures bind PIP2 in the same manner (matching experimental work by Miller *et al*). [261]

Overall, this work shed light on the complex interaction between PIP2-binding proteins and curvature. In essence, this suggests there is a balance of opposite forces due to the PIP2 localization away from regions of convex curvature to the central and flat regions of the membrane. While each of the proteins studied in this work bind PIP2 in the same manner, the Full helix engages more hydrophobic residues than the Short and Split helices. As such, the hydrophobic attraction of the Full helix allows it to still sense curvature even in the presence of PIP2. We can extrapolate this result to suggest a more generalized mechanism for curvature sensing proteins during endocytosis. Due to the local enrichment of PIP2 during endocytosis, we can imagine that most of these lipids will localize around the forming bud, at concave curvature. Hence, curvature active proteins must be able to balance their hydrophobic and PIP2 attractions in order to bind PIP2 at endocytic pits and still localize to curvature in order to drive the CME process.

Chapter 5

Characterisation of Biologically Relevant Surfaces via XPS

This chapter describes the application of X-ray photoelectron spectroscopy (XPS) for the characterization of material surfaces for biological applications. Two materials systems in particular are characterized in this chapter. Firstly, silicon nanoneedles and their surface chemistry are investigated for their use in bio-interfacial applications. Following this, the surface of gold nanoclusters is studied to further understand catalytic reactions required for applications in disease biosensing.

5.1 Introduction

The previous chapters presented the application of coarse-grained simulations to study the interface between nanomaterial surfaces and cell membranes. Chapter 2 in particular explored how nanoporous surfaces could induce membrane curvature and potentially stimulate biological processes in cells by initiating protein aggregation at regions of curvature. In addition to physical design parameters of nanoporous wafers, the potential chemical attraction of the cell membrane to the surface was shown to strongly influence membrane deformation. Tailoring the adhesion between cells and materials is one of the key aspects for the successful application of materials for biological applications. [274]

While in chapter 2, the interface between a membrane and solid surface was tuned by artificially modifying the interactions between lipids and wafer beads, experimentalists and chemists have developed a number of ways to improve cellular attachment to material surfaces. Indeed, surface modification of materials for cellular interfacing is a rich field of research. Although the design of new chemical modifications for materials is not in the

scope of this thesis, this chapter's aim is to support the development of materials surfaces for cellular applications by employing high resolution characterisation techniques.

Returning to the initial inspiration for the nanoporous wafer design employed throughout this thesis, the material system of choice for the application of XPS are porous silicon nanoneedles. Co-developed in the Stevens Group, these nanostructured materials have recently become of interest in the field of drug delivery and cellular manipulation. Indeed, they have been applied as intracellular sensors and drug delivery vectors with applications both *in vitro* and *in vivo*. [23, 24, 180] In addition to their excellent performance as drug delivery vectors, the promise of these materials stems from their low cellular stress, biocompatibility and biodegradability. The excellent performance of these materials however, relies on precise control over their surface chemistry. As these materials are designed to be directly in contact with cells and even used *in vivo*, their surface chemistry must be very well characterized and understood. Incorrect chemical species and contaminants could not only reduce the performance of these innovative materials but also create severe complications for patients.

In addition to investigating the surface chemistry of silicon nanomaterials, this chapter presents results on the surface characterisation of gold nanoclusters (AuNCs). Exploring these materials for biosensing applications *in vivo*, XPS is used to study chemical changes occurring at the surface of these catalytic nanomaterials. The investigation of chemical reactions at surfaces is a domain of rich computational research and XPS can be used as a useful tool to contribute to our understanding of surface-mediated reactions. As such, this chapter provides an overview of the potential applications of XPS for studying material surfaces.

5.1.1 XPS and Biological Surfaces

The surface sensitivity of XPS has led it to be a go-to technique for the characterisation of surface chemistry in nanotechnology and biology. Since the mid 1970's, XPS has been applied to biological systems, for example studying the surfaces of biomaterials, [275] evaluating the formation of blood clots on artificial substrates *in vivo*,[276] and designing cell culture environments. [277]. The Food and Drug Administration (FDA) often requests XPS data during approval of medical devices. [274] McArthur splits the applications of XPS into three distinct categories. [278] The first describes XPS as a means to characterise the chemistry of biological surfaces and detecting the presence of surface contaminants. Surface chemistry plays a crucial role in biocompatibility and contamination can lead to biofouling or even medical device failure *in vivo*. Secondly, XPS is often used to optimize surface functionality of materials which have been chemically modified. The technique,

despite its relatively low spatial resolution, has been used to map coverage as well as compositional depth profiles of compounds bound to surfaces. [279, 280] Thirdly, XPS has been applied to understanding biological interactions with materials, such as protein and biomolecule adsorption to surfaces immersed in biological fluid. [278] In particular, researchers have used XPS combined with radiolabeling to quantify the extent of protein and DNA adsorption to polymers and surfaces. [281–283] In recent years, the technique has been expanded to the study of micro-organisms such as bacteria and their cell membranes. [284–286]

Despite its rich history of applications in biology and nanotechnology, XPS does have its limitations however. One of the biggest limitations of XPS when applied to biological surfaces is the ultra-high vacuum (UHV) requirements of the technique. Biological surfaces are hydrated and once placed in vacuum and dehydrated, structural changes occur which can belie the "real" surface chemistry in a hydrated state. Some workarounds include analysing frozen samples at low temperatures, [275, 287, 288], adsorbing small amounts of water molecules onto surfaces under UHV, [289] and implementing differential pumping techniques to create thin water vapour layers on samples during analysis as in ambient pressure XPS. [290, 291] This issue is also highly relevant to the study of catalysis materials which are frequently applied in aqueous environments.

Another limitation of XPS for the analysis of adsorbed proteins and biomolecules is the difficulty in resolving different species of similar chemistry. Indeed, most proteins contain similar amounts of carbon, oxygen and nitrogen. Hence, without the presence of an independent chemical species, it is nearly impossible to distinguish individual proteins from one another and even from a biomolecule with similar elemental composition using only XPS. [292] One solution this problem is to radiolabel specific proteins of interest with a radioisotope which can be directly identified with XPS. [292]

In order to account for these limitations, most state-of-the-art surface characterisation laboratories employ XPS as part of a roster of advanced techniques; combining XPS with secondary ion mass spectrometry (SIMS), spanning probe microscopy (SPM), surface plasmon resonance (SPR) and others. [292] These techniques are complementary and allow researchers to gain a fuller picture of their surfaces of interest which XPS on its own cannot provide. The results presented in this chapter will highlight applications where XPS both does and does not provide a full picture of a materials surface.

5.2 Methods

All XPS measurements were performed using a Thermo Fisher K-Alpha spectrophotometer. This equipment employs a monochromatic Al-Kα X-ray source and a 180 double focusing hemispherical analyser with a 2D detector. Using a 400 μm^2 X-ray spot size, survey spectra were recorded with a pass energy of 200 eV, followed by high-resolution measurements for Au 4f, S 2p and C 1s core levels at pass energies of 20 eV. For each sample, a flood gun was employed to minimize sample charging during photoelectron collection. Curve fitting and data analysis was carried out using the Avantage Software package (v.5.9490). The principal C 1s peak, the band at 284.8 eV, was used as the internal standard for charge correction.

5.3 Results & Discussion I: Surface functionalisation of Silicon Nanoneedles

Once fabricated, porous silicon nanoneedles go through a series of surface treatment steps before being used for biological applications. These usually include an oxidation treatment to pre-treat the silicon followed by the addition of chemical modifiers to functionalise the surface. A first example of XPS' ability to evaluate surface chemistry is shown in Figure 5.1. Here we see the effect of thermal treatment on the formation of a silicon oxide layer on flat silicon, silicon nanoneedles and silicon nanowires. The single peak around 104 eV corresponds to silicon oxide while the doublet peak around 100 eV corresponds to silicon. In figure 5.1 we can clearly see that the intensity of the oxide peak increases strongly after thermal treatment. Furthermore in the flat and nanoneedle cases, the silicon peak disappears completely. As photoelectrons can only escape from approximately 5 nm deep into a surface, these results suggest that the oxide layer has grown thicker than this.

In order to add chemical functionality to silicon surfaces for use in biological environments, these surfaces are often functionalised with 3-aminopropyl-triethoxysilane (APTES). This molecule binds hydroxyl groups on silicon surfaces and subsequently presents a free amine group allowing further functionalisation of the surface with peptides or biomolecules. Figure 5.2 shows a schematic of bare silicon surfaces after oxidation treatment and after functionalisation with APTES. [293, 294] As APTES requires free hydroxyl groups in order to attach to silicon surfaces, two oxidation protocols were investigated in order to generate these OH groups.

The first oxidation protocol involved subjecting silicon wafers to an oxygen (O_2) atmosphere plasma before treating the silicon with an APTES solution. The O_2 plasma cleans the surface by removing any organic contaminants that might be present and oxidises the surface. Silicon oxide presents silanol (Si-OH) at its surface which can be used by APTES in order to bind. The number and availability of free hydroxyls is a key bottleneck in the successful functionalisation of silicon. As such, in order to increase the number of these groups, silicon surfaces are often treated with a strong oxidising Piranha solution. This solution removes any organic matter and hydroxylates the silicon surface creating many more OH groups.

Figure 5.3 shows the C *1s*, N *1s* and Si *2p* core levels for both flat and nanoneedle silicon surfaces functionalised with APTES with and without Piranha treatment. Examining the flat and nanoneedle samples, we see the presence of a C-N chemical shift as well as a nitrogen signal confirming the presence of APTES on these surfaces. In addition, we see

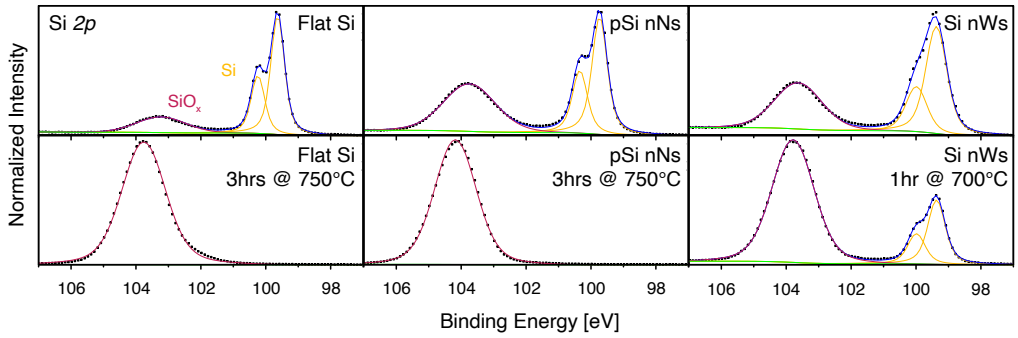

Figure 5.1: Si *2p* core levels showing the effect of thermal on oxidation silicon surfaces and the formation of thicker oxide layers.

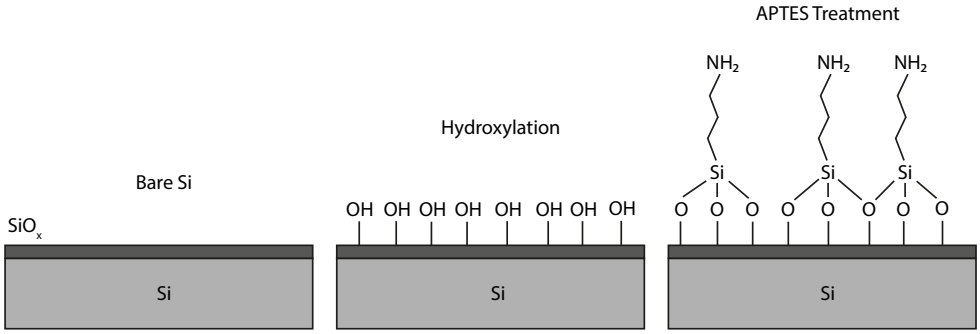

Figure 5.2: Schematic of a bare silicon surface, after oxidation treatment and after functionalisation with APTES.

a shoulder in the C *1s* signal for these surfaces around 289 eV. This cannot be associated with APTES, which only contains C-C and C-N bonds, and as such we can assume these additional chemical shifts are due to contamination. Once treated with Piranha solution, we see this shoulder disappear suggesting a better clean of the surfaces. In addition, the relative height of the C-N to C-C peaks in the C *1s* increases. This suggests a better functionalisation of the surface as the relative amount of carbon bound to nitrogen on the surface has increased. Furthermore, the amount of NH_3^+ increases on the Piranha treated surfaces although this does not suggest better functionalisation.

We can also perform the same XPS analysis throughout the functionalisation process. Figure 5.4 tracks the C *1s*, N *1s* and S *2p* peaks of silicon at each step during APTES-functionalisation. Starting with a flat silicon wafer which is then processed into nanoneedles, baked at 700°C for 3 hours, washed in Piranha solution and then treated with APTES. From figure 5.4, we again see a clear increase in silicon oxide after baking the sample as

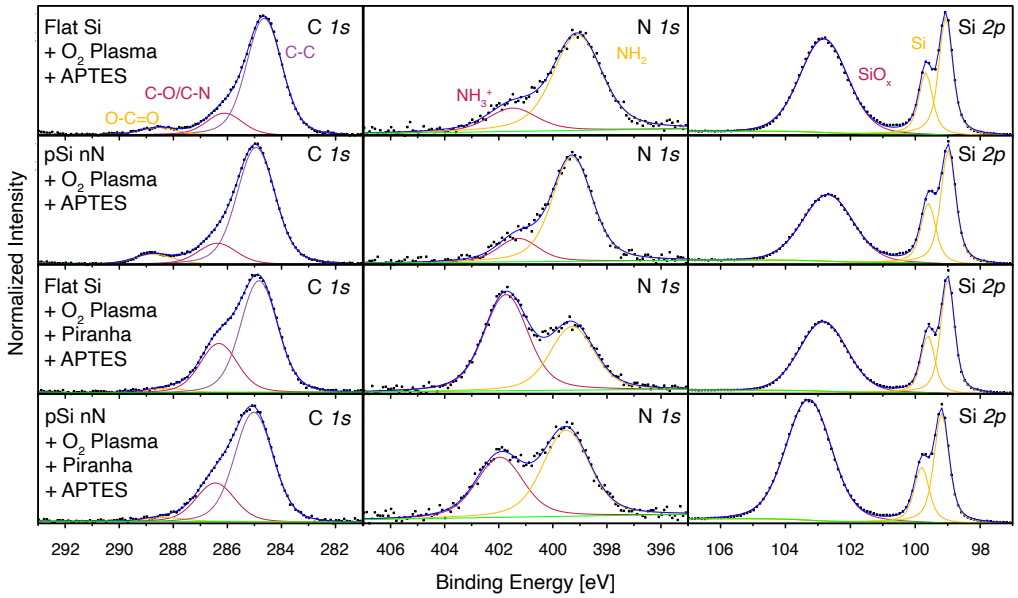

Figure 5.3: C *1s*, N *1s* and Si *2p* core levels of flat silicon and silicon nanoneedles showing the effect of a oxidation protocol on APTES functionalisation.

well as the appearance of a nitrogen peak after APTES-treatment. Furthermore, after baking and the Piranha bath, it is interesting to see the disappearance of higher energy carbon chemical groups, in particular the carboxyl peak around 288 eV which we can associate to the removal of organic contaminants from the surface. This peak does seem to re-appear after APTES treatment however. As APTES does not contain any C=O bonds, it is difficult to determine where this peak may be coming from other than re-contamination.

In addition to functionalising silicon nNs directly with APTES, one can adsorb biopolymers onto the surface in order to create a more biocompatible material. In this case, a chitosan/heparin (CS/HEP) mixture was used to coat silicon nanoneedles in order to make them more biocompatible with cells. These coatings can also be designed to be biodegradable in order to deliver drugs or biomolecules to cells. These coatings can be aided to stick to surfaces by pre-treating with a charged polymer mixture. Here a polyethylenimine/polyacrylic acid (PEI/PAA) mixture was used to pre-treat nanoneedles before adding the CS/HEP biopolymers.

Figure 5.6 shows the C *1s*, N *1s* and Si *2p* core leves for nanoneedles coated with a CS/HEP mixture directly as well as first pre-treated with a PEI/PAA coat. Here we see distinct changes in the shape of the C *1s* and N *1s* as more complex chemistry is added. In particular, the bare and O_2 plasma-treated nanoneedles shows fairly monodisperse peaks centered around 284 eV corresponding to C-C bonds. When the CS/HEP coat is added, the main

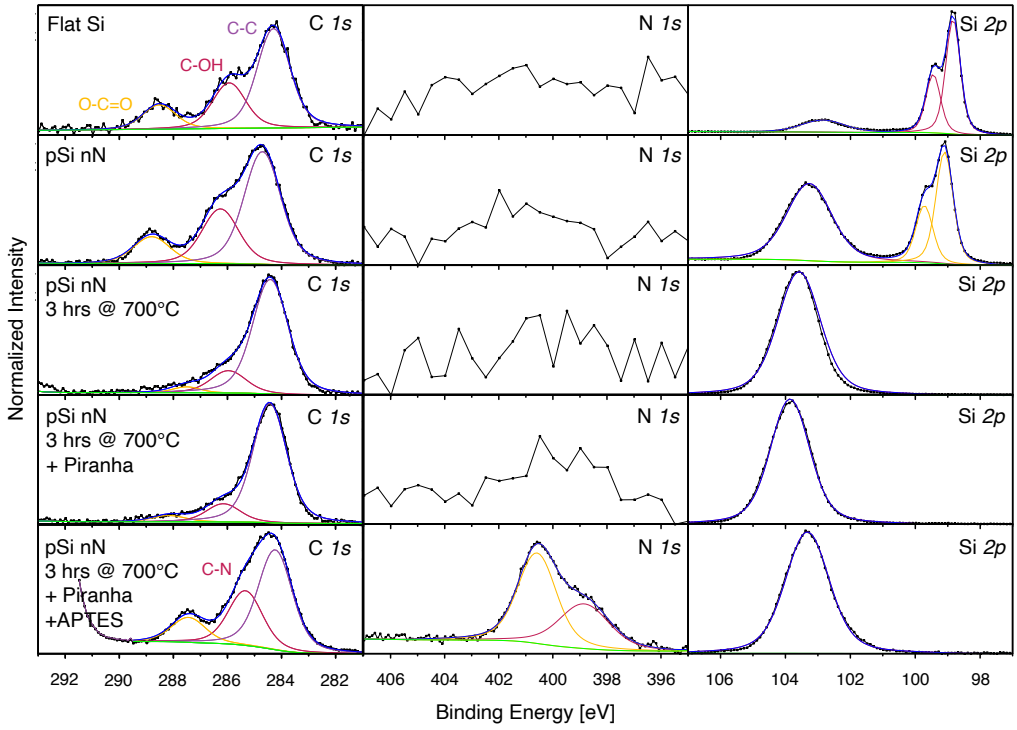

Figure 5.4: C *1s*, N *1s* and Si *2p* core levels at each stage during APTES functionalisation.

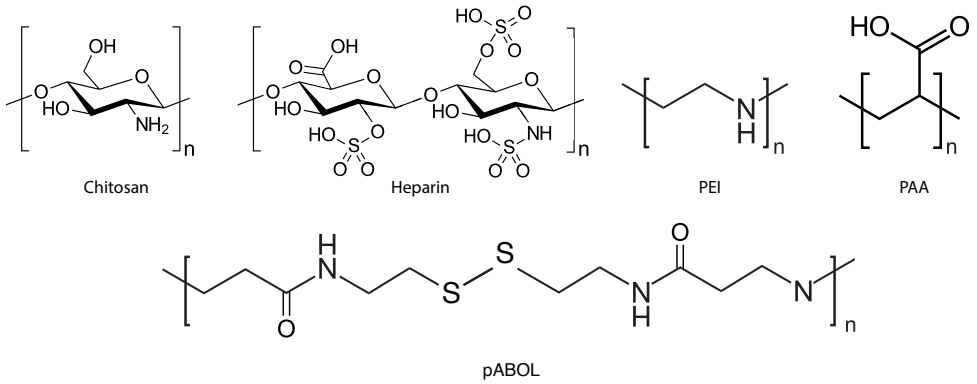

Figure 5.5: Chemical structure of chitosan, heparin, PEI, PAA and pABOL monomers. Adapted under a Creative Commons License from Wikipedia.

peak is now shifted to higher energy around 286 eV. This can be explained by the introduction of C-O and C-N chemical groups from CS/HEP which are more prevalent than C-C bonds. Furthermore, this main peak has shoulders on either side, corresponding to C-C at lower energy (284 eV) and the other corresponding to carboxylic groups (288 eV) which are present in both CS and HEP. When a PEI/PAA pre-coat is used we see a strong increase in the intensity of both the C-C and carboxylic peaks. As PEI and PAA are synthetic polymers, they have a higher content of C-C bonds, while PAA is a carboxylic acid and as such contains many carboxyl groups. In the N *1s* signal, we see a shift in intensity from a balanced state to a lower energy state at around 399 eV. This might be due to the differences in amine chemistry between CS and PEI; CS contains mostly primary amines (RNH_2) while PEI contains secondary amines (R_2NH). We can also see a relative decrease in the silicon oxide peak strength. This can be explained by an increasingly thicker polymer coat decreasing the number of photoelectrons that will reach the underlying oxide.

A final example of surface chemistry modification of silicon nanoneedles can be seen in figure 5.7. Here, nNs were treated first with HEP and then with a DNA-containing polymer (either poly(CBA-co-4-amino-1-butanol) (pABOL) or CS). These surfaces are designed to successfully allow for cell culture as well as for the delivery of therapeutic DNA to cells. Again, theses surfaces were tested with and without a pre-treatment with PEI. In figure 5.7, we see a clear different in each of the Carbon, Nitrogen and Sulfur core levels between the pABOL-DNA and CS-DNA cases. The presence or lack of PEI does not seem to affect the XPS spectra. This exemplifies the difficulty in differentiating molecules which contain similar chemical groups. Furthermore, the samples treated with CS-DNA show very similar C *1s* and N *1s* spectra to the CS/HEP treated sample shown in Figure 5.6 suggesting that the presence of PEI cannot be easily discerned by XPS in this case.

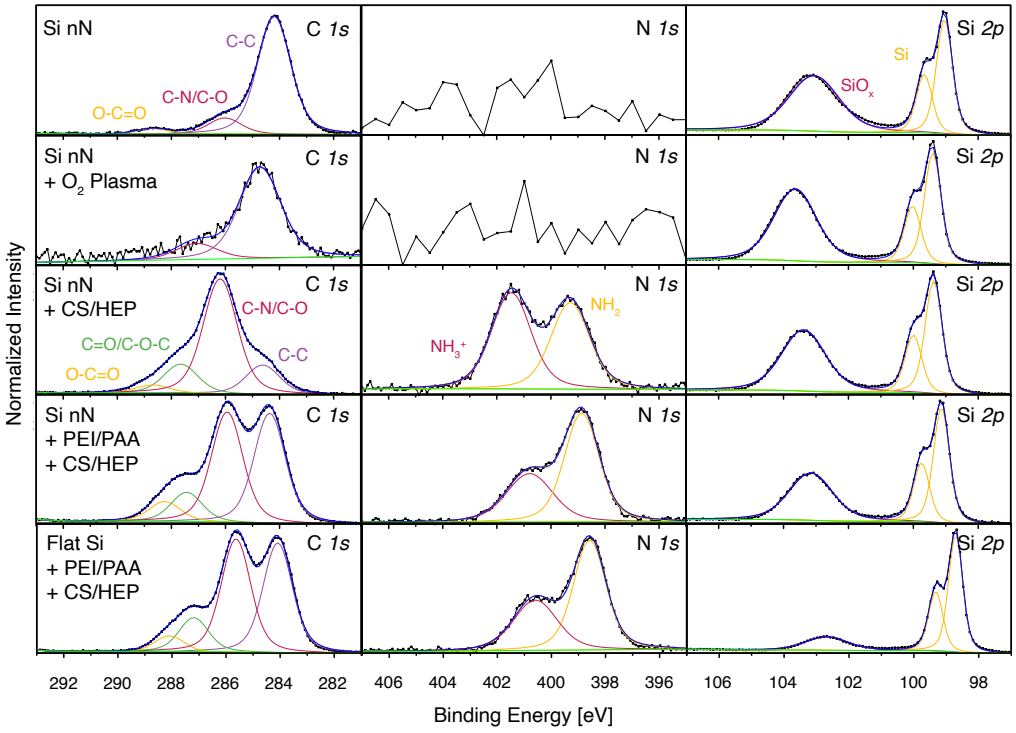

Figure 5.6: C *1s*, N *1s* and Si *2p* core levels of silicon surfaces coated with CS/HEP with and without a PEI/PAA pre-treatment. Note that the N *1s* signal in the first two rows is just noise and no signal was detected suggesting that Nitrogen is not present on those samples

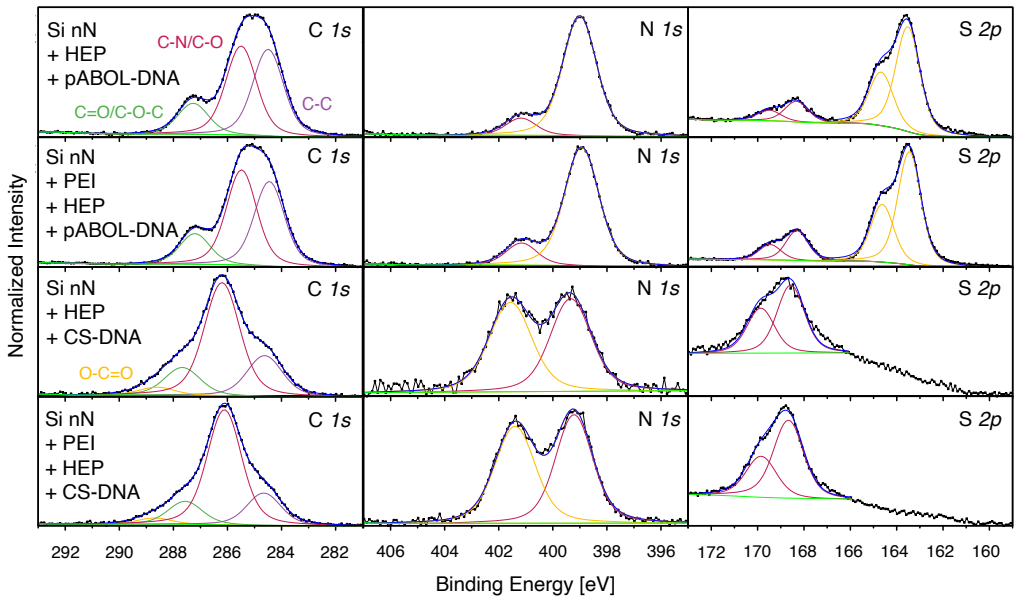

Figure 5.7: C *1s*, N *1s* and S *2p* core levels of silicon nanoneedles functionalised with heparin (HEP) and a pABOL-DNA or chitosan-DNA (CS-DNA) molecule as well as with and without a PEI pre-treatment.

Sulfur, like Silicon, exhibits a doublet state which can be clearly seen even without fitting the peaks centered around 64 eV for the pABOL-containing surfaces. This state disappears completely in the CS-DNA surfaces, being replaced by a higher energy state at around 169 eV. This could be explained by differences in sulfur chemistry between both groups. pABOL contains di-sulfide (R-S-S-R) bonds while heparin contains many sulfate and sulfite groups (SO_4 and SO_3).

Finally, we can evaluate the presence of DNA by examining the Phosphorus (P) peak in the XPS spectra for these cases as P is present in DNA backbone. Shown in figure 5.8, we can see that the overall P *2p* signal is very weak compared to other elements in these samples. However, for the pABOL-DNA cases we can just about make out the presence of a weak peak centred around 144 eV while the CS-DNA cases do no shown any significant signal in this energy range. Furthermore, the PEI-treated pABOL-DNA case shows a slightly clearer P *2p* peak suggesting that the presence of PEI may improve the attachment of pABOL to the surface and hence the biological payload of these materials.

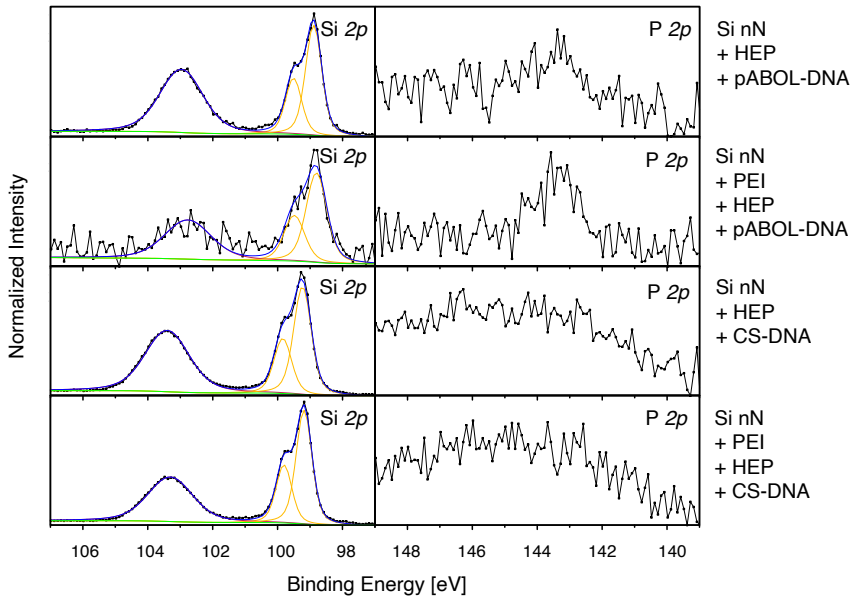

Figure 5.8: Si *2p* and P *2p* core levels of silicon nanoneedles functionalised with heparin (HEP) and a pABOL-DNA or chitosan-DNA (CS-DNA) molecule as well as with and without a PEI pre-treatment.

5.4 Results & Discussion II: Hydrogen Peroxide Disproportionation by Gold Nanoclusters

Ultra-small gold nanoclusters (AuNCs) have recently become of great interest for *in vivo* applications due to their extremely small size (< 2 nm) and biocompatibility. [295–297] These nanomaterials also have catalytic properties, allowing them to disproportionate hydrogen peroxide very efficiently (H_2O_2). Hydrogen peroxide disproportionation can in turn oxidise chromogenic substrates to provide a colorimetric readout for disease diagnosis. [298] In this instance, gold nanoclusters were employed as diagnostic tools *in vivo* to identify the presence of disease within a mouse model. [299]

The diagnostic system is shown schematically in Figure 5.9. AuNCs are bound to a neutravidin (NAv) core using peptide linkers. These linkers are designed to be cleavable by disease-specific proteases secreted *in vivo*. Hence, once injected into a mouse model, the AuNCs will be cleaved from their protein scaffold if the mouse is affected by disease. These cleaved AuNCs are then cleared by the kidneys and can be collected in the mouse's urine. Finally, H_2O_2 and a chromogenic substrate (3,3',5,5'-Tetramethylbenzidine, TMB) are added to the urine. If AuNCs are present in the mouse urine, they will disproportionate H_2O_2 into radicals which then oxidise TMB, changing the solution's color to blue. This allows for a simple readout for the presence or lack of a disease in a mouse model which can be modulated by the use of disease-specific peptide linkers.

This diagnostic system was shown to work experimentally but the method by which AuNCs react with hydrogen peroxide is not well understood. Horseradish peroxidase, the archetypical hydrogen peroxide catalyst, has been studied extensively, [300] but there is little to no direct characterization of this catalytic reaction on AuNCs. As such, XPS was selected to shed light onto the mechanism of peroxide dissociation by AuNCs.

AuNCs are formed of a core of gold atoms (25 atoms in this case) which are stabilized by glutathione (GSH, see Figure 5.10) ligands via surface sulfur groups. It is thought that catalysis occurs when the H_2O_2 molecules react with the AuNC core due to the reactive nature of nanogold. [301] Figure 5.11 shows schematics of thiol-terminated AuNCs of different sizes. With XPS, the hope is that we can identify chemical shifts in order to identify reactive sites on the clusters.

The first experiment designed aimed to characterize the AuNCs in the presence of increasing peroxide concentration to understand their behaviour. Figure 5.12 shows the Au *4f*, S

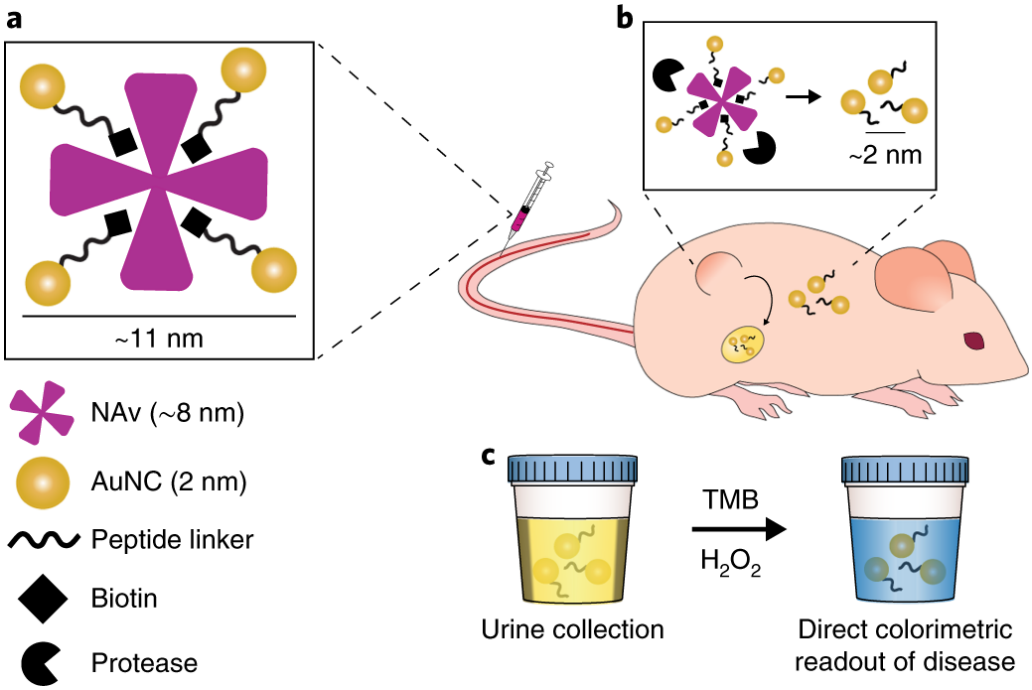

Figure 5.9: Schematic of the AuNC diagnostic system, showing (a) , (b) and (c) The colorimetric change highlighted in (c) is the step of interest to us in the context of this thesis. Reproduced with permission. [299] Copyright 2019, Springer Nature.

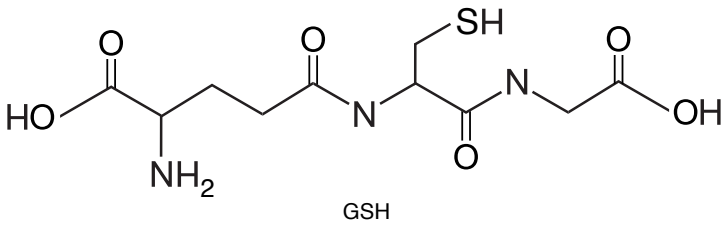

Figure 5.10: Chemical structure of GSH.

2p and C *1s* core levels for the GSH-coated AuNCs under increasing hydrogen peroxide concentration. Surprisingly, we see a noted shift in energy in the S *2p* peak signal as we increase peroxide concentration. Indeed, the control group shows two distinct energy levels for sulfur present in the sample, one peak located around 162 eV and a higher energy state located at 168 eV. The intensity of the "high energy" peak increases as hydrogen peroxide concentration is increased while the "low energy" peak decreases in intensity. This can be described as a shift in chemical state of the sulfur present in the sample. The chemical groups in glutathione are seen in the C *1s* signal, notably C-N, C-S and C=O. The Au *4f* and C *1s* peaks do not show any noticeable changes in intensity under increasing peroxide concentration suggesting the Sulfur group is active when AuNCs are exposed to hydrogen

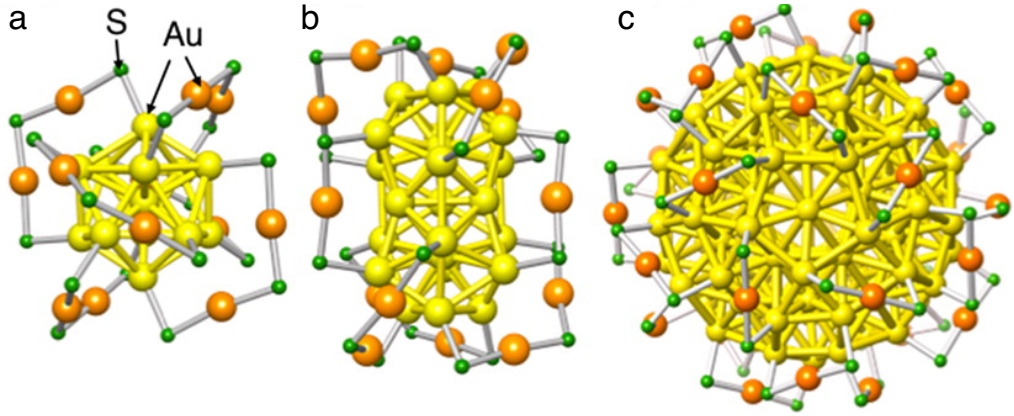

Figure 5.11: Schematic atomic structures of (a) Au_{25}, (b) Au_{38} and (c) Au_{144}, commonly used thiolate-protected AuNCs. Green, orange and yellow beads correspond to Sulfur, surface Gold and core Gold atoms respectively. Adapted with permission from Kurashige *et al.* [302] Copyright 2014, American Chemical Society.

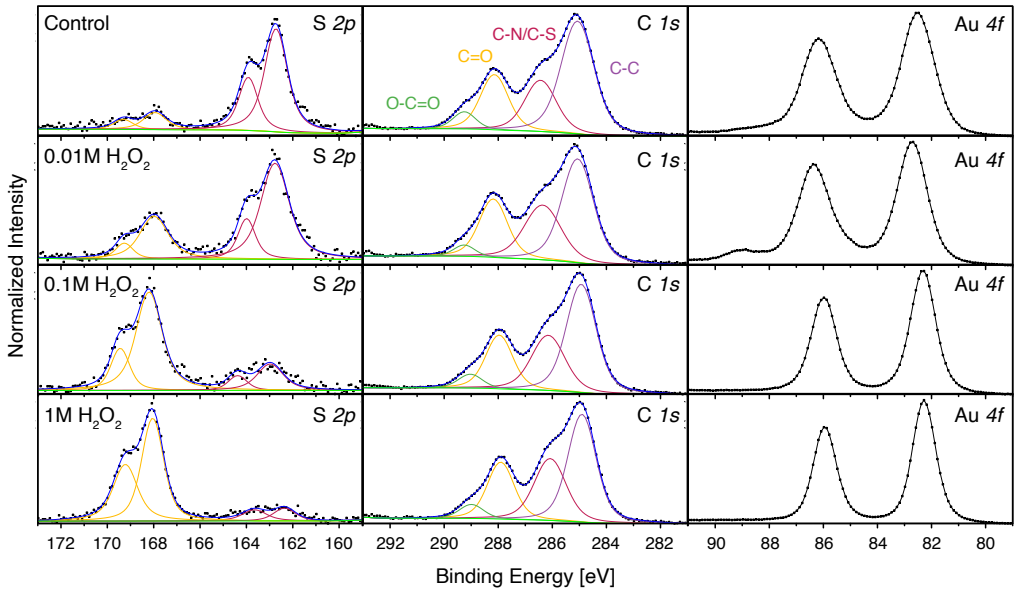

Figure 5.12: Au *4f*, S *2p* and C *1s* spectra for GSH-coated AuNCs under increasing hydrogen peroxide concentration.

peroxide.

As GSH can have some catalytic roles in the body, we aimed to deconvolute the contribution of the GSH ligand from the AuNC. As such, we repeated a spike experiment exposing both GSH-AuNCs and pure GSH to increasing concentration of hydrogen peroxide. Fig-

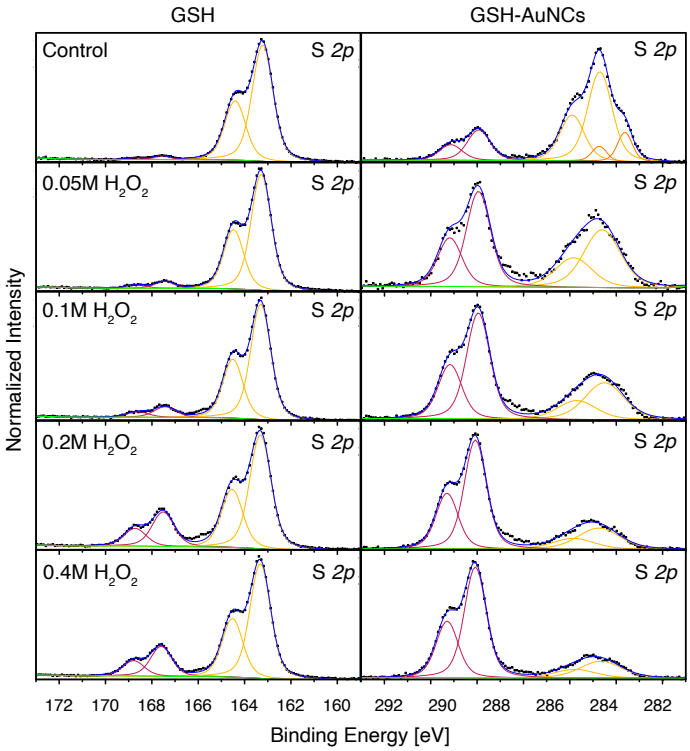

Figure 5.13: S2p spectra for pure GSH and GSH-coated AuNCs under increasing hydrogen peroxide concentration.

ure 5.13 shows the S *2p* signal for pure GSH and GSH-coated AuNCs under increasing peroxide concentration. Here, we observe a very similar shift in the AuNC signal as in figure 5.12, with the "high energy" sulfur state increasing in intensity while the "low energy" state decreases. Interestingly, in the pure GSH case, we see a slight increase in the high energy sulfur peak but to a much lesser extent compared to AuNCs. This results could highlight the catalytic effect that such AuNCs have. Examining the C *1s* and Au *4f* peaks in figure 5.14 for the GSH-only and AuNCs, we see that no significant changes occur in the ligand chemistry for either sample.

Following this, we investigated the spectra of bare AuNCs, GSH-coated AuNCs and pure GSH with and without exposure to hydrogen peroxide. This would allow us to determine what the contribution of each component part of the AuNC diagnostic system has for peroxide disproportionation. Figure 5.15 shows the S *2p* signal of bare AuNCs, GSH-AuNCs and pure GSH with and without exposure to 0.5 M of hydrogen peroxide. Again, with pure GSH we see a slight shift in the S *2p* signal to a higher energy state which is much more prominent in the GSH-AuNC case. Bare AuNCs also seem to present a similar shift to the GSH-functionalised AuNCs, highlighting the catalytic nature of nanogold surfaces.

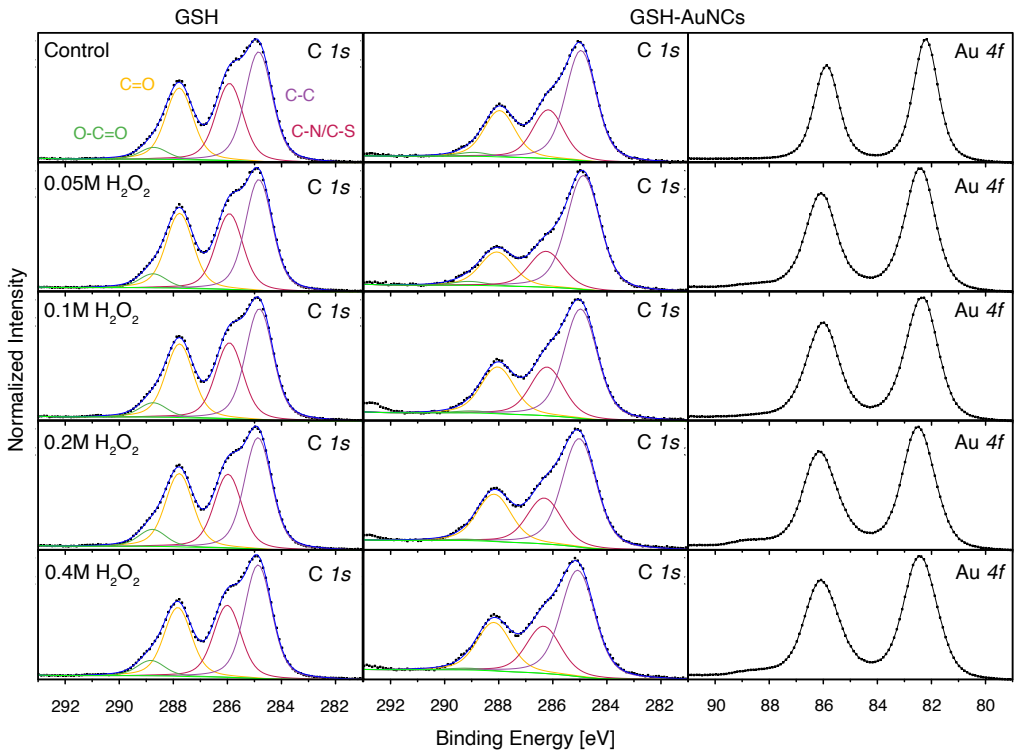

Figure 5.14: C1s spectra for pure GSH and GSH-coated AuNCs under increasing hydrogen peroxide concentration as well as Au4f signal of AuNCs.

As such these results allow us to posit that the surface thiol on the AuNC surface plays a key role in the catalytic disproportionation of hydrogen peroxide. We are still limited in our understanding of the exact intermediates and process ongoing at this interface however as XPS can only provide a static before and after image of this catalytic process. Furthermore, the exact nature of the sulfur chemical state formed after disproportionation is unknown and cannot be directly elucidated via XPS. S *2p* peaks in the range of 168 to 169 eV have been posited to correspond to disulfide bonds as well as metal sulfate states. [303] More in depth chemical investigation is required to determine the exact state of Sulfur during this catalytic reaction.

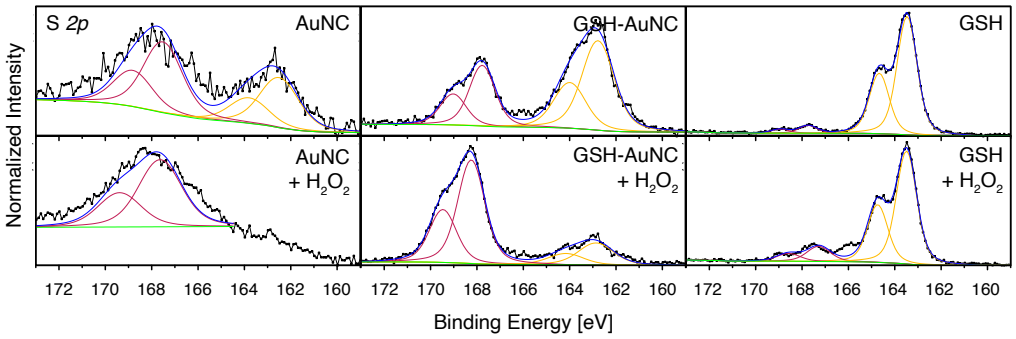

Figure 5.15: S2p spectra for bare AuNCs, GSH-AuNCs and pure GSH with and without hydrogen peroxide (500 mM).

5.5 Conclusion & Outlook

In conclusion, this chapter presented the application of XPS to the characterisation of biologically-active nanomaterials. Firstly, the surface chemistry of various silicon surfaces was explored to understand the formation of oxide layers as well as to characterize the presence of functional chemical groups. We studied how XPS can be used to validate functionalisation protocols and compare them. XPS was also employed to search for the presence of adsorbed polymers to nanoneedle surface as well as to identify payload-containing biomolecules on these surfaces. These results highlight both the importance and the complexity of understanding surface chemistry for materials with biological applications.

Secondly, XPS was employed to investigate the catalytic activity of gold nanoclusters (AuNCs). XPS allowed for the identification of a key chemical shift in the Sulfur state of GSH-functionalised AuNCs during disproportionation of hydrogen peroxide. Interestingly, XPS was able to identify a significant shift in the chemical state of Sulfur from a low energy state to a higher energy state. This was compared to the potential activity of the GSH ligand and the bare AuNC surface and it was found that the surface of thiol-protected AuNCs seem to be playing a key role in the disproportionation reaction. The limitations of XPS however, mean that we cannot elucidate more information on the chemical reaction ongoing at the surface nor the exact chemical state of Sulfur after reaction.

Chapter 6

Conclusion

6.1 Conclusions & Future Scope

Following the research presented in chapters 2,3 and 4, more work can be invested in exploring the interplay of cell membrane curvature, lipid localization and protein binding. One of the largest gaps in our knowledge of the bio-nano interface is the lack of detailed biophysical information on the state of the cell membrane when in contact with nanotextured surfaces. The research presented in Chapter 2 is an early foray into developing this field, however this work has many limitations and further work is necessary to improve current approaches.

Scale is one of the clearest limitations of current work on cell membrane curvature. Although continuum models allow for much larger length and time scales, large-scale molecular simulations of curvature processes are lacking. The system presented in chapter 2 presents radii of curvature below 10 nm. As we have seen in the introduction, membrane curvature regions in cells can range from tens to hundreds of nanometers in size, hence this thesis is only touching upon the smallest of radii of curvature. Exploring the molecular arrangements ongoing during curvature at a scale of hundreds of nanometers would be highly interesting. Current computational power could allow for some very large systems to be built at this scale using the same level of coarseness employed in this thesis work. Figure 6.1 shows an example of a CG simulation performed during this thesis work of a 20 nm radius liposome. This highlights the ease with which relatively large radii of curvature can be studied with regular high-performance computing equipment. Combined with implicit solvent models, there is a strong potential to be able to study certain curvature processes at real scale. Modelling curvature progression during endocytosis would be an ideal candidate to investigate due to the varied shapes and types of curvature presented

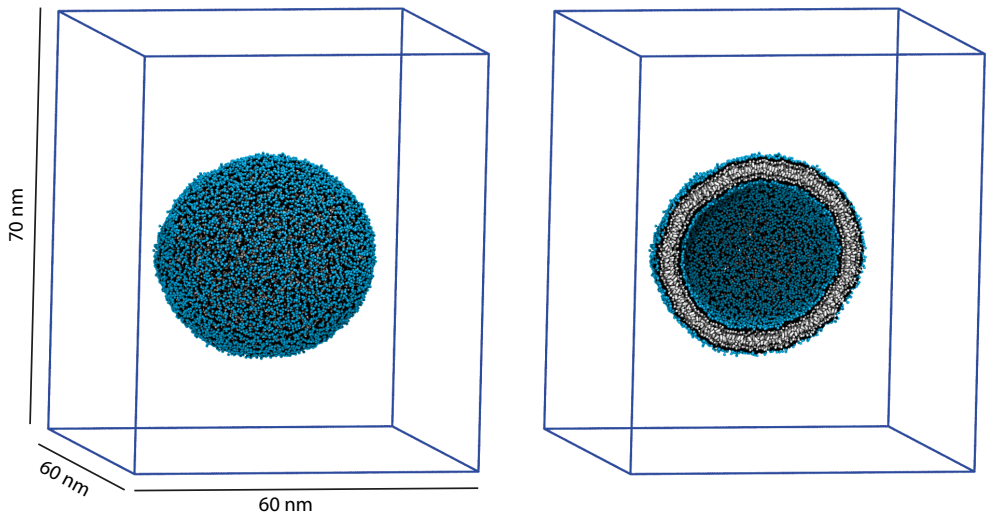

Figure 6.1: Snapshots of a 40 nm diameter liposome after 1 μs of simulation time in solvent with and without a cross-sectional view of the liposome interior.

during this process.

In addition to scale, the study of various levels of membrane curvature and their biological effects is lacking in the literature. Indeed, a fixed membrane curvature is used throughout chapters 3 and 4 to study the binding of the ENTH and ANTH domains. Repeating these studies at different membrane curvature levels would allow us to quantify the strength of the curvature sensitivity of these proteins and their respective structural actors. One can posit that amphipathic helix insertion as a curvature mechanism is strongly active at very small radii of curvature while curvature sensing by BAR domains on the other hand is active at larger radii. Furthermore, lipid species also have specific curvature sensitivity and varying the range of curvature will allow us to study which lipids prefer curvature and to what extent.

Finally, the curvature model used in chapters 2, 3 and 4 relies on a rigid substrate to induce and stabilise membrane curvature. Although the artefacts and disruptions to membrane behaviour are minimal, this model lacks both elegance and adaptability. Indeed whole new substrates need to be built and designed to accommodate different curvature radii and only one side of the membrane is accessible to solvent and proteins. A recent improvement is the the development of EnCurve, a curvature fixing tool for MD simulations, by Yesylevskyy *et al*. [304] This tool allows for direct introduction and stabilisation of membrane curvature without restricting lipid diffusion nor membrane properties in both coarse-grained and atomistic membrane simulations. As such, this tool will be highly useful for future studies of membrane curvature and presents a significant improvement on the curvature model

employed in this thesis.

6.1.1 Membrane Composition

Another strong limitation of the membrane model employed in this thesis is the limited lipidic complexity of this membrane. Indeed, *in vivo* plasma membranes are very chemically complex with at least six different types of lipid not including proteins and other biomolecular components as highlighted in Figure 6.2. [305] As such, the membrane models used in this thesis are extremely simplistic (see Figure 6.1) and could be greatly improved by the inclusion of key membrane components. The study of membranes with *in vivo* lipid compositions has recently become of interest to many in the membrane biophysics community. Such complex membrane compositions allow for the study of spontaneous lipid clustering and lipid raft formation as well of specific protein-lipid interactions. [84, 306, 307] As these lipidic domains are thought to have significant biological consequences, [308, 309] it would be highly valuable to explore complex membrane compositions computationally. Coupled to membrane curvature, it would be very interesting to study curvature specificity of lipids, as has been shown for PIP2. [84] Curvature processes like endocytosis combine multiple lipid species with both spatial and temporal complexity. Varying the level of membrane curvature and studying lipid redistribution would be very useful for furthering our understanding of fundamental processes ongoing during endocytosis. Furthermore, having a better understanding of the lipidic redistributions during membrane deformation will also improve our knowledge of potential effects on cells when interfaced with nanostructured materials.

In addition to more complex lipid compositions, the presence of membrane proteins and transmembrane proteins within membrane models is lacking. Studies have explored protein and nanoparticle clustering on membranes, [29, 310] and this clustering can even be lipid-driven. [311, 312] Applied to membrane curvature, this would allow for the study of protein clustering due to curvature and potentially structural changes in proteins at membrane curvature. This was touched upon in the introduction but further investigation of membrane protein structure-function relationships in regions of membrane curvature would be highly interesting. Furthering the complexity of membranes with respect to proteins has been of keen interest to the field of bacterial membrane simulations as these are often highly complex membrane structures held together with large proteins and lipopolysaccharides. [313] The recent reviews by Pezeshkian *et al* and Marrink *et al* [314, 315] are excellent introductions to the current state of both membrane curvature simulations and realistic membrane simulations.

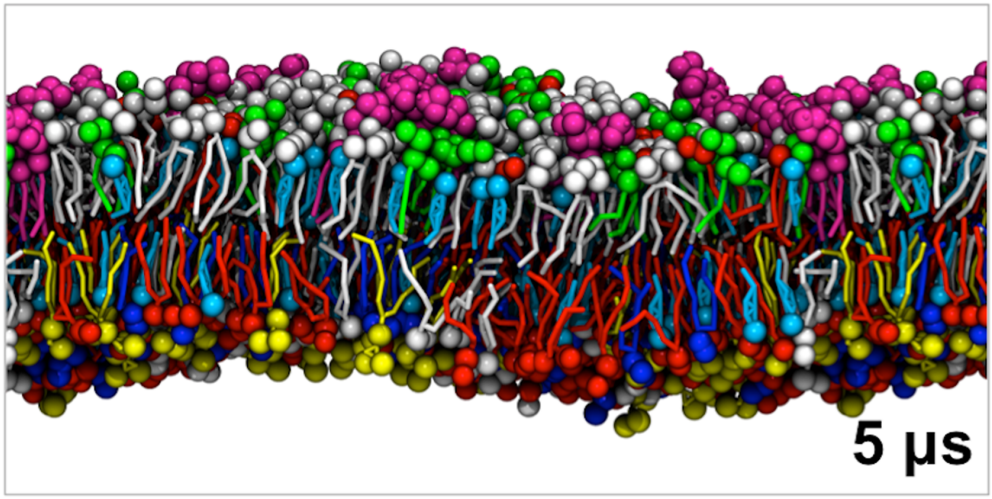

Figure 6.2: Snapshot of a complex composition membrane after 5 μs of simulation containing various lipids (PC in light gray, PE in red, Sphingomyelin in green, PS in blue and PIP2 in yellow) as well as a glycolipid (GM3) in magenta and Cholesterol in cyan. Adapted with permission under a Creative Commons License from Koldso *et al.* [84]

6.1.2 Protein Localization

In addition to membrane composition and complexity, the study of protein localization to membranes could be expanded. The work in this thesis examined single proteins localizing to membrane curvature. In reality, multiple proteins will be interacting simultaneously with curvature. While some studies have explored how pre-assembled protein-lattices can deform membranes, [53, 151, 156], being able to observe the dynamic self-assembly of such lattices would be highly interesting to understand *in vivo* protein behaviour. Furthermore, recent experimental work has suggested that membrane curvature proteins, such as the ENTH and ANTH domains, can form complexes once bound to the membrane. [257, 267–269] As such, it would be highly interesting to study membrane curvature in the presence of multiple proteins in order to elucidate their coordinated action. Similarly to the previous section discussing membrane composition, understanding how membrane curvature can promote or disrupt protein assemblies would be highly interesting to investigate as well. As some recent work on the spatial localization of proteins has been resolved through painstaking experiments, [101] computational modelling of curvature with multiple proteins present would help steer these developments.

The work presented in this thesis studied only two curvature active proteins in detail and their interaction with curvature. Membrane curvature processes such as endocytosis contain many different proteins which can potentially play important biological roles. As such,

more proteins need to be studied and their interaction with curvature explored. During the work performed in this thesis, a number of other protein domains were investigated for their potential membrane curvature activity. Figure 6.3 shows simulations performed on 5 other PIP2-binding domains interacting with the same 97.5% PC and 2.5% PIP2 curved membrane as used in chapters 3 and 4. These proteins include three different structures of the PH domain, a FERM domain and a PX domain. Although none of these proteins exhibited curvature activity, the model developed in this thesis allows for relatively rapid testing of the curvature sensing behaviour of protein domains. Furthermore, none of the proteins investigated in figure 6.3 are known to sense membrane curvature, as such these results serve as a negative control to validate the modelling approach used in this thesis. Simulation can be used to screen for protein function and have contributed to the discovery of new curvature active proteins such as annexins. [316]

The large database of protein structures freely available will allow for a large exploration of proteins and their interactions with membranes and membrane curvature. Coupled to the introduction of more complex membrane compositions, a large number of studies are ongoing to understand specific membrane and lipid interactions of protein domains. These studies have been pioneered in particular by the Sansom group whereby protein dynamics and lipid binding are extensively explored to understand protein orientations and interactions in their functional form on membranes. [307, 317, 318] As such, simulations allow us to further our fundamental understanding of both chemical and physical protein-lipid interactions.

In addition, the simulations performed in this thesis were coarse-grained in order to simulate at larger length and time scales. These simplifications, although validated and insightful, do reduce the extent to which information that can be extracted from the simulations. Moving to fully atomistic simulations of proteins interacting with membrane curvature would be ideal to study structural changes in the protein but the computational limitations are clear. Multiscale or hybdrid atomistic/coarse-grained simulations could potentially be employed to study protein structure dynamics at curvature and protein-lipid interactions at curvature in more detail. [319] The investigation of structural changes in the ENTH domain in chapter 3 is a simplistic example of what could be achieved using more elaborate simulation methods.

Following on, the protein localization results presented in this thesis relied on multiple repeats and long simulation times in order to generate statistically relevant distributions of protein behaviour. This approach is computationally intensive and far from guarantees that the equilibrium localization profile of a protein will be reached. As such, future

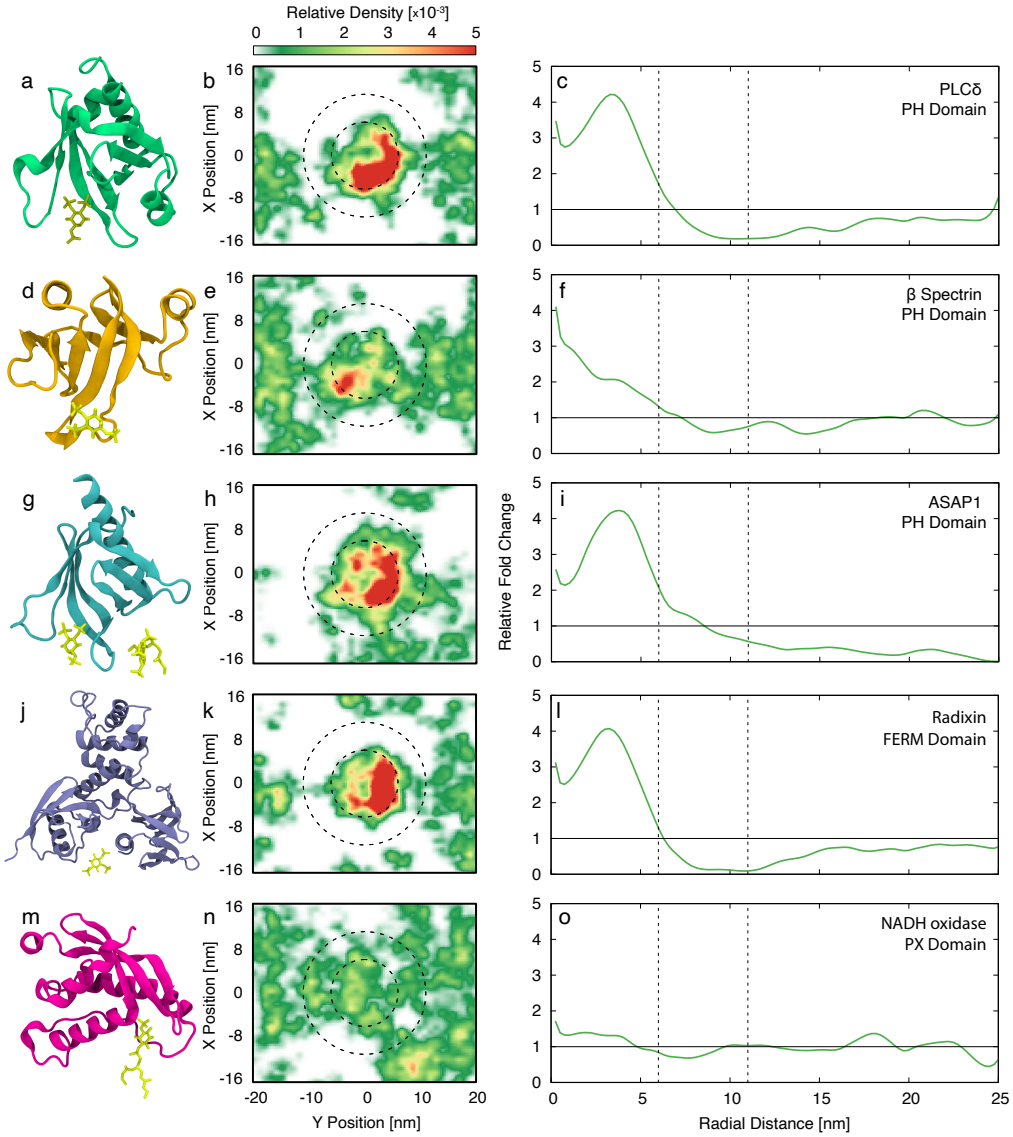

Figure 6.3: Crystal structure, top-down localization heatmap and relative fold change of (a-c) PLCδ, (d-f) β spectrin and (g-i) ASAP1 PH domains as well as (j-l) Radixin FERM domain and (m-o) NADH oxidase PX domain respectively interacting on PC/PIP2 membranes.

approaches could employ free energy methods such as umbrella sampling and metadynamics simulations to generate more accurate data on a protein's spatial preference on curved membranes. [35, 36] Both these approaches were attempted during the thesis research. Unfortunately, consistently generating trajectories across membrane curvature in umbrella sampling was not achievable and attempts at metadynamics simulations were extremely computationally expensive due to the system size and did not converge within the time frame of this thesis. Despite this, free energy calculations of the ANTH domain, presented in Chapter 4, are currently being undertaken in collaboration with the Sansom group at the University of Oxford. Using the ANTH domain localization results from non-biased simulations, umbrella sampling simulations will be performed to remove the protein from flat, convex and concave regions of membrane curvature. From these results, an estimate of the relative difference in binding energy of the protein at various membrane regions will hopefully be achieved yielding more reliable curvature activity estimates for the protein and its structural variants.

6.1.3 Surface Chemistry

Chapter 5 presented results on the application of XPS to the study of materials surfaces in order to evaluate their potential for applications in biological settings. Despite the insight that is possible using this technique, these results are inherently limited by the shortcomings of XPS. Indeed, as covered briefly in chapter 5, XPS is performed under ultra-high vacuum conditions which can greatly change the "real" chemistry within a system. As most biological applications are applied in aqueous environments, the likelihood of bond breaking and chemical changes occurring between dry and hydrated states is high. Luckily, many advances to the methodology of XPS have been developed to address this issue including using flash freezing of samples, using ambient pressure XPS and directly adsorbing water vapour onto surfaces. [288–290]. Furthermore, coupling XPS results with other advanced characterisation techniques such as secondary ion mass spectroscopy (SIMS), scanning probe microscopy (SPM) and Raman spectroscopy for example can allow for researchers to gain a more complete picture of the chemical state of material surfaces, using each technique to overcome the limitations of others.

6.2 Summary

Overall, this thesis has explored the interface between biology and nanomaterials using computational modelling and x-ray photoelectron spectroscopy. By employing coarse-grained molecular dynamics simulations, it was found that cell membrane curvature can be induced through the design of nanoporous wafers and that such structures can strongly influence the biophysical properties of these membranes. Three key wafer design parameters were determined; pore taper, pore radius and surface attraction. The potential biological implications of membrane curvature was confirmed through the observation of increased protein localization to regions of curvature.

Following the development of this membrane curvature simulation system, this thesis queried the structural basis behind membrane curvature sensing of the ENTH domain. By studying this domain with and without its terminal helix, it was found that the protein could accurately sense membrane curvature even without its supposed key curvature-active H0 helix. The binding and interactions of the ENTH domains with its lipid binding partner, PIP2, were also explored in the context of curvature sensing as well as the effect of a rigid elastic network on protein localization to membrane curvature.

Expanding on this, the curvature sensing of another protein domain, the ANTH domain, was investigated. By varying the structure of this domain's terminal a0/a1 helices, it was also shown that the ANTH domain presents innate curvature attraction on neutrally charged membranes due to the action of adjacent hydrophobic residues in the domain. In the presence of negatively charged lipids, it was shown that the domain can only accurately sense membrane curvature with a full, rigid terminal helix. It was hypothesised that PIP2 lipids play an opposing role to curvature sensing of such proteins domains due its preference for regions of concave membrane curvature.

Finally, expanding on the importance of surface attraction on the design of nanoporous wafers for membrane curvature induction, this thesis explored the application of XPS for the surface characterisation of nanomaterials. In particular, the surface chemistry of silicon nanoneedles were characterised to query the successful functionalisation of these materials for applications in drug delivery and cellular interfacing. In addition, XPS was applied to characterise the chemical activity of gold nanoclusters (AuNCs) to shed light onto the potential catalytic reactions ongoing at the nanocluster surface.

6.3 Perspective

This thesis has demonstrated the characterisation of nano-bio interactions through the use of computational methods and advanced characterisation techniques. This thesis has explored how membrane deformation might be forthcoming when interfacing cells with nanostructured materials and how these materials might change biophysical properties of membranes. Furthermore, the structural basis for membrane curvature sensing of proteins was explored along with their lipid interactions. The work presented in this thesis provides an early exploration of this complex interface and sets the foundation for future studies aiming to understand the functional effect of materials on cell membranes as well as to query fundamental questions in structural biology and membrane biophysics.

Bibliography

1. Milo, R. & Phillips, R. *Cell Biology by the Numbers* (Garland Science, New York, 2015).
2. Kolind, K., Leong, K. W., Besenbacher, F. & Foss, M. Guidance of stem cell fate on 2D patterned surfaces. *Biomaterials* **33**, 6626–6633 (2012).
3. Lee, M. R. *et al.* Direct differentiation of human embryonic stem cells into selective neurons on nanoscale ridge/groove pattern arrays. *Biomaterials* **31**, 4360–4366 (2010).
4. Kilian, K. A., Bugarija, B., Lahn, B. T. & Mrksich, M. Geometric cues for directing the differentiation of mesenchymal stem cells. *Proceedings of the National Academy of Sciences of the United States of America* **107**, 4872–4877 (2010).
5. Qian, T. & Wang, Y. Micro/nano-fabrication technologies for cell biology. *Medical and Biological Engineering and Computing* **48**, 1023–1032 (2010).
6. Chen, C. S., Mrksich, M., Huang, S., Whitesides, G. M. & Ingber, D. E. Geometric control of cell life and death. *Science* **276**, 1425–1428 (1997).
7. Discher, D. E., Janmey, P. & Wang, Y. L. Tissue cells feel and respond to the stiffness of their substrate. *Science* **310**, 1139–1143 (2005).
8. Wen, J. H. *et al.* Interplay of matrix stiffness and protein tethering in stem cell differentiation. *Nature Materials* **13**, 979–987 (2014).
9. Pek, Y. S., Wan, A. C. & Ying, J. Y. The effect of matrix stiffness on mesenchymal stem cell differentiation in a 3D thixotropic gel. *Biomaterials* **31**, 385–391 (2010).
10. Leipzig, N. D. & Shoichet, M. S. The effect of substrate stiffness on adult neural stem cell behavior. *Biomaterials* **30**, 6867–6878 (2009).
11. Tse, J. R. & Engler, A. J. Stiffness gradients mimicking in vivo tissue variation regulate mesenchymal stem cell fate. *PLoS ONE* **6** (2011).
12. Engler, A. J., Sen, S., Sweeney, H. L. & Discher, D. E. Matrix Elasticity Directs

Stem Cell Lineage Specification. *Cell* **126**, 677–689 (2006).

13. Gilbert, P. M. *et al.* Substrate elasticity regulates skeletal muscle stem cell self-renewal in culture. *Science* **329**, 1078–1081 (2010).

14. Fromherz, P. & Voelker, M. Comment on "detection, stimulation, and inhibition of neuronal signals with high-density nanowire transistor arrays". *Science* **323**, 1100–1104 (2009).

15. Qing, Q. *et al.* Nanowire transistor arrays for mapping neural circuits in acute brain slices. *Proceedings of the National Academy of Sciences of the United States of America* **107**, 1882–1887 (2010).

16. Xie, C. *et al.* Noninvasive neuron pinning with nanopillar arrays. *Nano Letters* **10**, 4020–4024 (2010). arXiv:NIHMS150003.

17. Robinson, J. T. *et al.* Vertical nanowire electrode arrays as a scalable platform for intracellular interfacing to neuronal circuits. *Nature Nanotechnology* **7**, 180–184 (2012). arXiv:NIHMS150003.

18. Timko, B. P. *et al.* Electrical recording from hearts with flexible nanowire device arrays. *Nano Letters* **9**, 914–918 (2009).

19. Timko, B. P., Cohen-Karni, T., Qing, Q., Tian, B. & Lieber, C. M. Design and implementation of functional nanoelectronic interfaces with biomolecules, cells, and tissue using nanowire device arrays. *IEEE Transactions on Nanotechnology* **9**, 269–280 (2010).

20. Duan, X. *et al.* Intracellular recordings of action potentials by an extracellular nanoscale field-effect transistor. *Nature Nanotechnology* **7**, 174–179 (2012).

21. Jain, R. K. & Stylianopoulos, T. Delivering nanomedicine to solid tumors. *Nature Reviews Clinical Oncology* **7**, 653–664 (2010).

22. Shi, J., Votruba, A. R., Farokhzad, O. C. & Langer, R. Nanotechnology in drug delivery and tissue engineering: From discovery to applications. *Nano Letters* **10**, 3223–3230 (2010).

23. Chiappini, C. *et al.* Biodegradable silicon nanoneedles delivering nucleic acids intracellularly induce localized in vivo neovascularization. *Nature Materials* **14**, 532–539 (2015).

24. Chiappini, C. *et al.* Biodegradable nanoneedles for localized delivery of nanoparticles in vivo: Exploring the biointerface. *ACS Nano* **9**, 5500–5509 (2015).

25. Kasemo, B. Biological surface science. *Surface Science* **500**, 656–677 (2002).

26. Alder, B. J. & Wainwright, T. E. Phase transition for a hard sphere system. *The Journal of Chemical Physics* **27**, 1208–1209 (1957).

27. McCammon, J. A., Gelin, B. R. & Karplus, M. Dynamics of folded proteins. *Nature* **267**, 585–590 (1977).

28. Sener, M., Strumpfer, J., Singharoy, A., Hunter, C. N. & Schulten, K. Overall energy conversion efficiency of a photosynthetic vesicle. *eLife* **5**, 09541 (2016).

29. Chavent, M. *et al.* How nanoscale protein interactions determine the mesoscale dynamic organisation of bacterial outer membrane proteins. *Nature Communications* **9**, 2846 (2018).

30. Jung, J. *et al.* Scaling molecular dynamics beyond 100,000 processor cores for large-scale biophysical simulations. *Journal of Computational Chemistry* **40**, 1919–1930 (2019).

31. Pezeshkian, W., König, M., Wassenaar, T. A. & Marrink, S. J. Backmapping triangulated surfaces to coarse-grained membrane models. *Nature Communications* **11** (2020).

32. Girodat, D., Pati, A. K., Terry, D. S., Blanchard, S. C. & Sanbonmatsu, K. Y. Quantitative comparison between sub-millisecond time resolution single-molecule FRET measurements and 10-second molecular simulations of a biosensor protein. *PLoS Computational Biology* **16**, e1008293 (2020).

33. Hospital, A., Goñi, J. R., Orozco, M. & Gelpí, J. L. Molecular dynamics simulations: Advances and applications (2015).

34. Ode, H., Nakashima, M., Kitamura, S., Sugiura, W. & Sato, H. Molecular dynamics simulation in virus research. *Frontiers in Microbiology* **3**, 1–9 (2012).

35. Barducci, A., Bonomi, M. & Parrinello, M. Metadynamics. *Wiley Interdisciplinary Reviews: Computational Molecular Science* **1**, 826–843 (2011).

36. Kästner, J. Umbrella sampling. *Wiley Interdisciplinary Reviews: Computational Molecular Science* **1**, 932–942 (2011).

37. Zwier, M. C. & Chong, L. T. Reaching biological timescales with all-atom molecular dynamics simulations. *Current Opinion in Pharmacology* **10**, 745–752 (2010).

38. Brooks, B. R. *et al.* CHARMM: A program for macromolecular energy, minimization, and dynamics calculations. *Journal of Computational Chemistry* **4**, 187–217 (1983).

39. Kox, A. J., Michels, J. P. & Wiegel, F. W. Simulation of a lipid monolayer using

molecular dynamics. *Nature* **287**, 317–319 (1980).

40. Van Der Ploeg, P. & Berendsen, H. J. Molecular dynamics simulation of a bilayer membrane. *The Journal of Chemical Physics* **76**, 3271–3276 (1982).

41. Heller, H., Schaefer, M. & Schulten, K. Molecular dynamics simulation of a bilayer of 200 lipids in the gel and in the liquid-crystal phases. *Journal of Physical Chemistry* **97**, 8343–8360 (1993).

42. Tieleman, D. P., Marrink, S. J. & Berendsen, H. J. A computer perspective of membranes: Molecular dynamics studies of lipid bilayer systems. *Biochimica et Biophysica Acta - Reviews on Biomembranes* **1331**, 235–270 (1997).

43. Marrink, S. J., Berger, O., Tieleman, P. & Jähnig, F. Adhesion forces of lipids in a phospholipid membrane studied by molecular dynamics simulations. *Biophysical Journal* **74**, 931–943 (1998).

44. Zhong, Q., Jiang, Q., Moore, P. B., Newns, D. M. & Klein, M. L. Molecular dynamics simulation of a synthetic ion channel. *Biophysical Journal* **74**, 3–10 (1998).

45. Shrivastava, I. H. & Sansom, M. S. Simulations of ion permeation through a potassium channel: Molecular dynamics of KcsA in a phospholipid bilayer. *Biophysical Journal* **78**, 557–570 (2000).

46. Gumbart, J., Wang, Y., Aksimentiev, A., Tajkhorshid, E. & Schulten, K. Molecular dynamics simulations of proteins in lipid bilayers. *Current Opinion in Structural Biology* **15**, 423–431 (2005).

47. Lindahl, E. & Sansom, M. S. Membrane proteins: molecular dynamics simulations. *Current Opinion in Structural Biology* **18**, 425–431 (2008).

48. Kutzner, C., Grubmüller, H., De Groot, B. L. & Zachariae, U. Computational electrophysiology: The molecular dynamics of ion channel permeation and selectivity in atomistic detail. *Biophysical Journal* **101**, 809–817 (2011).

49. Ohkubo, Y. Z. & Tajkhorshid, E. Distinct Structural and Adhesive Roles of Ca2+ in Membrane Binding of Blood Coagulation Factors. *Structure* **16**, 72–81 (2008).

50. Rogaski, B. & Klauda, J. B. Membrane-binding mechanism of a peripheral membrane protein through microsecond molecular dynamics simulations. *Journal of Molecular Biology* **423**, 847–861 (2012).

51. Lai, C. L. *et al.* Molecular mechanism of membrane binding of the GRP1 PH domain. *Journal of Molecular Biology* **425**, 3073–3090 (2013).

52. Marrink, S. J., Risselada, H. J., Yefimov, S., Tieleman, D. P. & De Vries, A. H. The

MARTINI force field: Coarse grained model for biomolecular simulations. *Journal of Physical Chemistry B* **111**, 7812–7824 (2007).

53. Arkhipov, A., Yin, Y. & Schulten, K. Four-scale description of membrane sculpting by BAR domains. *Biophysical Journal* **95**, 2806–2821 (2008).

54. Wang, H., Lo, W. T. & Haucke, V. Phosphoinositide switches in endocytosis and in the endolysosomal system. *Current Opinion in Cell Biology* **59**, 50–57 (2019).

55. Roux, B. & Simonson, T. Implicit solvent models. *Biophysical Chemistry* **78**, 1–20 (1999).

56. Feig, M. & Brooks, C. L. Recent advances in the development and application of implicit solvent models in biomolecule simulations. *Current Opinion in Structural Biology* **14**, 217–224 (2004).

57. Arnarez, C. *et al.* Dry martini, a coarse-grained force field for lipid membrane simulations with implicit solvent. *Journal of Chemical Theory and Computation* **11**, 260–275 (2015).

58. Shi, Q., Izvekov, S. & Voth, G. A. Mixed atomistic and coarse-grained molecular dynamics: Simulation of a membrane-bound ion channel. *Journal of Physical Chemistry B* **110**, 15045–15048 (2006).

59. Silva, J. R. *et al.* A multiscale model linking ion-channel molecular dynamics and electrostatics to the cardiac action potential. *Proceedings of the National Academy of Sciences of the United States of America* **106**, 11102–11106 (2009).

60. Alessandri, R., Grünewald, F. & Marrink, S. J. The martini model in materials science. *arXiv* **arXiv:2012** (2020). arXiv:2012.07194.

61. Watts, J. F. & Wolstenholme, J. Electron Spectroscopy: Some Basic Concepts. In *An Introduction to Surface Analysis by XPS and AES*, 1–15 (John Wiley & Sons, Ltd, Chichester, UK, 2005).

62. Baio, J. E., Graham, D. J. & Castner, D. G. Surface analysis tools for characterizing biological materials. *Chemical Society Reviews* **49**, 3278–3296 (2020).

63. Mazzotta, E., Rella, S., Turco, A. & Malitesta, C. XPS in development of chemical sensors. *RSC Advances* **5**, 83164–83186 (2015).

64. Salmeron, M. & Schlögl, R. Ambient pressure photoelectron spectroscopy: A new tool for surface science and nanotechnology. *Surface Science Reports* **63**, 169–199 (2008).

65. Alberts, Bray, Hopkin, Johnson, Lewis, Raff, Roberts, W. *Essential Cell Biology*

SLEEEEET (Garland Science, 2014), 3 edn.

66. Sezgin, E., Levental, I., Mayor, S. & Eggeling, C. The mystery of membrane organization: Composition, regulation and roles of lipid rafts. *Nature Reviews Molecular Cell Biology* **18**, 361–374 (2017).

67. Zimmerberg, J. & Kozlov, M. M. How proteins produce cellular membrane curvature. *Nature Reviews Molecular Cell Biology* **7**, 9–19 (2006).

68. McMahon, H. T. & Gallop, J. L. Membrane curvature and mechanisms of dynamic cell membrane remodelling. *Nature* **438**, 590–596 (2005).

69. Hung, Y. F. *et al.* Dengue virus NS4A cytoplasmic domain binding to liposomes is sensitive to membrane curvature. *Biochimica et Biophysica Acta - Biomembranes* **1848**, 1119–1126 (2015).

70. Yao, H., Lee, M. W., Waring, A. J., Wong, G. C. & Hong, M. Viral fusion protein transmembrane domain adopts β-strand structure to facilitate membrane topological changes for virus-cell fusion. *Proceedings of the National Academy of Sciences of the United States of America* **112**, 10926–10931 (2015).

71. Schmidt, N. W., Mishra, A., Wang, J., Degrado, W. F. & Wong, G. C. Influenza virus A M2 protein generates negative gaussian membrane curvature necessary for budding and scission. *Journal of the American Chemical Society* **135**, 13710–13719 (2013).

72. Weise, K. *et al.* Membrane-mediated induction and sorting of K-Ras microdomain signaling platforms. *Journal of the American Chemical Society* **133**, 880–887 (2011).

73. Reynwar, B. J. *et al.* Aggregation and vesiculation of membrane proteins by curvature-mediated interactions. *Nature* **447**, 461–464 (2007).

74. Strahl, H. *et al.* Transmembrane protein sorting driven by membrane curvature. *Nature Communications* **6**, 8728 (2015).

75. Larsen, J. B. *et al.* Membrane curvature enables N-Ras lipid anchor sorting to liquid-ordered membrane phases. *Nature Chemical Biology* **11**, 192–194 (2015).

76. Hanna, M. G. *et al.* Sar1 GTPase activity is regulated by membrane curvature. *Journal of Biological Chemistry* **291**, 1014–1027 (2016).

77. Bassereau, P. *et al.* The 2018 biomembrane curvature and remodeling roadmap. *Journal of Physics D: Applied Physics* **51**, 343001 (2018).

78. Baumgart, T., Hess, S. T. & Webb, W. W. Imaging coexisting fluid domains in

biomembrane models coupling curvature and line tension. *Nature* **425**, 821–824 (2003).

79. Bacia, K., Schwille, P. & Kurzchalia, T. Sterol structure determines the separation of phases and the curvature of the liquid-ordered phase in model membranes. *Proceedings of the National Academy of Sciences of the United States of America* **102**, 3272–3277 (2005).

80. Jarsch, I. K., Daste, F. & Gallop, J. L. Membrane curvature in cell biology: An integration of molecular mechanisms. *Journal of Cell Biology* **214**, 375–387 (2016).

81. Kooijman, E. E. *et al.* Spontaneous curvature of phosphatidic acid and lysophosphatidic acid. *Biochemistry* **44**, 2097–2102 (2005).

82. Roux, A. *et al.* Role of curvature and phase transition in lipid sorting and fission of membrane tubules. *EMBO Journal* **24**, 1537–1545 (2005).

83. Callan-Jones, A., Sorre, B. & Bassereau, P. Curvature-driven lipid sorting in biomembranes. *Cold Spring Harbor Perspectives in Biology* **3**, 1–14 (2011).

84. Koldsø, H., Shorthouse, D., Hélie, J. & Sansom, M. S. Lipid Clustering Correlates with Membrane Curvature as Revealed by Molecular Simulations of Complex Lipid Bilayers. *PLoS Computational Biology* **10**, e1003911 (2014).

85. Vanni, S., Hirose, H., Barelli, H., Antonny, B. & Gautier, R. A sub-nanometre view of how membrane curvature and composition modulate lipid packing and protein recruitment. *Nature Communications* **5**, 4916 (2014).

86. Black, J. C., Cheney, P. P., Campbell, T. & Knowles, M. K. Membrane curvature based lipid sorting using a nanoparticle patterned substrate. *Soft Matter* **10**, 2016–2023 (2014).

87. Tonnesen, A., Christensen, S. M., Tkach, V. & Stamou, D. Geometrical membrane curvature as an allosteric regulator of membrane protein structure and function. *Biophysical Journal* **106**, 201–209 (2014).

88. Rosholm, K. R. *et al.* Membrane curvature regulates ligand-specific membrane sorting of GPCRs in living cells. *Nature Chemical Biology* **13**, 724–729 (2017).

89. Kaksonen, M. & Roux, A. Mechanisms of clathrin-mediated endocytosis. *Nature Reviews Molecular Cell Biology* **19**, 313–326 (2018).

90. Skruzny, M. *et al.* Molecular basis for coupling the plasma membrane to the actin cytoskeleton during clathrin-mediated endocytosis. *Proceedings of the National Academy of Sciences of the United States of America* **109**, E2533–E2542 (2012).

91. Kaksonen, M., Toret, C. P. & Drubin, D. G. Harnessing actin dynamics for clathrin-mediated endocytosis. *Nature Reviews Molecular Cell Biology* **7**, 404–414 (2006).

92. McMahon, H. T. & Boucrot, E. Membrane curvature at a glance. *Journal of Cell Science* **128**, 1065–1070 (2015).

93. Stachowiak, J. C. *et al.* Membrane bending by protein-protein crowding. *Nature Cell Biology* **14**, 944–949 (2012).

94. Busch, D. J. *et al.* Intrinsically disordered proteins drive membrane curvature. *Nature Communications* **6**, 7875 (2015).

95. Conner, S. D. & Schmid, S. L. Regulated portals of entry into the cell. *Nature* **422**, 37–44 (2003).

96. Varkouhi, A. K., Scholte, M., Storm, G. & Haisma, H. J. Endosomal escape pathways for delivery of biologicals. *Journal of Controlled Release* **151**, 220–228 (2011).

97. Roux, A. *et al.* Membrane curvature controls dynamin polymerization. *Proceedings of the National Academy of Sciences of the United States of America* **107**, 4141–4146 (2010).

98. Ferguson, S. M. & De Camilli, P. Dynamin, a membrane-remodelling GTPase. *Nature Reviews Molecular Cell Biology* **13**, 75–88 (2012). arXiv:NIHMS150003.

99. Larson, B. T., Sochacki, K. A., Kindem, J. M. & Taraska, J. W. Systematic spatial mapping of proteins at exocytic and endocytic structures. *Molecular Biology of the Cell* **25**, 2084–2093 (2014).

100. Picco, A., Mund, M., Ries, J., Nédélec, F. & Kaksonen, M. Visualizing the functional architecture of the endocytic machinery. *eLife* **4**, e04535 (2015).

101. Sochacki, K. A., Dickey, A. M., Strub, M. P. & Taraska, J. W. Endocytic proteins are partitioned at the edge of the clathrin lattice in mammalian cells. *Nature Cell Biology* **19**, 352–361 (2017).

102. Habermann, B. The BAR-domain family of proteins: A case of bending and binding? *EMBO Reports* **5**, 250–255 (2004).

103. Frost, A. *et al.* Structural Basis of Membrane Invagination by F-BAR Domains. *Cell* **132**, 807–817 (2008).

104. Mim, C. *et al.* Structural basis of membrane bending by the N-BAR protein endophilin. *Cell* **149**, 137–145 (2012).

105. Sorre, B. *et al.* Nature of curvature coupling of amphiphysin with membranes depends on its bound density. *Proceedings of the National Academy of Sciences of the*

United States of America **109**, 173–178 (2012).

106. Yin, Y., Arkhipov, A. & Schulten, K. Simulations of Membrane Tubulation by Lattices of Amphiphysin N-BAR Domains. *Structure* **17**, 882–892 (2009).

107. Yu, H. & Schulten, K. Membrane Sculpting by F-BAR Domains Studied by Molecular Dynamics Simulations. *PLoS Computational Biology* **9** (2013).

108. Ford, M. G. *et al.* Simultaneous binding of PtdIns (4,5) P2 and clathrin by AP180 in the nucleation of clathrin lattices on membranes. *Science* **291**, 1051–1055 (2001).

109. Ford, M. G. *et al.* Curvature of clathrin-coated pits driven by epsin. *Nature* **419**, 361–366 (2002).

110. Gruenberg, J. Lipids in endocytic membrane transport and sorting. *Current Opinion in Cell Biology* **15**, 382–388 (2003).

111. Zoncu, R. *et al.* Loss of endocytic clathrin-coated pits upon acute depletion of phosphatidylinositol 4,5-bisphosphate. *Proceedings of the National Academy of Sciences of the United States of America* **104**, 3793–3798 (2007).

112. Posor, Y. *et al.* Spatiotemporal control of endocytosis by phosphatidylinositol-3,4-bisphosphate. *Nature* **499**, 233–237 (2013).

113. Di Paolo, G. & De Camilli, P. Phosphoinositides in cell regulation and membrane dynamics. *Nature* **443**, 651–657 (2006).

114. Belessiotis-Richards, A., Higgins, S. G., Sansom, M. S., Alexander-Katz, A. & Stevens, M. M. Coarse-Grained Simulations Suggest the Epsin N-Terminal Homology Domain Can Sense Membrane Curvature without Its Terminal Amphipathic Helix. *ACS Nano* **14**, 16919–16928 (2020).

115. Helfrich, W. Elastic Properties of Lipid Bilayers: Theory and Possible Experiments. *Zeitschrift fur Naturforschung - Section C Journal of Biosciences* **28**, 693–703 (1973).

116. Lipowsky, R. The conformation of membranes. *Nature* **349**, 475–481 (1991).

117. Kroll, D. M. & Gompper, G. The conformation of fluid membranes: Monte Carlo simulations. *Science* **255**, 968–971 (1992).

118. Jülicher, F. & Lipowsky, R. Domain-induced budding of vesicles. *Physical Review Letters* **70**, 2964–2967 (1993).

119. Deserno, M. & Gelbart, W. M. Adhesion and wrapping in colloid-vesicle complexes. *Journal of Physical Chemistry B* **106**, 5543–5552 (2002).

120. Bahrami, A. H., Lipowsky, R. & Weikl, T. R. Tubulation and aggregation of spherical

nanoparticles adsorbed on vesicles. *Physical Review Letters* **109**, 188102 (2012).

121. Paulose, J., Vliegenthart, G. A., Gompper, G. & Nelson, D. R. Fluctuating shells under pressure. *Proceedings of the National Academy of Sciences of the United States of America* **109**, 19551–19556 (2012). arXiv:1210.3704.

122. Bahrami, A. H. & Hummer, G. Formation and Stability of Lipid Membrane Nanotubes. *ACS Nano* **11**, 9558–9565 (2017).

123. Liu, J., Sun, Y., Drubin, D. G. & Oster, G. F. The mechanochemistry of endocytosis. *PLoS Biology* **7**, e1000204 (2009).

124. Agrawal, N. J., Nukpezah, J. & Radhakrishnan, R. Minimal mesoscale model for protein-mediated vesiculation in clathrin-dependent endocytosis. *PLoS Computational Biology* **6**, e1000926 (2010).

125. Pezeshkian, W. *et al.* Membrane invagination induced by Shiga toxin B-subunit: From molecular structure to tube formation. *Soft Matter* **12**, 5164–5171 (2016).

126. Hassinger, J. E., Oster, G., Drubin, D. G. & Rangamani, P. Design principles for robust vesiculation in clathrin-mediated endocytosis. *Proceedings of the National Academy of Sciences of the United States of America* **114**, E1118–E1127 (2017).

127. Akamatsu, M. *et al.* Principles of self-organization and load adaptation by the actin cytoskeleton during clathrin-mediated endocytosis. *eLife* **9**, e49840 (2020).

128. Dasgupta, S., Auth, T. & Gompper, G. Shape and orientation matter for the cellular uptake of nonspherical particles. *Nano Letters* **14**, 687–693 (2014).

129. Egberts, E., Marrink, S. J. & Berendsen, H. J. Molecular dynamics simulation of a phospholipid membrane. *European Biophysics Journal* **22**, 423–436 (1994).

130. Marrink, S. J. & Berendsen, H. J. Simulation of water transport through a lipid membrane. *Journal of Physical Chemistry* **98**, 4155–4168 (1994).

131. Ayton, G. S. & Voth, G. A. Hybrid coarse-graining approach for lipid bilayers at large length and time scales. *Journal of Physical Chemistry B* **113**, 4413–4424 (2009).

132. Laradji, M. & Kumar, P. B. Dynamics of domain growth in self-assembled fluid vesicles. *Physical Review Letters* **93**, 198105 (2004).

133. McWhirter, J. L., Ayton, G. & Voth, G. A. Coupling field theory with mesoscopic dynamical simulations of multicomponent lipid bilayers. *Biophysical Journal* **87**, 3242–3263 (2004).

134. Camley, B. A. & Brown, F. L. Dynamic simulations of multicomponent lipid membranes over long length and time scales. *Physical Review Letters* **105**, 148102 (2010).

arXiv:1105.4898.

135. Spangler, E. J., Sunil Kumar, P. B. & Laradji, M. Anomalous freezing behavior of nanoscale liposomes. *Soft Matter* **8**, 10896–10904 (2012).

136. Siggel, M., Bhaskara, R. M. & Hummer, G. Phospholipid Scramblases Remodel the Shape of Asymmetric Membranes. *Journal of Physical Chemistry Letters* **10**, 6351–6354 (2019).

137. Noguchi, H. & Takasu, M. Adhesion of nanoparticles to vesicles: A Brownian dynamics simulation. *Biophysical Journal* **83**, 299–308 (2002).

138. Šarić, A. & Cacciuto, A. Mechanism of membrane tube formation induced by adhesive nanocomponents. *Physical Review Letters* **109**, 188101 (2012). arXiv:1206.3528.

139. Bahrami, A. H. Orientational changes and impaired internalization of ellipsoidal nanoparticles by vesicle membranes. *Soft Matter* **9**, 8642–8646 (2013).

140. Dasgupta, S., Auth, T. & Gompper, G. Wrapping of ellipsoidal nano-particles by fluid membranes. *Soft Matter* **9**, 5473–5482 (2013). arXiv:1303.5567.

141. Van Lehn, R. C. & Alexander-Katz, A. Penetration of lipid bilayers by nanoparticles with environmentally- responsive surfaces: Simulations and theory. *Soft Matter* **7**, 11392–11404 (2011).

142. Vácha, R., Martinez-Veracoechea, F. J. & Frenkel, D. Receptor-mediated endocytosis of nanoparticles of various shapes. *Nano Letters* **11**, 5391–5395 (2011).

143. Lin, J. & Alexander-Katz, A. Cell membranes open "doors" for cationic nanoparticles/ biomolecules: Insights into uptake kinetics. *ACS Nano* **7**, 10799–10808 (2013).

144. Huang, C., Zhang, Y., Yuan, H., Gao, H. & Zhang, S. Role of nanoparticle geometry in endocytosis: Laying down to stand up. *Nano Letters* **13**, 4546–4550 (2013).

145. Dasgupta, N. P. *et al.* 25th anniversary article: Semiconductor nanowires - Synthesis, characterization, and applications. *Advanced Materials* **26**, 2137–2184 (2014).

146. Shen, Z., Ye, H. & Li, Y. Understanding receptor-mediated endocytosis of elastic nanoparticles through coarse grained molecular dynamic simulation. *Physical Chemistry Chemical Physics* **20**, 16372–16385 (2018).

147. Shen, Z., Ye, H., Yi, X. & Li, Y. Membrane Wrapping Efficiency of Elastic Nanoparticles during Endocytosis: Size and Shape Matter. *ACS Nano* **13**, 215–228 (2019).

148. Blood, P. D. & Voth, G. A. Direct observation of Bin/amphiphysin/Rvs (BAR) domain-induced membrane curvature by means of molecular dynamics simulations.

Proceedings of the National Academy of Sciences of the United States of America **103**, 15068–15072 (2006).

149. Blood, P. D., Swenson, R. D. & Voth, G. A. Factors influencing local membrane curvature induction by N-BAR domains as revealed by molecular dynamics simulations. *Biophysical Journal* **95**, 1866–1876 (2008).

150. Arkhipov, A., Yin, Y. & Schulten, K. Four-scale description of membrane sculpting by BAR domains. *Biophysical Journal* **95**, 2806–2821 (2008).

151. Arkhipov, A., Yin, Y. & Schulten, K. Membrane-bending mechanism of amphiphysin N-BAR domains. *Biophysical Journal* **97**, 2727–2735 (2009).

152. Braun, A. R., Lacy, M. M., Ducas, V. C., Rhoades, E. & Sachs, J. N. A-Synuclein-Induced Membrane Remodeling Is Driven By Binding Affinity, Partition Depth, and Interleaflet Order Asymmetry. *Journal of the American Chemical Society* **136**, 9962–9972 (2014).

153. Takemura, K., Hanawa-Suetsugu, K., Suetsugu, S. & Kitao, A. Salt Bridge Formation between the I-BAR Domain and Lipids Increases Lipid Density and Membrane Curvature. *Scientific Reports* **7**, 6808 (2017).

154. Simunovic, M., Šarić, A., Henderson, J. M., Lee, K. Y. C. & Voth, G. A. Long-Range Organization of Membrane-Curving Proteins. *ACS Central Science* **3**, 1246–1253 (2017).

155. Mahmood, M. I., Noguchi, H. & ichi Okazaki, K. Curvature induction and sensing of the F-BAR protein Pacsin1 on lipid membranes via molecular dynamics simulations. *Scientific Reports* **9**, 14557 (2019).

156. Lai, C. L. *et al.* Membrane Binding and Self-Association of the Epsin N-Terminal Homology Domain. *Journal of Molecular Biology* **423**, 800–817 (2012).

157. Bradley, R. P. & Radhakrishnan, R. Curvature-undulation coupling as a basis for curvature sensing and generation in bilayer membranes. *Proceedings of the National Academy of Sciences of the United States of America* **113**, E5117–E5124 (2016).

158. Nepal, B., Leveritt, J. & Lazaridis, T. Membrane Curvature Sensing by Amphipathic Helices: Insights from Implicit Membrane Modeling. *Biophysical Journal* **114**, 2128–2141 (2018).

159. Belessiotis-Richards, A., Higgins, S. G., Butterworth, B., Stevens, M. M. & Alexander-Katz, A. Single-Nanometer Changes in Nanopore Geometry Influence Curvature, Local Properties, and Protein Localization in Membrane Simulations. *Nano Letters* **19**, 4770–4778 (2019).

160. Hsin, J. *et al.* Protein-induced membrane curvature investigated through molecular dynamics flexible fitting. *Biophysical Journal* **97**, 321–329 (2009).

161. Chandler, D. E., Gumbart, J., Stack, J. D., Chipot, C. & Schulten, K. Membrane curvature induced by aggregates of LH2s and monomeric LH1s. *Biophysical Journal* **97**, 2978–2984 (2009).

162. Yue, T., Li, S., Zhang, X. & Wang, W. The relationship between membrane curvature generation and clustering of anchored proteins: A computer simulation study. *Soft Matter* **6**, 6109–6118 (2010).

163. Martinez, J. O. *et al.* Engineering multi-stage nanovectors for controlled degradation andtunable release kinetics. *Biomaterials* **34**, 8469–8477 (2013).

164. Vandersarl, J. J., Xu, A. M. & Melosh, N. A. Nanostraws for direct fluidic intracellular access. *Nano Letters* **12**, 3881–3886 (2012).

165. Shalek, A. K. *et al.* Nanowire-mediated delivery enables functional interrogation of primary immune cells: Application to the analysis of chronic lymphocytic leukemia. *Nano Letters* **12**, 6498–6504 (2012).

166. Wang, Y. *et al.* Poking cells for efficient vector-free intracellular delivery. *Nature Communications* **5**, 4466 (2014).

167. Shalek, A. K. *et al.* Vertical silicon nanowires as a universal platform for delivering biomolecules into living cells. *Proceedings of the National Academy of Sciences of the United States of America* **107**, 1870–1875 (2010).

168. Trimmer, W. *et al.* Injection of DNA into plant and animal tissues with micromechanical piercing structures. *Proceedings of the IEEE Micro Electro Mechanical Systems* **2**, 111–115 (1995).

169. Reed, M. L. *et al.* Micromechanical devices for intravascular drug delivery. *Journal of Pharmaceutical Sciences* **87**, 1387–1394 (1998).

170. Ita, K. Transdermal delivery of drugs with microneedles: Strategies and outcomes. *Journal of Drug Delivery Science and Technology* **29**, 16–23 (2015).

171. Kim, B. H. & Seo, Y. H. Transdermal Drug Delivery Devices Based on Microneedles: A Review. *Journal of mucopolysaccharidosis and rare disease* **1**, 5–14 (2015).

172. Higgins, S. G. *et al.* High-Aspect-Ratio Nanostructured Surfaces as Biological Metamaterials. *Advanced Materials* **32**, 1903862 (2020).

173. Xie, X. *et al.* Nanostraw-electroporation system for highly efficient intracellular delivery and transfection. *ACS Nano* **7**, 4351–4358 (2013).

174. Xu, A. M. *et al.* Quantification of nanowire penetration into living cells. *Nature Communications* **5**, 3613 (2014).

175. Xu, A. M., Kim, S. A., Wang, D. S., Aalipour, A. & Melosh, N. A. Temporally resolved direct delivery of second messengers into cells using nanostraws. *Lab on a Chip* **16**, 2434–2439 (2016).

176. Xu, A. M., Wang, D. S., Shieh, P., Cao, Y. & Melosh, N. A. Direct Intracellular Delivery of Cell-Impermeable Probes of Protein Glycosylation by Using Nanostraws. *ChemBioChem* **18**, 623–628 (2017).

177. Willander, M. & Al-Hilli, S. ZnO nanorods as an intracellular sensor for pH measurements. *Methods in molecular biology (Clifton, N.J.)* **544**, 187–200 (2009).

178. Na, Y. R. *et al.* Probing enzymatic activity inside living cells using a nanowire-cell "sandwich" assay. *Nano Letters* **13**, 153–158 (2013).

179. Berthing, T. *et al.* Intact mammalian cell Function on semiconductor nanowire arrays: New perspectives for cell-based biosensing. *Small* **7**, 640–647 (2011).

180. Chiappini, C. *et al.* Mapping Local Cytosolic Enzymatic Activity in Human Esophageal Mucosa with Porous Silicon Nanoneedles. *Advanced Materials* **27**, 5147–5152 (2015).

181. Fromherz, P. & Voelker, M. Comment on "detection, stimulation, and inhibition of neuronal signals with high-density nanowire transistor arrays". *Science* **323**, 1100–1104 (2009).

182. Xie, C. *et al.* Noninvasive neuron pinning with nanopillar arrays. *Nano Letters* **10**, 4020–4024 (2010).

183. Timko, B. P. *et al.* Electrical recording from hearts with flexible nanowire device arrays. *Nano Letters* **9**, 914–918 (2009).

184. Timko, B. P., Cohen-Karni, T., Qing, Q., Tian, B. & Lieber, C. M. Design and implementation of functional nanoelectronic interfaces with biomolecules, cells, and tissue using nanowire device arrays. *IEEE Transactions on Nanotechnology* **9**, 269–280 (2010).

185. Hanson, L., Lin, Z. C., Xie, C., Cui, Y. & Cui, B. Characterization of the cell-nanopillar interface by transmission electron microscopy. *Nano Letters* **12**, 5815–5820 (2012).

186. Berthing, T. *et al.* Cell membrane conformation at vertical nanowire array interface revealed by fluorescence imaging. *Nanotechnology* **23**, 415102 (2012).

187. Mumm, F., Beckwith, K. M., Bonde, S., Martinez, K. L. & Sikorski, P. A transparent nanowire-based cell impalement device suitable for detailed cell-nanowire interaction studies. *Small* **9**, 263–272 (2013).

188. Qi, S., Yi, C., Ji, S., Fong, C. C. & Yang, M. Cell adhesion and spreading behavior on vertically aligned silicon nanowire arrays. *ACS Applied Materials and Interfaces* **1**, 30–34 (2009).

189. Kim, W., Ng, J. K., Kunitake, M. E., Conklin, B. R. & Yang, P. Interfacing silicon nanowires with mammalian cells. *Journal of the American Chemical Society* **129**, 7228–7229 (2007).

190. Gopal, S. *et al.* Porous Silicon Nanoneedles Modulate Endocytosis to Deliver Biological Payloads. *Advanced Materials* **31**, 1806788 (2019).

191. Hansel, C. S. *et al.* Nanoneedle-Mediated Stimulation of Cell Mechanotransduction Machinery. *ACS Nano* **13**, 2913–2926 (2019).

192. Galic, M. *et al.* External push and internal pull forces recruit curvature-sensing N-BAR domain proteins to the plasma membrane. *Nature Cell Biology* **14**, 874–881 (2012). arXiv:NIHMS150003.

193. Zhao, W. *et al.* Nanoscale manipulation of membrane curvature for probing endocytosis in live cells. *Nature Nanotechnology* **12**, 750–756 (2017).

194. Lou, H. Y. *et al.* Membrane curvature underlies actin reorganization in response to nanoscale surface topography. *Proceedings of the National Academy of Sciences of the United States of America* **116**, 23143–23151 (2019).

195. Pieuchot, L. *et al.* Curvotaxis directs cell migration through cell-scale curvature landscapes. *Nature Communications* **9**, 3995 (2018).

196. Zhao, W. *et al.* Nanoscale manipulation of membrane curvature for probing endocytosis in live cells. *Nature Nanotechnology* **12**, 750–756 (2017).

197. Xie, X. *et al.* Mechanical model of vertical nanowire cell penetration. *Nano Letters* **13**, 6002–6008 (2013).

198. Xie, X., Aalipour, A., Gupta, S. V. & Melosh, N. A. Determining the Time Window for Dynamic Nanowire Cell Penetration Processes. *ACS Nano* **9**, 11667–11677 (2015).

199. Bonde, S. *et al.* Tuning InAs nanowire density for HEK293 cell viability, adhesion, and morphology: Perspectives for nanowire-based biosensors. *ACS Applied Materials and Interfaces* **5**, 10510–10519 (2013).

200. Bonde, S., Bolinsson, J., Berthing, T. & Martinez, K. L. Towards a better prediction of cell settling on nanostructure arrays - Simple means to complicated ends. *Advanced Functional Materials* **25**, 3246–3255 (2015).

201. Zhou, J. *et al.* The effects of surface topography of nanostructure arrays on cell adhesion. *Physical Chemistry Chemical Physics* **20**, 22946–22951 (2018).

202. Capozza, R. *et al.* Cell Membrane Disruption by Vertical Micro-/Nanopillars: Role of Membrane Bending and Traction Forces. *ACS Applied Materials and Interfaces* **10**, 29107–29114 (2018).

203. Park, J., Bauer, S., Von Der Mark, K. & Schmuki, P. Nanosize and vitality: TiO2 nanotube diameter directs cell fate. *Nano Letters* **7**, 1686–1691 (2007).

204. Agrawal, A. A. *et al.* Porous nanocrystalline silicon membranes as highly permeable and molecularly thin substrates for cell culture. *Biomaterials* **31**, 5408–5417 (2010).

205. Vetrone, F. *et al.* Nanoscale oxidative patterning of metallic surfaces to modulate cell activity and fate. *Nano Letters* **9**, 659–665 (2009).

206. Popat, K. C. *et al.* Influence of nanoporous alumina membranes on long-term osteoblast response. *Biomaterials* **26**, 4516–4522 (2005).

207. Park, J. *et al.* TiO2 nanotube surfaces: 15 nm - an optimal length scale of surface topography for cell adhesion and differentiation. *Small* **5**, 666–671 (2009).

208. Wang, S., Kowal, T. J., Marei, M. K., Falk, M. M. & Jain, H. Nanoporosity significantly enhances the biological performance of engineered glass tissue scaffolds. *Tissue Engineering - Part A* **19**, 1632–1640 (2013).

209. Guadarrama Bello, D., Fouillen, A., Badia, A. & Nanci, A. A nanoporous titanium surface promotes the maturation of focal adhesions and formation of filopodia with distinctive nanoscale protrusions by osteogenic cells. *Acta Biomaterialia* **60**, 339–349 (2017).

210. Chen, Z. *et al.* Nanoporous microstructures mediate osteogenesis by modulating the osteo-immune response of macrophages. *Nanoscale* **9**, 706–718 (2017).

211. Chapman, C. A. *et al.* Nanoporous gold as a neural interface coating: Effects of topography, surface chemistry, and feature size. *ACS Applied Materials and Interfaces* **7**, 7093–7100 (2015).

212. Bradley, R. & Radhakrishnan, R. Coarse-grained models for protein-cell membrane interactions. *Polymers* **5**, 890–936 (2013).

213. Ramakrishnan, N., Bradley, R. P., Tourdot, R. W. & Radhakrishnan, R. Biophysics of

membrane curvature remodeling at molecular and mesoscopic lengthscales. *Journal of Physics Condensed Matter* **30**, 273001 (2018).

214. Agudo-Canalejo, J. & Discher, D. E. Biomembrane Adhesion to Substrates Topographically Patterned with Nanopits. *Biophysical Journal* **115**, 1292–1306 (2018).

215. Hess, B., Kutzner, C., Van Der Spoel, D. & Lindahl, E. GRGMACS 4: Algorithms for highly efficient, load-balanced, and scalable molecular simulation. *Journal of Chemical Theory and Computation* **4**, 435–447 (2008). arXiv:0701253.

216. Humphrey, W., Dalke, A. & Schulten, K. VMD: Visual molecular dynamics. *Journal of Molecular Graphics* **14**, 33–38 (1996). arXiv:arXiv:1503.05249v1.

217. Michaud-Agrawal, N., Denning, E. J., Woolf, T. B. & Beckstein, O. MDAnalysis: A toolkit for the analysis of molecular dynamics simulations. *Journal of Computational Chemistry* **32**, 2319–2327 (2011). arXiv:NIHMS150003.

218. Wassenaar, T. A., Ingólfsson, H. I., Böckmann, R. A., Tieleman, D. P. & Marrink, S. J. Computational lipidomics with insane: A versatile tool for generating custom membranes for molecular simulations. *Journal of Chemical Theory and Computation* **11**, 2144–2155 (2015).

219. Hjorth Larsen, A. *et al.* The atomic simulation environment - A Python library for working with atoms. *Journal of Physics Condensed Matter* **29**, 273002 (2017).

220. Cremer, P. S. & Boxer, S. G. Formation and spreading of lipid bilayers on planar glass supports. *Journal of Physical Chemistry B* **103**, 2554–2559 (1999).

221. Nollert, P., Kiefer, H. & Jähnig, F. Lipid vesicle adsorption versus formation of planar bilayers on solid surfaces. *Biophysical Journal* **69**, 1447–1455 (1995).

222. Rizwan, M., Tse, J. W., Nori, A., Leong, K. W. & Yim, E. K. F. Chapter 27 - Cell–Substrate Interactions. In Atala, A., Lanza, R., Mikos, A. G. & Nerem, R. B. T. P. o. R. M. T. E. (eds.) *Principles of Regenerative Medicine (Third Edition)*, 437–468 (Academic Press, Boston, 2019).

223. Huang, Z., Geyer, N., Werner, P., De Boor, J. & Gösele, U. Metal-assisted chemical etching of silicon: A review. *Advanced Materials* **23**, 285–308 (2011).

224. Whitney, A. V., Myers, B. D. & Van Duyne, R. P. Sub-100 nm triangular nanopores fabricated with the reactive ion etching variant of nanosphere lithography and angle-resolved nanosphere lithography. *Nano Letters* **4**, 1507–1511 (2004).

225. Kučerka, N., Nieh, M. P. & Katsaras, J. Fluid phase lipid areas and bilayer thicknesses of commonly used phosphatidylcholines as a function of temperature. *Biochimica et Biophysica Acta - Biomembranes* **1808**, 2761–2771 (2011).

226. Reddy, A. S., Warshaviak, D. T. & Chachisvilis, M. Effect of membrane tension on the physical properties of DOPC lipid bilayer membrane. *Biochimica et Biophysica Acta - Biomembranes* **1818**, 2271–2281 (2012).

227. Strahl, H. *et al.* Transmembrane protein sorting driven by membrane curvature. *Nature Communications* **6**, 8728 (2015).

228. Schütte, O. M. *et al.* Size and mobility of lipid domains tuned by geometrical constraints. *Proceedings of the National Academy of Sciences of the United States of America* **114**, E6064–E6071 (2017).

229. Mitra, K., Ubarretxena-Belandia, I., Taguchi, T., Warren, G. & Engelman, D. M. Modulation of the bilayer thickness of exocytic pathway membranes by membrane proteins rather than cholesterol. *Proceedings of the National Academy of Sciences of the United States of America* **101**, 4083–4088 (2004).

230. Andersen, O. S. & Koeppe, R. E. Bilayer thickness and membrane protein function: An energetic perspective. *Annual Review of Biophysics and Biomolecular Structure* **36**, 107–130 (2007).

231. Jakobsson, J. *et al.* Role of epsin 1 in synaptic vesicle endocytosis. *Proceedings of the National Academy of Sciences of the United States of America* **105**, 6445–6450 (2008).

232. Messa, M. *et al.* Epsin deficiency impairs endocytosis by stalling the actin-dependent invagination of endocytic clathrin-coated pits. *eLife* **3**, 1–25 (2014).

233. Chen, H. *et al.* Epsin is an EH-domain-binding protein implicated in clathrin-mediated endocytosis. *Nature* **394**, 793–797 (1998). arXiv:9810036.

234. Capraro, B. R., Yoon, Y., Cho, W. & Baumgart, T. Curvature sensing by the epsin N-terminal homology domain measured on cylindrical lipid membrane tethers. *Journal of the American Chemical Society* **132**, 1200–1201 (2010).

235. Wu, Q. Y. & Liang, Q. Interplay between curvature and lateral organization of lipids and peptides/proteins in model membranes. *Langmuir* **30**, 1116–1122 (2014).

236. Antonescu, C. N., Aguet, F., Danuser, G. & Schmid, S. L. Phosphatidylinositol-(4,5)-bisphosphate regulates clathrin-coated pit initiation, stabilization, and size. *Molecular Biology of the Cell* **22**, 2588–2600 (2011).

237. Schöneberg, J. *et al.* Lipid-mediated PX-BAR domain recruitment couples local membrane constriction to endocytic vesicle fission. *Nature Communications* **8**, 15873 (2017).

238. Scott, B. L. *et al.* Membrane bending occurs at all stages of clathrincoat assembly

and defines endocytic dynamics. *Nature Communications* **9**, 273 (2018).

239. Capraro, B. R., Yoon, Y., Cho, W. & Baumgart, T. Curvature sensing by the epsin N-terminal homology domain measured on cylindrical lipid membrane tethers. *Journal of the American Chemical Society* **132**, 1200–1201 (2010). arXiv:NIHMS150003.

240. Itoh, T. *et al.* Role of the ENTH domain in phosphatidylinositol-4,5-bisphosphate binding and endocytosis. *Science* **291**, 1047–1051 (2001).

241. De Camilli, P. *et al.* The ENTH domain. *FEBS Letters* **513**, 11–18 (2002).

242. Furuya, T. *et al.* Nanotubules formed by highly hydrophobic amphiphilic α-helical peptides and natural phospholipids. *Biophysical Journal* **84**, 1950–1959 (2003).

243. Campelo, F., McMahon, H. T. & Kozlov, M. M. The hydrophobic insertion mechanism of membrane curvature generation by proteins. *Biophysical Journal* **95**, 2325–2339 (2008).

244. Drin, G. & Antonny, B. Amphipathic helices and membrane curvature. *FEBS Letters* **584**, 1840–1847 (2010).

245. Harries, D., Ben-Shaul, A. & Szleifer, I. Enveloping of charged proteins by lipid bilayers. *Journal of Physical Chemistry B* **108**, 1491–1496 (2004).

246. Strandberg, E., Zerweck, J., Wadhwani, P. & Ulrich, A. S. Synergistic insertion of antimicrobial magainin-Family peptides in membranes depends on the lipid spontaneous curvature. *Biophysical Journal* **104**, L9–L11 (2013).

247. Perrin, B. S., Sodt, A. J., Cotten, M. L. & Pastor, R. W. The Curvature Induction of Surface-Bound Antimicrobial Peptides Piscidin 1 and Piscidin 3 Varies with Lipid Chain Length. *Journal of Membrane Biology* **248**, 455–467 (2015).

248. Chen, Z., Zhu, C., Kuo, C. J., Robustelli, J. & Baumgart, T. The N-Terminal Amphipathic Helix of Endophilin Does Not Contribute to Its Molecular Curvature Generation Capacity. *Journal of the American Chemical Society* **138**, 14616–14622 (2016).

249. Zeno, W. F. *et al.* Molecular mechanisms of membrane curvature sensing by a disordered protein. *Journal of the American Chemical Society* **141**, 10361–10371 (2019).

250. Mu, L. *et al.* A phosphatidylinositol 4,5-bisphosphate redistribution-based sensing mechanism initiates a phagocytosis programing. *Nature Communications* **9**, 4259 (2018).

251. Lou, H. Y. *et al.* Membrane curvature underlies actin reorganization in response to nanoscale surface topography. *Proceedings of the National Academy of Sciences of the United States of America* **116**, 23143–23151 (2019).

252. Gleisner, M. *et al.* Driving a planar model system into the 3rd dimension: Generation and control of curved pore-spanning membrane arrays. *Soft Matter* **10**, 6228–6236 (2014).

253. Tebar, F., Bohlander, S. K. & Sorkin, A. Clathrin assembly lymphoid myeloid leukemia (CALM) protein: Localization in endocytic-coated pits, interactions with clathrin, and the impact of overexpression on clathrin-mediated traffic. *Molecular Biology of the Cell* **10**, 2687–2702 (1999).

254. Goode, B. L., Eskin, J. A. & Wendland, B. Actin and endocytosis in budding yeast. *Genetics* **199**, 315–358 (2014).

255. Kaneda, M. *et al.* Plant AP180 N-terminal homolog proteins are involved in clathrin-dependent endocytosis during pollen tube growth in arabidopsis thaliana. *Plant and Cell Physiology* **60**, 1316–1330 (2019).

256. Legendre-Guillemin, V., Wasiak, S., Hussain, N. K., Angers, A. & McPherson, P. S. ENTH/ANTH proteins and clathrin-mediated membrane budding. *Journal of Cell Science* **117**, 9–18 (2004).

257. Garcia-Alai, M. M. *et al.* Epsin and Sla2 form assemblies through phospholipid interfaces. *Nature Communications* **9**, 1–13 (2018).

258. Traub, L. M. Tickets to ride: Selecting cargo for clathrin-regulated internalization. *Nature Reviews Molecular Cell Biology* **10**, 583–596 (2009).

259. Petralia, R. S. *et al.* Reduction of AP180 and CALM produces defects in synaptic vesicle size and density. *NeuroMolecular Medicine* **15**, 49–60 (2013).

260. Koo, S. J. *et al.* Vesicular Synaptobrevin/VAMP2 Levels Guarded by AP180 Control Efficient Neurotransmission. *Neuron* **88**, 330–344 (2015).

261. Miller, S. E. *et al.* CALM Regulates Clathrin-Coated Vesicle Size and Maturation by Directly Sensing and Driving Membrane Curvature. *Developmental Cell* **33**, 163–175 (2015).

262. Bhatia, V. K. *et al.* Screening the Sensing of Membrane Curvature by BAR domains on Single Liposome Arrays. *Biophysical Journal* **96**, 570a (2009).

263. Haucke, V. & Kozlov, M. M. Membrane remodeling in clathrin-mediated endocytosis. *Journal of Cell Science* **131**, jcs216812 (2018).

264. Brod, J., Hellwig, A. & Wieland, F. T. Epsin but not AP-2 supports reconstitution of endocytic clathrin-coated vesicles. *FEBS Letters* **594**, 2227–2239 (2020).

265. Boucrot, E. *et al.* Membrane fission is promoted by insertion of amphipathic helices

and is restricted by crescent BAR domains. *Cell* **149**, 124–136 (2012).

266. Zhukovsky, M. A., Filograna, A., Luini, A., Corda, D. & Valente, C. Protein Amphipathic Helix Insertion: A Mechanism to Induce Membrane Fission. *Frontiers in Cell and Developmental Biology* **7**, 291 (2019).

267. Manna, P. T., Gadelha, C., Puttick, A. E. & Field, M. C. ENTH and ANTH domain proteins participate in AP2-independent clathrin-mediated endocytosis. *Journal of Cell Science* **128**, 2130–2142 (2015).

268. Pemberton, J. G. & Balla, T. Polyphosphoinositide-Binding Domains: Insights from Peripheral Membrane and Lipid-Transfer Proteins. *Advances in Experimental Medicine and Biology* **1111**, 77–137 (2019).

269. Kalthoff, C., Alves, J., Urbanke, C., Knorr, R. & Ungewickell, E. J. Unusual structural organization of the endocytic proteins AP180 and epsin 1. *Journal of Biological Chemistry* **277**, 8209–8216 (2002).

270. Zeno, W. F. *et al.* Synergy between intrinsically disordered domains and structured proteins amplifies membrane curvature sensing. *Nature Communications* **9**, 4152 (2018).

271. Snead, W. T. *et al.* BAR scaffolds drive membrane fission by crowding disordered domains. *Journal of Cell Biology* **218**, 664–682 (2019).

272. Chen, Z. & Schmid, S. L. Evolving models for assembling and shaping clathrin-coated pits. *Journal of Cell Biology* **219**, e202005126 (2020).

273. Snead, W. T. *et al.* Membrane fission by protein crowding. *Proceedings of the National Academy of Sciences of the United States of America* **114**, E3258–E3267 (2017).

274. Castner, D. G. & Ratner, B. D. Biomedical surface science: Foundations to frontiers. *Surface Science* **500**, 28–60 (2002).

275. Ratner, B. D., Weathersby, P. K., Hoffman, A. S., Kelly, M. A. & Scharpen, L. H. Radiation-grafted hydrogels for biomaterial applications as studied by the ESCA technique. *Journal of Applied Polymer Science* **22**, 643–664 (1978).

276. Hanson, S. R., Harker, L. A., Ratner, B. D. & Hoffman, A. S. In vivo evaluation of artificial surfaces with a nonhuman primate model of arterial thrombosis. *The Journal of Laboratory and Clinical Medicine* **95**, 289–304 (1980).

277. Tidwell, C. D. *et al.* Endothelial cell growth and protein adsorption on terminally functionalized, self-assembled monolayers of alkanethiolates on gold. *Langmuir* **13**, 3404–3413 (1997).

278. McArthur, S. L. Applications of XPS in bioengineering. *Surface and Interface Analysis* **38**, 1380–1385 (2006).

279. Lee, C. Y., Harbers, G. M., Grainger, D. W., Gamble, L. J. & Castner, D. G. Fluorescence, XPS, and TOF-SIMS surface chemical state image analysis of DNA microarrays. *Journal of the American Chemical Society* **129**, 9429–9438 (2007).

280. Tyler, B. J., Castner, D. G. & Ratner, B. D. Regularization: A stable and accurate method for generating depth profiles from angle-dependent XPS data. *Surface and Interface Analysis* **14**, 443–450 (1989).

281. Ratner, B. D., Horbett, T. A., Shuttleworth, D. & Thomas, H. R. Analysis of the organization of protein films on solid surfaces by ESCA. *Journal of Colloid And Interface Science* **83**, 630–642 (1981).

282. Paynter, R. W., Ratner, B. D., Horbett, T. A. & Thomas, H. R. XPS studies on the organization of adsorbed protein films on fluoropolymers. *Journal of Colloid And Interface Science* **101**, 233–245 (1984).

283. Gong, P., Lee, C. Y., Gamble, L. J., Castner, D. G. & Grainger, D. W. Hybridization behavior of mixed DNA/alkylthiol monolayers on gold: Characterization by surface plasmon resonance and32P radiometric assay. *Analytical Chemistry* **78**, 3326–3334 (2006).

284. Leone, L., Loring, J., Sjöberg, S., Persson, P. & Shchukarev, A. Surface characterization of the Gram-positive bacteria Bacillus subtilis-an XPS study. *Surface and Interface Analysis* **38**, 202–205 (2006).

285. Rouxhet, P. G. & Genet, M. J. XPS analysis of bio-organic systems. *Surface and Interface Analysis* **43**, 1453–1470 (2011).

286. Kjærvik, M., Schwibbert, K., Dietrich, P., Thissen, A. & Unger, W. E. Surface characterisation of Escherichia coli under various conditions by near-ambient pressure XPS. *Surface and Interface Analysis* **50**, 996–1000 (2018).

287. Lewis, K. B. & Ratner, B. D. Observation of surface rearrangement of polymers using ESCA. *Journal of Colloid And Interface Science* **159**, 77–85 (1993).

288. Shchukarev, A. & Ramstedt, M. Cryo-XPS: probing intact interfaces in nature and life. *Surface and Interface Analysis* **49**, 349–356 (2017).

289. Henderson, M. A. The interaction of water with solid surfaces: Fundamental aspects revisited. *Surface Science Reports* **46**, 1–308 (2002).

290. Shchukarev, A. XPS at solid-aqueous solution interface. *Advances in Colloid and Interface Science* **122**, 149–157 (2006).

291. Faubel, M., Steiner, B. & Toennies, J. P. Photoelectron spectroscopy of liquid water, some alcohols, and pure nonane in free micro jets. *Journal of Chemical Physics* **106**, 9013–9031 (1997).

292. Castner, D. G. Biomedical surface analysis: Evolution and future directions (Review). *Biointerphases* **12**, 02C301 (2017).

293. Zhai, W. L., Li, D. W., Qu, L. L., Fossey, J. S. & Long, Y. T. Multiple depositions of Ag nanoparticles on chemically modified agarose films for surface-enhanced Raman spectroscopy. *Nanoscale* **4**, 137–142 (2012).

294. Sarkar, A. & Daniels-Race, T. Electrophoretic Deposition of Carbon Nanotubes on 3-Amino-Propyl-Triethoxysilane (APTES) Surface Functionalized Silicon Substrates. *Nanomaterials* **3**, 272–288 (2013).

295. Jin, R. Quantum sized, thiolate-protected gold nanoclusters. *Nanoscale* **2**, 343–362 (2010).

296. Jin, R., Zeng, C., Zhou, M. & Chen, Y. Atomically Precise Colloidal Metal Nanoclusters and Nanoparticles: Fundamentals and Opportunities. *Chemical Reviews* **116**, 10346–10413 (2016).

297. Chen, Y. *et al.* Shortwave Infrared in Vivo Imaging with Gold Nanoclusters. *Nano Letters* **17**, 6330–6334 (2017).

298. Tao, Y., Li, M., Ren, J. & Qu, X. Metal nanoclusters: Novel probes for diagnostic and therapeutic applications. *Chemical Society Reviews* **44**, 8636–8663 (2015).

299. Loynachan, C. N. *et al.* Renal clearable catalytic gold nanoclusters for in vivo disease monitoring. *Nature Nanotechnology* **14**, 883–890 (2019).

300. Berglund, G. I. *et al.* The catalytic pathway of horseradish peroxidase at high resolution. *Nature* **417**, 463–468 (2002).

301. Haruta, M. Size- and support-dependency in the catalysis of gold. *Catalysis Today* **36**, 153–166 (1997).

302. Kurashige, W., Niihori, Y., Sharma, S. & Negishi, Y. Recent progress in the functionalization methods of thiolate-protected gold clusters. *Journal of Physical Chemistry Letters* **5**, 4134–4142 (2014).

303. Mekaru, H., Yoshigoe, A., Nakamura, M., Doura, T. & Tamanoi, F. Biodegradability of Disulfide-Organosilica Nanoparticles Evaluated by Soft X-ray Photoelectron Spectroscopy: Cancer Therapy Implications. *ACS Applied Nano Materials* **2**, 479–488 (2019).

304. Yesylevskyy, S. & Khandelia, H. EnCurv: Simple Technique of Maintaining Global Membrane Curvature in Molecular Dynamics Simulations. *Journal of Chemical Theory and Computation* **17**, 1181–1193 (2021).

305. Van Meer, G., Voelker, D. R. & Feigenson, G. W. Membrane lipids: Where they are and how they behave. *Nature Reviews Molecular Cell Biology* **9**, 112–124 (2008).

306. Song, W., Yen, H. Y., Robinson, C. V. & Sansom, M. S. State-dependent Lipid Interactions with the A2a Receptor Revealed by MD Simulations Using In Vivo-Mimetic Membranes. *Structure* **27**, 392–403.e3 (2019).

307. Corey, R. A., Stansfeld, P. J. & Sansom, M. S. The energetics of protein-lipid interactions as viewed by molecular simulations. *Biochemical Society Transactions* **48**, 25–37 (2020).

308. Shaw, A. S. Lipid rafts: Now you see them, now you don't. *Nature Immunology* **7**, 1139–1142 (2006).

309. Sonnino, S. & Prinetti, A. Membrane Domains and the "Lipid Raft" Concept. *Current Medicinal Chemistry* **20**, 4–21 (2012).

310. Šarić, A. & Cacciuto, A. Fluid membranes can drive linear aggregation of adsorbed spherical nanoparticles. *Physical Review Letters* **108**, 118101 (2012).

311. Schmidt, T. H., Homsi, Y. & Lang, T. Oligomerization of the Tetraspanin CD81 via the Flexibility of Its δ-Loop. *Biophysical Journal* **110**, 2463–2474 (2016).

312. Guixà-González, R. *et al.* Membrane omega-3 fatty acids modulate the oligomerisation kinetics of adenosine A2A and dopamine D2 receptors. *Scientific Reports* **6**, 19839 (2016).

313. Patel, D. S., Qi, Y. & Im, W. Modeling and simulation of bacterial outer membranes and interactions with membrane proteins. *Current Opinion in Structural Biology* **43**, 131–140 (2017).

314. Pezeshkian, W. & Marrink, S. J. Simulating realistic membrane shapes. *Current Opinion in Cell Biology* **71**, 103–111 (2021).

315. Marrink, S. J. *et al.* Computational Modeling of Realistic Cell Membranes. *Chemical Reviews* **119**, 6184–6226 (2019).

316. Florentsen, C. D. *et al.* Annexin A4 trimers are recruited by high membrane curvatures in giant plasma membrane vesicles. *Soft Matter* **17**, 308–318 (2021).

317. Duncan, A. L., Corey, R. A. & Sansom, M. S. Defining how multiple lipid species interact with inward rectifier potassium (Kir2) channels. *Proceedings of the National*

Academy of Sciences of the United States of America **117**, 7803–7813 (2020).

318. Wang, Q. *et al.* Lipid Interactions of a Ciliary Membrane TRP Channel: Simulation and Structural Studies of Polycystin-2. *Structure* **28**, 169–184.e5 (2020).

319. Roel-Touris, J. & Bonvin, A. M. Coarse-grained (hybrid) integrative modeling of biomolecular interactions. *Computational and Structural Biotechnology Journal* **18**, 1182–1190 (2020).